

2D MATERIALS FOR GAS-SENSING APPLICATIONS

by

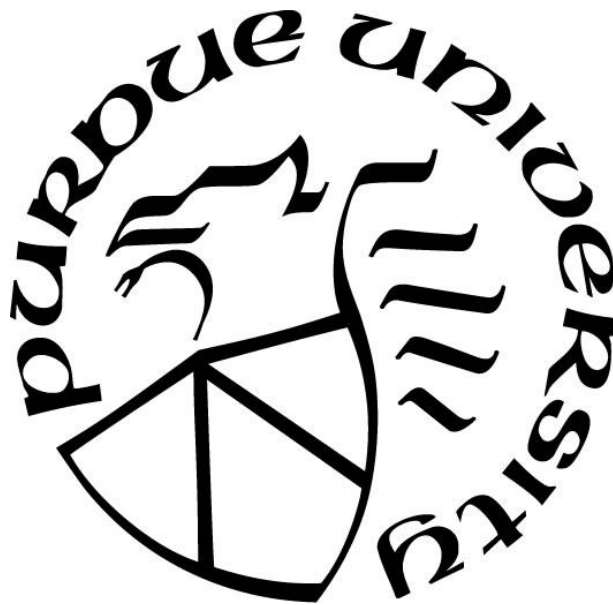
Winston Yenyu Chen

A Thesis

Submitted to the Faculty of Purdue University

In Partial Fulfillment of the Requirements for the degree of

Doctor of Philosophy



School of Materials Engineering

West Lafayette, Indiana

August 2021

THE PURDUE UNIVERSITY GRADUATE SCHOOL
STATEMENT OF COMMITTEE APPROVAL

Dr. Lia A. Stanciu, Chair

School of Materials Engineering

Dr. Alexander Wei

Department of Chemistry

Dr. Maria A. Okuniewski

School of Materials Engineering

Dr. Rahim Rahimi

School of Materials Engineering

Approved by:

Dr. David Bahr

Dedication

ACKNOWLEDGMENTS

Foremost, I would like to express my deepest gratitude to my advisor, Prof. Lia Stanciu, for their patience and encouraging manner in supervising me with immense knowledge during the last five years as a PhD student. Their guidance helped me all the time of my graduate research, including editing of my thesis, journal papers and grant support of funding and attending the 2019 MRS Fall Meeting.

I would also like to thank Profs. Alexander Wei, Maria Okuniewski, and Rahim Rahimi, who, as the members of my thesis committee, have given insightful comments and significant questions. I have learned much during the preliminary exam and data review.

I thank my fellow labmates in Purdue University: Sabrina Huang, Seon-Ah Jin, Susana Diaz, Ana Ulla, Shoumya Shuvo, Pengyu Xu, and Amit Barui, for stimulating discussions and assistance in experiments; I really enjoy the fun we have had in the last five years. I also want to thank my friends in Taiwan: Hang Lin, Chao-Chun Yen and Sz-Nian Lai.

Last but not the least, I would like to thank my parents, Giin-Shan Chen and Claire Lin, and my older brother Eric Chen for encouraging and inspiring my interests and supporting me spiritually and financially during the youth of my life.

TABLE OF CONTENTS

LIST OF TABLES	8
LIST OF FIGURES	9
ABSTRACT.....	15
1. INTRODUCTION TO 2D MATERIAL-BASED GAS SENSORS	17
1.1 Overview of 2D Materials	17
1.2 Motivation for 2D Material-Based Gas Sensors	18
1.3 Scope and Organization of the Dissertation	19
2. PROPERTIES AND APPLICATIONS OF 2D MATERIAL-BASED GAS SENSORS	21
2.1 Transition Metal Dichalcogenides (TMDCs).....	21
2.1.1 Structural Properties	21
2.1.2 Optical Properties	22
2.1.3 Electronic Properties	24
2.1.4 TMDC-Based Gas Sensors.....	25
2.2 Transition Metal Carbides/Nitrides (MXenes).....	30
2.2.1 Structural Properties	30
2.2.2 Optical Properties	32
2.2.3 Electronic Properties	32
2.2.4 MXene-Based Gas Sensors	33
2.3 Fundamental Challenges in 2D Gas-Sensing Devices	35
3. CHARACTERIZATION OF SOLUTION-PROCESSED 2D GAS-SENSING MATERIALS	39
3.1 Synthesis of 2D Materials	39
3.1 Solution Processing of Layered TMDCs and MXenes	40
3.1 Materials Characterization.....	42
3.2 Gas-Sensing Measurements.....	44
3.2.1 Equipment Setup	44
3.2.2 Wireless Sensing System.....	46
3.2.3 Gas-Sensing Parameters	47
4. FLEXIBLE AU-DECORATED MOS ₂ CONDUCTOMETRIC GAS SENSORS	49
4.1 Sensor Fabrication	49

4.1	Materials Characterization.....	49
4.2	The Performance of 2D MoS ₂ -based Sensor Towards VOCs.....	52
4.2.1	Au Nanoparticle Size and Distribution Effect.....	52
4.2.2	Relative Humidity Effect.....	53
4.2.3	Selectivity Performance	54
4.2.4	Sensing Mechanism of Au-Decorated MoS ₂	55
5.	SELECTIVE DETECTION OF ETHYLENE FOR CU(I)-PINCER COMPLEXES COATED MOS ₂ -SCNT	59
5.1	Sensor Fabrication	59
5.1	Materials Characterization.....	60
5.2	The Performance of Ethylene Sensors	63
5.2.1	Sensitivity and Selectivity Performance.....	63
5.2.2	Produce Testing.....	66
5.2.3	Mechanism for Selective Sensing of Ethylene.....	68
6.	FLEXIBLE Ti ₃ C ₂ T _x /WSe ₂ HYBRID CONDUCTOMETRIC GAS SENSORS.....	70
6.1	Sensor Fabrication	70
6.2	Materials Characterization.....	70
6.3	The Performance of 2D Ti ₃ C ₂ T _x -based Sensor Towards VOCs	73
6.3.1	Composition Ratio Effect.....	73
6.3.2	Film Thickness Effect	75
6.3.3	Environmental and Mechanical Stability	75
6.3.4	Sensitivity and Selectivity Performance.....	77
6.3.5	Sensing Mechanism.....	79
7.	FLEXIBLE SILANE-FUNCTIONALIZED Ti ₃ C ₂ T _x CONDUCTOMETRIC GAS SENSORS.....	81
7.1	Sensor Fabrication	81
7.2	Materials Characterization.....	81
7.3	The Performance of 2D Ti ₃ C ₂ T _x -based Sensor Towards VOCs	89
7.3.1	Film Thickness Effect	89
7.3.2	Signal-to-Noise Ratio	90
7.3.3	Sensitivity and Selectivity Performance.....	91
7.3.4	Response, Recovery and Durability of Sensors	93
7.3.5	Sensing Mechanism for Silane-functionalized MXene.....	95

8. CONCLUSIONS AND FUTURE DIRECTIONS	97
8.1 Conclusions	97
8.2 Future Perspectives.....	98
REFERENCES	100
PUBLICATIONS.....	109

LIST OF TABLES

Table 2.1 Electronic properties of TMDCs comprising different M and X atoms. ¹⁴	25
Table 2.2 Comparison of different types of gas-sensing devices. ⁴⁶	36
Table 2.3 Summaries of key parameters and performance indicators for recent studies of sensing volatile organic compounds using various 2D materials.	38
Table 3.1 Antoine coefficients of the various solvents used for vapor sensing experiments. ⁸⁴ ...	46
Table 4.1 Calculated adsorption energies (E_a) and heights (h) of an acetone molecule on MoS ₂ and MoS ₂ -Au nanoflakes either at horizontal or vertical orientation.	56
Table 5.1 Selected Raman and XPS signals from MoS ₂ -SCNT, coated with two different Cu(I)-pincer complexes. ⁹³	62
Table 7.1 Average baseline resistances of Ti ₃ C ₂ T _x , Ti ₃ C ₂ T _x -Cl, and Ti ₃ C ₂ T _x -F films measured in the gas sensing chamber at room temperature under air flow. ⁸¹	91

LIST OF FIGURES

Fig. 2.1 Section views of monolayered TMDCs from c-axis and [1120] directions with (a) trigonal prismatic and (b) octahedral coordinations, where purple and yellow atoms represent transition metal and chalcogen atoms, respectively. ¹⁴	21
Fig. 2.2 Schematics showing the three stacking forms of MoS ₂ : (a) 2H-hexagonal symmetry, (b) 3R-rhomohedral symmetry, and (c) 1T-tetragonal symmetry. ¹⁵	22
Fig. 2.3 Raman spectra of bulk and different layered MoS ₂ using 632.8 nm laser. ¹⁷	23
Fig. 2.4 Schematic of atomic displacements of Raman vibrational modes in MoS ₂ . ¹⁸	23
Fig. 2.5 UV-Vis spectra of MoS ₂ exfoliated with NMP, acetonitrile, hexane, and cyclohexane. ¹⁹	24
Fig. 2.6 Schematic illustration of the electronic band structure of D _{3h} and D _{3d} from TMDCs. ¹⁴	24
Fig. 2.12 Dynamic response curves of (a) single-layer and (b) double-layer MoS ₂ sensors for NO detection. ²⁷	26
Fig. 2.13 Dynamic response curves of MoS ₂ -based gas sensors upon exposure to (a) NO ₂ and (b) NH ₃ at different temperatures. ²⁸	27
Fig. 2.14 Schematics of charge-transfer mechanisms for MoS ₂ sensor in the presence of (a) NO ₂ and (b) NH ₃ gas molecules. ²⁸	27
Fig. 2.15 Comparison of monolayer MoS ₂ and carbon nanotube in response to triethylamine (TEA), tetrahydrofuran (THF), acetone, methanol, nitrotoluene (NT), 1,5-dichloropentane (DCP), and 1,4-dichlorobenzene (DCB). ²⁹	28
Fig. 2.16 Schematics showing the major adsorption sites of (a) MoS ₂ and (b) MUA-MoS ₂ in response to polar and nonpolar VOCs. ³⁰	28
Fig. 2.17 Responsivity of pristine MoS ₂ and MUA-functional MoS ₂ in response to nonpolar and polar VOCs. ³⁰	29
Fig. 2.18 Charge-density-difference images revealing the flow direction of charges and magnitude of charge transfer for the adsorption of (a) O ₂ , (b) H ₂ O, (c) NH ₃ , (d) NO, (e) NO ₂ , and (f) CO on 2D MoS ₂ . ³⁵	30
Fig. 2.7 The periodic table showing compositions of MXenes (top) and the schematics (bottom) showing the three typical structures of MXenes: M ₂ XT _x , M ₃ X ₂ T _x and M ₄ X ₃ T _x	31
Fig. 2.8 (a) Side and (b) top views of Ti ₃ C ₂ T _x MXene showing the hexagonal crystal structure with surface termination groups.....	31
Fig. 2.9 UV-vis-NIR transmittance spectra of Ti ₃ C ₂ T _x films with different thicknesses. ³⁸	32

Fig. 2.10 (a) Calculated band structure of Ti_3C_2 with different surface termination groups ($-OH$ and $-F$). ⁴² Calculated total density of states (DOS) of (b) $Ti_3C_2(OH)_2$ and (c) $Mo_2TiC_2(OH)_2$ showing a transition from metal to semiconductor by replacing outer Ti layers with Mo. ⁴³	33
Fig. 2.19 (a) Schematic illustration of $Ti_3C_2T_x$ sensor and structure. (b) Maximal resistance changes upon exposure to various gases at room temperature (25 °C). (c) Minimum binding energies of acetone and ammonia adsorbed on $Ti_3C_2(OH)_2$, $Ti_3C_2O_2$, $Ti_3C_2F_2$, graphene, MoS_2 , and BP. ⁷	34
Fig. 2.20 Real-time response of V_2CT_x sensors towards various gases. (a) Schematic illustration of V_2CT_x sensor for the detection of nonpolar (methane) and polar (acetone) gas molecules. ⁴⁴ .	35
Fig. 2.11 Schematics showing the layout of interdigitated electrodes and sensing layer for conductometric sensor. ⁴⁷	36
Fig. 3.1 Schematic diagrams summarizing the process flows of CVD-grown MoS_2 using various precursors: (a) ammonium thiomolybdate $[(NH_4)_2MoS_4]$, (b) molybdenum film, and (c) molybdenum trioxide film. ⁶⁹	39
Fig. 3.2 Schematic diagram of liquid phase exfoliation (top) and Li-ion intercalation (bottom) for low-dimensional TMDC fabrication. ⁷³	40
Fig. 3.3 Schematic illustrating the synthesis of MXenes from MAX phases by a selective etching process. ⁷⁷	41
Fig. 3.4 General map for the synthesis of $Ti_3C_2T_x$ MXenes from Ti_3AlC_2 MAX phase. ⁷⁶	42
Fig. 3.5 X-ray diffraction by planes of atom. ⁷⁸	43
Fig. 3.6 XRD patterns of the Ti_3AlC_2 and $Ti_3C_2T_x$ powders. ⁸⁰	43
Fig. 3.7 SEM images of (a) Ti_3AlC_2 and (b) $Ti_3C_2T_x$. ⁸⁰ (c) TEM micrograph of a single MXene nanosheet. ⁸¹	44
Fig. 3.8 Schematic diagram showing the setup of a homemade gas sensing system used for sensor testing. ⁸⁰	45
Fig. 3.9 Wireless sensor system. (a) Functional block diagram. (b) Image of a wireless-reading flexible sensor system. ⁸⁰	47
Fig. 4.1 Schematic of the process flows for the fabrication of conductometric VOC sensors on flexible substrates. (a) Liquid-phase exfoliation of bulk MoS_2 . (b) Functionalization of 2D MoS_2 nanoflakes with Au NPs. (c) Fabrication of Au-decorated MoS_2 sensors for VOC detection. ⁶³ .	49
Fig. 4.2 Top-view SEM images of (a) pristine MoS_2 , (b) $MoS_2-Au(0.5)$, and (c) $MoS_2-Au(2)$ nanoflakes, showing increase of size and coverage of Au NPs with increasing of $HAuCl_4$ molar concentration. (d) Energy diagram showing the relation between Fermi energy of MoS_2 and the reduction potential energy of Au^{3+} (+1.002 eV versus SHE), resulting in a spontaneous redox reaction between MoS_2 and $AuCl_4^-$. (e) HRTEM image and (f) high-angle annual dark-field STEM image and corresponding elemental mapping of Mo, S, and Au elements for $MoS_2-Au(0.5)$ showing a uniform distribution of Au NPs on MoS_2 . (g) Enlarged HRTEM image of Au NPs on MoS_2 , and corresponding (h) lattice fringes of MoS_2 (top) and Au (bottom). ⁶³	50

Fig. 4.3 XPS spectra of (a) Mo 3d, (b) S 2p, and (c) Au 4f for MoS₂ and MoS₂-Au(0.5). (d) Raman spectra of pristine MoS₂, MoS₂-Au(0.5), and MoS₂-Au(2) nanoflakes acquired at room temperature (λ_{ex} of 532 nm): the blue shifts in E¹_{2g} (in plane vibration) and A_{1g} (out-of-plane vibration) are attributed to an electron-donating effect of Au nanoparticles. (e) The energy band diagram for MoS₂ and Au, indicating electron transfer from Au nanoparticles to MoS₂.⁶³ 51

Fig. 4.4 (a) Real-time response to 120-ppm acetone by MoS₂, MoS₂-Au(0.25), MoS₂-Au(0.5), and MoS₂-Au(1). (b) Response plots of MoS₂-Au(0.5) to acetone (top) and hexane (bottom) ranging from 10 to 120 ppm. (c) Responses as a function of concentrations of acetone and hexane for MoS₂-Au(0.5). (d) Response and recovery times versus concentration curves of acetone for the MoS₂-Au(0.5) sensor derived from (b).⁶³ 53

Fig. 4.5 (a) Real-time response curves of the MoS₂-Au(0.5) sensor to 10 ppm of acetone under various RH levels (10–80%) and (b) the sensing response as a function of RH levels.⁶³ 53

Fig. 4.6 Real-time response curves of (a) pristine MoS₂ and (b) MoS₂-Au(0.5) sensors towards 40 ppm of acetone, ethanol, 2-propanol, hexane, toluene, and benzene at room temperature. (c) Corresponding maximal response changes towards various VOCs. (d) Consecutive sensing cycles (top) and long-term stability (bottom) of MoS₂-Au(0.5) sensors toward 40 ppm of acetone.⁶³ ... 55

Fig. 4.7 (a) Side and (b) top views of minimum energy configurations for an acetone molecule adsorbed on MoS₂-Au surface based on DFT simulations.⁶³ 56

Fig. 4.8 Enhanced sensing mechanism of Au-MoS₂ hybrid materials. (a) Hydrocarbon-based VOC molecules adsorbed onto MoS₂ creating only dipole scattering through electron clouds of their methyl groups and thus contributing a small change in electrical conductance. (b) Oxygen-based VOCs adsorbed onto MoS₂ creating the injection of electrons by the electron-donating properties of ethanol (right), and the interaction between oxygen species (O₂⁻ and O⁻) adsorbed on MoS₂ creating volatile species (CO₂ and H₂O), subsequently releasing electrons back to MoS₂; both mechanisms contributing to an increase in gas response. (c) Decoration of Au NPs resulting in an increasing of electron concentration on MoS₂, leading to an increase of adsorbed oxygen species and thus (d) for the Au-decorated MoS₂ to have higher responsivity and selectivity to oxygen-based VOCs owing to the returning of more electrons species to MoS₂ channel.⁶³ 58

Fig. 5.1 Schematic illustration of fabrication of MoS₂-SCNT based conductometric sensors on flexible substrates. (a) MoS₂-SCNT mixture cast onto Ag IDEs screen-printed on PET substrate; (b) MoS₂-SCNT film functionalized with Cu(I)-pincer complexes (Cu-Tp **1** and Cu-Tm **2**); (c) thin-film sensors in the detection of ethylene using a wireless monitoring system.⁹³ 59

Fig. 5.2 (a) SEM image of MoS₂-SCNT nanocomposite with network-like architecture; dotted circles show individual MoS₂ nanoflakes. (b) Conventional TEM image and (c) associated high-resolution TEM images of MoS₂ (top) and SCNT (bottom), showing a lattice spacing of 2.7 Å for MoS₂ (100) plane and a diameter of 1.5 nm for SCNT. (d) HAADF-STEM image and (e) corresponding elemental mapping of the MoS₂-SCNT nanocomposite.⁹³ 60

Fig. 5.3 Raman spectra, measured at room temperature (λ_{ex} 532 nm), showing (a) E¹_{2g} and A_{1g} vibrational modes of MoS₂ and (b) D and G bands of SCNTs for MoS₂-SCNT, **1**-MoS₂-SCNT, and **2**-MoS₂-SCNT. (c) Electrostatic potential maps of Cu-Tp **1** and Cu-Tm **2** indicates electron-rich (in red) and electron-deficient (in blue) surface regions, respectively. (d–f) XPS surface

analysis of MoS₂-SCNT and 2-MoS₂-SCNT: (d) Mo 3d region; (e) S 2p region; (f) Cu 2p region. Dashed lines indicate binding energies of the peaks before deposition of 2.⁹³..... 62

Fig. 5.4 (a) Real-time response to 10 ppm of C2 by MoS₂-SCNT, 1-MoS₂-SCNT, and 2-MoS₂-SCNT; (b) response of 2-MoS₂-SCNT to C2 concentrations ranging from 1.0 to 0.1 ppm; (c) steady-state response of 2-MoS₂-SCNT as a function of C2 concentration ($\pm 1\sigma$; $N = 3$); (d) sensitivity of 2-MoS₂-SCNT to C2 (steady-state response at 10 ppm; \pm noise) versus other volatile species (20–50 ppm). Responses of 1-MoS₂-SCNT, 2-MoS₂, and 2-SCNT to C2 (10 ppm) provided for reference.⁹³..... 64

Fig. 5.5 (a) Real-time response curves of 2-MoS₂ to 10 ppm of ethylene (b) Electrical noise measurements of 2-MoS₂, MoS₂-SCNT, 1-MoS₂-SCNT, 2-MoS₂-SCNT during nitrogen exposure.⁹³..... 65

Fig. 5.6 Real-time response to ethylene (C2; 10 ppm) by 2-MoS₂-SCNT using different carrier gases (N₂ and air).⁹³..... 66

Fig. 5.7 Long-term stability of the 2-MoS₂-SCNT sensor under exposure to 1 ppm of ethylene for 5 min every two days over one month. Data points represented steady-state $-\Delta G/G_0$ values.⁹³.. 66

Fig. 5.8 (a) Experimental setup for monitoring ethylene released by various fruit samples at room temperature, monitored by a wireless 2-MoS₂-SCNT sensor. (b) Conductometric response of the 2-MoS₂-SCNT sensor to various fruit samples incubated for 8 h.⁹³..... 67

Fig. 5.9 Experimental setup for gas-sensing measurements using a wireless MoS₂-SCNT-based sensor. The masses of each fruit tested were as follows: bananas (1.09 kg), apples (1.2 kg), tomatoes (1.08 kg), oranges (1.19 kg), and strawberries (1.08 kg).⁹³..... 68

Fig. 5.10 Illustration of ethylene sensing mechanism by 2-MoS₂-SCNT: (a) semiconducting MoS₂-SCNT nanocomposite; (b) increased electron mobility due to charge-transfer interactions between Cu-Tm 2 and MoS₂-SCNT; (c) partial disruption of doping effect upon exposure to ethylene.⁹³..... 69

Fig. 6.1 (a) Schematic illustration of preparation processes for Ti₃C₂T_x/WSe₂ nanohybrids. (b) Schematic illustration of inkjet-printed sensors for wireless VOC detections.⁸⁰..... 70

Fig. 6.2 (a) SEM image of Ti₃C₂T_x/WSe₂ nanohybrid film (scale bar, 2 μ m). (b) Low magnification TEM image (scale bar, 200 nm), with (c) showing image of a single Ti₃C₂T_x/WSe₂ nanohybrid (scale bar, 100 nm). (d) High-resolution TEM image of Ti₃C₂T_x/WSe₂ nanohybrid (scale bar, 100 nm). (e) Selected area electron diffraction pattern of Ti₃C₂T_x/WSe₂ nanohybrids (scale bar, 2 nm⁻¹). (f) HAADF-STEM image and corresponding elemental mapping of Ti, W, and Se for the Ti₃C₂T_x/WSe₂ nanohybrid showing a uniform decoration of WSe₂ nanoflakes on Ti₃C₂T_x matrix.⁸⁰..... 71

Fig. 6.3 The size distribution of Ti₃C₂T_x/ WSe₂ nanohybrids measured by dynamic light scattering.⁸⁰..... 72

Fig. 6.4 XPS spectra of (a) Ti 2p, (b) O 1s, (c) C 1s, and (d) W 4f from Ti₃C₂T_x/WSe₂ nanohybrids, showing chemical compositions and bonding configurations of Ti₃C₂T_x/WSe₂ nanohybrids.⁸⁰.. 73

Fig. 6.5 Comparison of room-temperature sensing responses of (a) pristine Ti₃C₂T_x, (b) WSe₂, (c) Ti₃C₂T_x/WSe₂ (2 wt%), and (d) Ti₃C₂T_x/WSe₂ (4 wt% WSe₂) upon exposure to 40-ppm ethanol.

(e) Electrical noise measurements. HAADF-STEM images of (f) $\text{Ti}_3\text{C}_2\text{T}_x/\text{WSe}_2$ (2 wt% WSe_2) and (g) $\text{Ti}_3\text{C}_2\text{T}_x$ (4% WSe_2). Scale bars: 100 nm. ⁸⁰	74
Fig. 6.6 Thickness-dependent responses of 60, 120, and 180-nm-thick $\text{Ti}_3\text{C}_2\text{T}_x/\text{WSe}_2$ films toward 40 ppm of ethanol and acetone. ⁸⁰	75
Fig. 6.7 Changes in electrical conductance of pristine $\text{Ti}_3\text{C}_2\text{T}_x$ and hybrid $\text{Ti}_3\text{C}_2\text{T}_x/\text{WSe}_2$ sensors under (a) 5% RH and (b) alternative RHs of 5 and 80% over 10 days. (c) Real-time responses of $\text{Ti}_3\text{C}_2\text{T}_x/\text{WSe}_2$ sensors toward 40 ppm ethanol under various RHs and (d) the sensing responses versus various RHs from 5 to 80%. ⁸⁰	76
Fig. 6.8 (a) Photograph of a flexible $\text{Ti}_3\text{C}_2\text{T}_x/\text{WSe}_2$ nanohybrid sensor. (b) Bending test over 1000 cycles revealing stable electrical conductance and slightly increases in ethanol sensing response. ⁸⁰	77
Fig. 6.9 (a) Real-time sensing response of $\text{Ti}_3\text{C}_2\text{T}_x$ and $\text{Ti}_3\text{C}_2\text{T}_x/\text{WSe}_2$ gas sensors upon exposure to ethanol from 1 to 40 ppm. (b) Gas response versus ethanol concentrations for $\text{Ti}_3\text{C}_2\text{T}_x$ and $\text{Ti}_3\text{C}_2\text{T}_x/\text{WSe}_2$ sensors. (c) Cycling responses and (d) long-term (one-month) stability of response of $\text{Ti}_3\text{C}_2\text{T}_x/\text{WSe}_2$ sensors toward 40 ppm of ethanol. (e) Response and recovery times of $\text{Ti}_3\text{C}_2\text{T}_x/\text{WSe}_2$ gas sensors. (f) Selectivity test of the $\text{Ti}_3\text{C}_2\text{T}_x$ and $\text{Ti}_3\text{C}_2\text{T}_x/\text{WSe}_2$ sensors toward various VOCs at 40 ppm. ⁸⁰ All the experiments were performed at room temperature.	78
Fig. 6.10 Enhanced sensing mechanism of $\text{Ti}_3\text{C}_2\text{T}_x/\text{WSe}_2$ heterostructure. Energy-band diagram of the $\text{Ti}_3\text{C}_2\text{T}_x/\text{WSe}_2$ in (a) air and (b) ethanol, showing the variation of the depletion layer with an interaction between adsorbed oxygen species and ethanol molecules. ⁸⁰	80
Fig. 7.1 Schematic process flows for the preparation of silane-modified $\text{Ti}_3\text{C}_2\text{T}_x$. ⁸¹	81
Fig. 7.2 (a) XRD patterns of Ti_3AlC_2 , $\text{Ti}_3\text{C}_2\text{T}_x$, $\text{Ti}_3\text{C}_2\text{T}_x\text{-Cl}$, and $\text{Ti}_3\text{C}_2\text{T}_x\text{-F}$ samples. SEM images of (b) Ti_3AlC_2 , (c) as-etched $\text{Ti}_3\text{C}_2\text{T}_x$, and (d) spray-coated $\text{Ti}_3\text{C}_2\text{T}_x\text{-F}$ film. (e) HAADF-STEM image and corresponding element mappings of $\text{Ti}_3\text{C}_2\text{T}_x\text{-F}$ nanosheets showing a uniform distribution of Ti, C, and F. ⁸¹	82
Fig. 7.3 EDS spectrum of FOTS-functionalized $\text{Ti}_3\text{C}_2\text{T}_x$ with a silicon characteristic peak of FOTS at 1.73 keV.	82
Fig. 7.4 Nitrogen adsorption/desorption isotherms for Ti_3AlC_2 , $\text{Ti}_3\text{C}_2\text{T}_x$, $\text{Ti}_3\text{C}_2\text{T}_x\text{-Cl}$ and $\text{Ti}_3\text{C}_2\text{T}_x\text{-F}$ samples. ⁸¹	83
Fig. 7.5 (a) Water contact angle images of $\text{Ti}_3\text{C}_2\text{T}_x$, $\text{Ti}_3\text{C}_2\text{T}_x\text{-Cl}$, and $\text{Ti}_3\text{C}_2\text{T}_x\text{-F}$ films. (b) Evolution of contact angles of $\text{Ti}_3\text{C}_2\text{T}_x\text{-F}$ versus reaction times. (c) Zeta potential plots of $\text{Ti}_3\text{C}_2\text{T}_x$, $\text{Ti}_3\text{C}_2\text{T}_x\text{-Cl}$, and $\text{Ti}_3\text{C}_2\text{T}_x\text{-F}$ samples. ⁸¹	84
Fig. 7.6 Schematic illustration of surface functionalization of $\text{Ti}_3\text{C}_2\text{T}_x$ MXene with FOTS. ⁸¹ ...	85
Fig. 7.7 XPS survey spectra of pristine $\text{Ti}_3\text{C}_2\text{T}_x$ (bottom) and FOTS-functionalized $\text{Ti}_3\text{C}_2\text{T}_x$ (top). ⁸¹	85
Fig. 7.8 XPS spectra of (a) Ti 2p, (b) C 1s, (c) O 1s, and (d) F 1s revealing chemical compositions and bonding characteristics of the FOTS-functionalized $\text{Ti}_3\text{C}_2\text{T}_x$ nanosheets. ⁸¹	86

Fig. 7.9 (a) Water contact angle for $Ti_3C_2T_x$ -F films after exposure to NH_4OH (pH 11.3), DI water (pH 6.8), and HCl (pH 1.1) for 2, 5, 10, and 20 s, respectively. (b) Water contact angle variations of $Ti_3C_2T_x$ -F films for 2-month storage in air. Changes in electrical conductance of $Ti_3C_2T_x$ and $Ti_3C_2T_x$ -F under (c) 5% RH and (d) alternative RHs of 5 and 100% over a period two weeks.⁸¹ 88

Fig. 7.10 Ti 2p XPS spectra showing the alternation of Ti chemical species contained in pristine (a) and (b) humidity treated $Ti_3C_2T_x$ films, along with the (c) plots showing proportion changes of the various Ti species derived from integrated peak areas; (d)-(f) revealing the corresponding results of $Ti_3C_2T_x$ -F.⁸¹ 89

Fig. 7.11 Thickness-dependent responses of 50, 100, and 200-nm-thick $Ti_3C_2T_x$ -F films toward 30 ppm of acetone and ethanol.⁸¹ 90

Fig. 7.12 Electrical noise levels of $Ti_3C_2T_x$, $Ti_3C_2T_x$ -Cl, and $Ti_3C_2T_x$ -F sensors during air exposure.⁸¹ 90

Fig. 7.13 (a) Real-time response curves of $Ti_3C_2T_x$, $Ti_3C_2T_x$ -Cl, and $Ti_3C_2T_x$ -F sensors toward ethanol from 5 to 120 ppm and (b) the response as a function of ethanol. (c) Gas response of $Ti_3C_2T_x$ -F sensors upon exposure to 30 ppm of acetone, ethanol, 2-propanol, toluene, benzene, hexane, ethylene, carbon dioxide, and nitrogen dioxide. (d) Maximal response variations toward various gases at room temperature. (e) Schematics of $Ti_3C_2T_x$ and $Ti_3C_2T_x$ -F films upon exposure to VOCs.⁸¹ 92

Fig. 7.14 (a) Response and recovery plot of $Ti_3C_2T_x$ -F toward 5 ppm of ethanol. (b) Response and (c) recovery times under different ethanol concentrations for the $Ti_3C_2T_x$, $Ti_3C_2T_x$ -Cl, $Ti_3C_2T_x$ -F sensors. (d) Real-time response curves of the $Ti_3C_2T_x$ -F sensor toward 30 ppm of ethanol under different RH levels from 5 to 80%. (e) Sensing response of the $Ti_3C_2T_x$ -F sensor to 30 ppm of ethanol versus bending cycles. (f) Long-term stability over a month (bottom) and consecutive sensing cycles (top) of the $Ti_3C_2T_x$ -F sensor toward 30 ppm of ethanol.⁸¹ 94

Fig. 7.15 (a) Side and top views of minimum energy configurations for an ethanol molecule (C_2H_5OH) adsorbed on $Ti_3C_2T_x$ -F surface based on DFT simulations. (b) Calculated minimum adsorption energies of toluene and ethanol on $Ti_3C_2T_x$ and $Ti_3C_2T_x$ -F *versus* corresponding sensing responses.⁸¹ 96

Fig. 8.1 The pie chart showing the potential applications of MXene materials for energy conversion/storage, catalysis, electromagnetic interference shielding, and biomedical sensors. . 99

ABSTRACT

Two-dimensional (2D) transition-metal dichalcogenides (TMDCs) and transition metal carbides/nitrides (MXenes), have been recently receiving attention for gas sensing applications due to their high specific area and rich surface functionalities. Using pristine 2D materials for gas-sensing applications, however, presents some drawbacks, including high operation temperatures, low gas response, and poor selectivity, limiting their applications in this area. Moreover, one of the long-standing challenges of MXenes is their poor stability against hydration and oxidation in a humid environment, which negatively influences their long-term storage and applications. Many studies have reported that the sensitivity and selectivity of 2D materials can be improved by surface functionalization and hybridization with other materials.

In this work, the properties of these two materials classes (TMDCs and MXenes) have been investigated and the results viewed through the lens of their implantation into chemoresistive gas sensors. In one of the lines of research, 2D MoS₂ nanoflakes were functionalized with Au nanoparticles through a facile solution mixing method. Au-decorated MoS₂ was used as a material platform for an electrochemical sensor to detect various volatile organic compounds (VOCs) at room temperature. After Au functionalization, the enhancement of gas-sensing performance in terms of response and selectivity, especially in detecting oxygen-based VOCs (acetone, ethanol, and 2-propanol), was observed. The response of the gas sensor to acetone improved by 131% (changing from 13.7% for pristine MoS₂ to 31.6% for MoS₂- Au(0.5)) owing to Au doping. Sensing tests under various relative humidity values (10–80%), repeated bending cycles, or after long-term storage, indicated the sound robustness and flexibility of the sensor. Density functional theory (DFT) simulations showed that the adsorption energy of acetone on Au-MoS₂ is significantly greater than that of on pristine MoS₂, contributing to an enhancement of VOC sensing. This work put forward an understanding of the dominant sensing mechanism for the highly sensitive and selective detection of oxygen-based VOCs with Au doped MoS₂ electrode materials.

Next, a nanocomposite film composed of exfoliated MoS₂, single-walled carbon nanotubes (SCNTs), and Cu(I)-tris(mercaptoimidazolyl)borate complexes (Cu-Tm) was the electrode material used for the design of a chemoresistive sensor for the real-time detection of ethylene (C₂H₄). The reported detection limit of this sensor was of 100 ppb. A co-percolation network of MoS₂ and SCNTs was deposited onto interdigitated Ag electrodes, printed on plastic substrates,

and then coated with Cu–Tm, with a final electrode conductance in the 0.5 mS range. The thin-film sensors were highly selective toward C₂H₄, and they responded weakly to other volatile organic compounds or water at similar partial pressures. A mechanism is proposed in which Cu–Tm acts as a chemically sensitive n-type dopant for MoS₂, based on spectroscopic characterization and DFT simulations. Cu–Tm-coated MoS₂/SCNT sensors were also connected to a battery-powered wireless transmitter and used to monitor C₂H₄ production from various fruit samples, validating their utility as practical, field-deployable sensors.

The hybridization of MXene and TMDC as gas-sensing materials were also proposed; Ti₃C₂T_x and WSe₂ are selected as model materials for hybridization. The Ti₃C₂T_x/WSe₂ hybrid sensor reveals high sensitivity, good selectivity, low noise level, ultrafast response/recovery times for the detection of various VOCs. Compared with pristine Ti₃C₂T_x sensor, the sensitivity of the hybrid sensor to ethanol was improved by over 12-fold. Furthermore, the hybridization process offers an effective strategy against MXene oxidation by restricting the interaction of water molecules from the edges of Ti₃C₂T_x. An enhancement mechanism for Ti₃C₂T_x/WSe₂ materials is proposed in which the numerous heterojunctions formed greatly improved the sensitivity and selectivity toward detection of oxygen-containing VOCs. The scientific findings of this work could guide future exploration of next-generation field-deployable sensors.

Lastly, we demonstrated a surface functionalization strategy for Ti₃C₂T_x with fluoroalkylsilane (FOTS) molecules, providing not only a superhydrophobic surface, mechanical/environmental stability but also enhanced sensing performance. Compared to pristine material, the FOTS-functionalized Ti₃C₂T_x shows the enhancement of gas-sensing performance in terms of sensitivity, repeatability, long-term stability, and selectivity and faster response/recovery toward oxygen-containing VOCs (ethanol, acetone). FOTS functionalization also offered protection of the sensor response to 30 ppm of ethanol over a 5 to 80% relative humidity range. DFT simulations suggested that the strong adsorption energy of ethanol on Ti₃C₂T_x-F and the local structure deformation induced by its adsorption contributed to the reported gas-sensing enhancement. This study offers a practical and facile solution for developing highly reliable MXene-based gas sensors with stable chemoresistive response in humid environment.

1. INTRODUCTION TO 2D MATERIAL-BASED GAS SENSORS

1.1 Overview of 2D Materials

The new research area of two-dimensional materials (2D) has received extensive attention since Geim's group used a mechanical exfoliation method to obtain single-layer graphene in 2004.¹ Graphene has unique mechanical, structural, optical and electrical properties. However, the lack of energy bandgap limits its applications in optoelectronic and sensing devices. Because of their unusual properties, other 2D materials, such as transition metal dichalcogenides (TMDCs), hexagonal boron nitride (h-BN), black phosphorous (BP), and transition metal nitrides/carbides (MXenes) soon afterward attracted much attention. MoS₂, WS₂, WSe₂, and MoSe₂, a family of TMDC semiconducting materials, have attracted great attention because they possess layer-dependent tunable bandgaps in the visible and near infrared range. Therefore, semiconducting TMDCs are promising functional materials for the design and fabrication of chemical sensors and biosensors, as well as for various optoelectronic device applications.²⁻⁴

Molybdenum disulfide (MoS₂) bulk crystal, a typical TMDC, has an indirect bandgap of 1.3 eV. Upon forming a 2D layer-like structure, MoS₂ becomes a direct bandgap material with an enlarged bandgap energy. For example, the MoS₂ monolayer has a direct bandgap of 1.9 eV.⁵ As is well-known, the performance of a gas-sensing device, such as responsivity, selectivity and stability, depends on specific surface area, conducting properties, and surface functionalization of the sensing material. MoS₂ nanoflakes have a high specific surface area, good electrical properties, and tunable direct bandgap, and thus are considered as an alternative to graphene for various optoelectronic and electronic applications, including room-temperature gas sensing. Ti MXenes (Ti₃C₂T_x), a new family of multifunctional 2D materials, have an excellent combination of physical and chemical properties, including metallic conductivity, hydrophilic nature, chemically active surfaces, and excellent mechanical properties.⁶ Recent studies have shown that gas sensors based on MXenes exhibit an excellent sensitivity and an extremely low detection limit compared to other 2D materials.⁷

1.2 Motivation for 2D Material-Based Gas Sensors

2D materials display excellent sensor-relevant properties, including adjustable and high specific surface area, rich surface functionalities, atomic-level thickness, and exceptional electronic properties, and are thus promising candidates for electrically-transduced chemical sensors.⁸ The high specific surface area of 2D materials provides a great number of active sites for the adsorption of gas molecules and contributes to an increase in sensitivity compared to bulk materials, even at extremely low concentration of a target analyte. At the same time, the available rich surface functionalities can be leveraged for a specific recognition of target analytes via surface functional groups, which has the potential of further improving a sensor's performance in terms of selectivity and sensitivity.

2D materials, such as TMDCs and MXenes, also exhibit exceptional physical properties, including strong mechanical strength and good optical transparency. The main limitations of 2D materials used for chemical gas sensing are: (i) their lack of environmental stability and selectivity; (ii) the fact that a mass-production method for commercial sensor manufacturing is yet to be available. Therefore, finding avenues towards improving these materials environmental stability and selectivity, with huge benefits to their sensing performance in practical settings, along with developing a reliable mass-production method, are topics worthy of investigation.

Solution processing is a facile, cost-effective method, amenable for the mass production of 2D materials, and thus deserves further study.⁹ MoS₂ nanoflakes fabricated by solution methods provide more active sites for functionalization than other methods, thus achieving a better recognition of specific analytes. However, it is not easy to fabricate high-performance, room-temperature gas sensors simply using pristine 2D MoS₂ because of its lack of sensing selectivity and sensitivity. To overcome this problem, strategies of surface modification of 2D MoS₂ need to be further investigated. Ti₃C₂T_x MXene have been explored as another promising candidate for gas-sensing application owing to their excellent combination of physical and chemical properties, including high electrical conductivity, abundant surface functional groups, and structural stability. MXenes, however, degrade rapidly over time in air or in the presence of water because they possess a hydrophilic character. Thus, how to overcome the oxidation tendency of MXenes for real-life sensing applications is another research area worth exploring.

1.3 Scope and Organization of the Dissertation

2D materials have attracted great attention for gas-sensing applications. Various approaches have been proposed to improve the sensitivity and selectivity of 2D materials to target analytes, including hybridization with metal oxides (e.g., SnO₂, ZnO, or WO₃), conducting polymers or carbon-based materials, surface functionalization with noble metallic nanoparticles (e.g., Ag, Au, Nb, Pt), and designing heterostructures.¹⁰⁻¹² However, the current VOC-sensing strategies present with some drawbacks, including high operation temperatures, low gas response, lack of selectivity, and complex fabrication. In this study, functionalization/hybridization strategies of 2D materials are studied for developing high performance gas-sensing devices. The strategies presented here can be an effective solution for not only improving materials' stability, but also enhancing sensor performance, shedding light on the development of next-generation field-deployable electrochemical sensing devices suitable for IoT applications.

This work investigates the effect of surface functionalization and/or hybridization of 2D materials on their gas sensing performance. The functionalization of MoS₂ with Au nanoparticles (NPs) provides a performance enhancement towards sensing of volatile organic compounds (VOCs). The dominant sensing mechanism of Au-decorated MoS₂ for enhancing the response and selectivity toward oxygen-containing VOCs is proposed. Moreover, a hybrid nanomaterial of MoS₂ and single-walled carbon nanotubes (SCNTs) coated with Cu(I)-pincer complex for the sensitive and selective detection of ethylene is also investigated. The effect of doping Cu(I)-pincer complexes on the MoS₂-SCNTs semiconducting networks is studied. Moreover, the effect of hybridizing MXene (Ti₃C₂T_x) with a different TMDC material, tungsten disulfide (WSe₂), on the oxidation stability of MXene and the gas-sensing performance is studied. The Ti₃C₂T_x/WSe₂ heterostructured material is proposed for highly sensitive and selective detection of oxygen-containing VOCs. The enhancement of VOC sensing is attribute to the formation of Ti₃C₂T_x/WSe₂ heterojunctions, which effectively accelerates the transport of electrons and creates additional active site for gas adsorption. Finally, a surface functionalization strategy for Ti₃C₂T_x with silane self-assembled monolayer (SAM) as a protection layer for VOC sensing is presented. The formation of superhydrophobic Ti₃C₂T_x by a fluoroalkylsilane (FOTS)-SAM coating offers an effective protection for Ti₃C₂T_x against oxidation, realizing a robust MXene hybrid material for practical gas-sensing applications.

The rest of this dissertation is organized as follows. Chapter 2 gives a comprehensive literature review of the physical properties of 2D TMDC and MXene, as well as their application in gas-sensing devices. Chapter 3 focuses on the solution processing and characterization techniques for 2D materials, and gas-sensing measurements. Chapters 4 to 7 provide detailed discussion on the 2D hybrid materials used for gas-sensing devices, sensors' performance data, and materials characterization results. Chapter 8 proposes future research topics, including fabrication of electronic nose devices for multiple VOC-sensing by roll-to-roll mass production, and fabrication of biomedical sensors with MXenes as electrode materials.

2. PROPERTIES AND APPLICATIONS OF 2D MATERIAL-BASED GAS SENSORS

2.1 Transition Metal Dichalcogenides (TMDCs)

2.1.1 Structural Properties

TMDCs are composed of a transition element and a chalcogen. Their general chemical formula is MX_2 , where M is a transition element such as Mo or W and X is chalcogen such as S or Se. Monolayered MoS_2 , one of the topic materials of this study, can be considered as a sandwich structure in the form of S-Mo-S, where the layers are vertically bonded together by van der Waals interactions and the elements within each layer are strongly and covalently bonded.¹³ Therefore, bulk MoS_2 can be cleaved into few-layer MoS_2 under the action of an external force, such as mechanical or liquid phase exfoliation. The valences of the metal (M) and chalcogen (X) atoms are +4 and -2, respectively. The lone-pair electrons of the chalcogen atoms terminate the surface of the layers, and the lack of dangling bonds on the top of the surface is similar to that of graphene, leading to a chemically stable surface on the basal planes of TMDCs.¹⁴ The coordination of metallic (Mo) and chalcogen (S) atoms is based on the thermodynamically preferred configuration, and can be either trigonal prismatic (D_{3h}) or octahedral (O_h or D_{3d}), as shown in **Fig. 2.1**(a) and (b), respectively.¹⁴

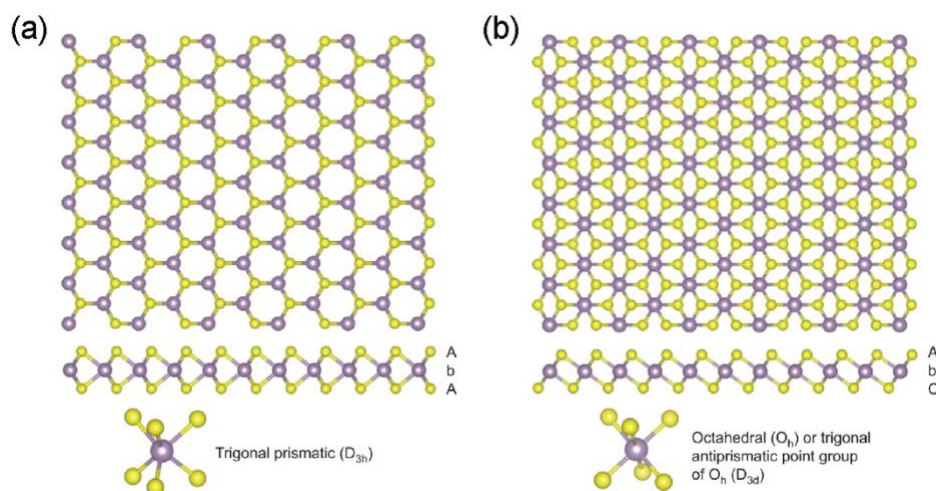


Fig. 2.1 Section views of monolayered TMDCs from c -axis and $[11\bar{2}0]$ directions with (a) trigonal prismatic and (b) octahedral coordinations, where purple and yellow atoms represent transition metal and chalcogen atoms, respectively.¹⁴

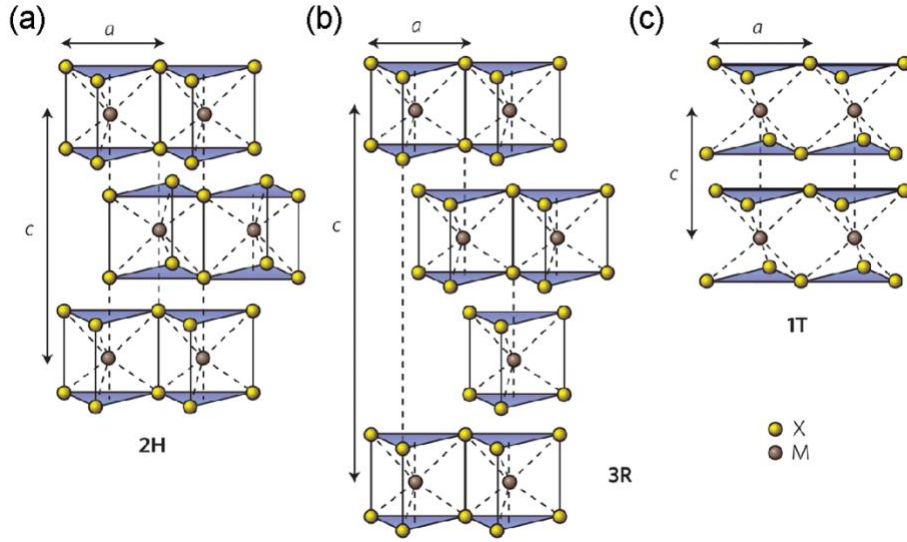


Fig. 2.2 Schematics showing the three stacking forms of MoS₂: (a) 2H-hexagonal symmetry, (b) 3R-rhombohedral symmetry, and (c) 1T-tetragonal symmetry.¹⁵

As shown in **Fig. 2.2**, there are three stacking forms for layered MoS₂, including 2H (hexagon with 2 layers per repeated unit), 3R (rhombohedron with 3 layers per repeated unit), and 1T (tetragon with 1 layer per repeated unit).¹⁵ The commonly observed stacking forms of MoS₂ are 2H and 3R, both of which have a trigonal prismatic arrangement of atoms.¹⁶ 2D-MoS₂ has a more versatile stacking structure than graphene because a MoS₂ monolayer contains three layers of atoms (S-Mo-S).

2.1.2 Optical Properties

Layered MoS₂ has a tunable bandgap ranging from 1.3 to 1.9 eV, which is determined by the number of layers. Raman spectroscopy, which measures a signal resulting from inelastic collisions between incident photons and lattice vibrations of materials, is a powerful and commonly used method to characterize the bonding structures of 2D materials. As shown in **Fig. 2.3**, the Raman spectra of single- and multi-layered MoS₂ contain three characteristic peaks: 2LA(M), A_{1g}, and E_{2g}¹. The peak of 2LA(M) is located at around 460 cm⁻¹ and is due to the longitudinal acoustic phonons at M point.¹⁷ The peak of the out-of-plane A_{1g} mode (approximately 404 cm⁻¹) results from the vibrations of solely S atoms in opposite directions. The peak of the in-plane E_{2g}¹ mode

(near 380 cm^{-1}) is caused by the opposite vibrations of two Mo atoms relative to S atom. As shown in **Fig. 2.4**, the other two modes, E_{1g} and E_{2g}^2 , could not be detected due to the selection rule.¹⁸

The vibrational modes of A_{1g} and E_{2g}^1 are closely related to the layer number of MoS₂. The strengthening of in-plane bonding and weakening between layers with decreasing sample thickness (i.e., layer number) result in blue shifts of the in-plane E_{2g}^1 peak and red shifts of the out-of-plane A_{1g} peak. Therefore, Raman spectroscopy is a facile technique for a reliable determination of the layer number of 2D MoS₂ according to the location of its characteristic peaks.

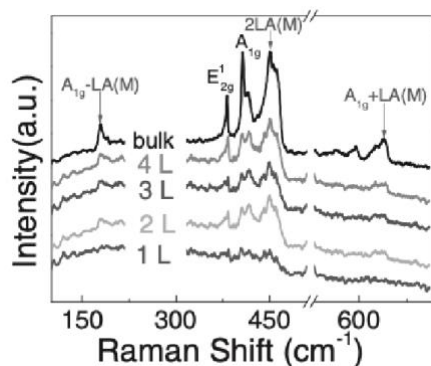


Fig. 2.3 Raman spectra of bulk and different layered MoS₂ using 632.8 nm laser.¹⁷

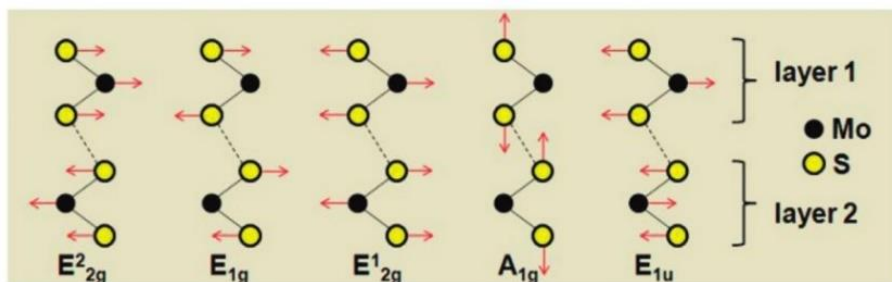


Fig. 2.4 Schematic of atomic displacements of Raman vibrational modes in MoS₂.¹⁸

UV-vis absorption spectroscopy is a common method for the analysis of the dependence of exfoliation levels and concentrations of 2D MoS₂ on solvent types used during exfoliation processing. **Fig. 2.5** reveals that the MoS₂ exfoliated by N-Methyl-2-pyrrolidone (NMP) solvent is lack of UV-Vis peaks, owing to a low concentration of 2D MoS₂ fabricated in the solvent.

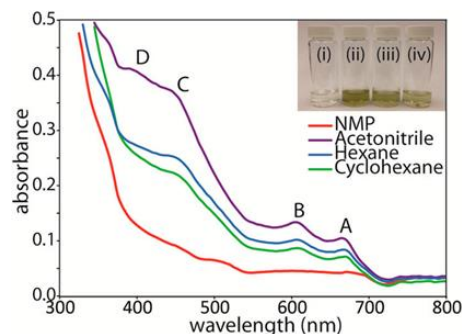


Fig. 2.5 UV-Vis spectra of MoS₂ exfoliated with NMP, acetonitrile, hexane, and cyclohexane.¹⁹

Additionally, **Fig. 2.5** reveals that absorption peaks from high concentrations of 2D MoS₂ fabricated by high levels of exfoliation using acetonitrile solvent are clearly located approximately at 660, 610, 450, and 395 nm, and referred to as A, B, C, and D, respectively. The A and B peaks result from direct excitonic transitions at the K point of the Brillouin zone. The C and D peaks arise from direct excitonic transition of the M point.^{19,20}

2.1.3 Electronic Properties

The electronic structure of TMDCs depends on the coordination of metal atoms and its *d* electron count. In both D_{3h} and D_{3d} structures, the non-bonding *d* bands of the TMDCs are located between the bonding (σ) and antibonding (σ^*) bands of M–X bonds, as presented in **Fig. 2.6**.¹⁴

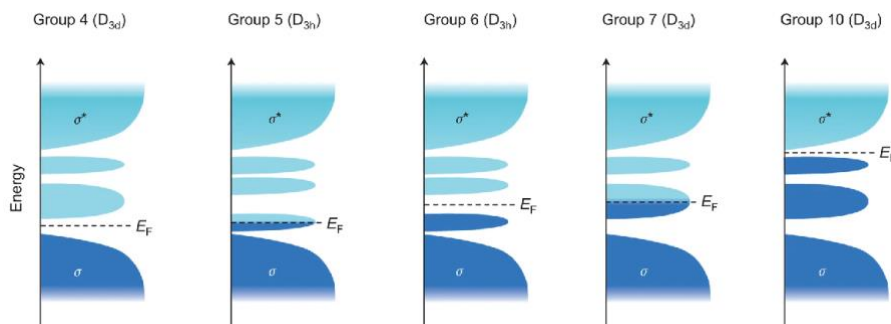


Fig. 2.6 Schematic illustration of the electronic band structure of D_{3h} and D_{3d} from TMDCs.¹⁴

The difference in band structures leads to diverse electronic properties of TMDCs as shown in **Table 2.1**. When an orbital is partially filled (Fermi level is within the band) as for group 5 and

7, the TMDCs show metallic behaviors; when an orbital is fully occupied (Fermi level is in energy gap) as for group 6, the TMDCs exhibit semiconducting properties.

Table 2.1 Electronic properties of TMDCs comprising different M and X atoms.¹⁴

Group	M	X	Properties
4	Ti, Hf, Zr	S, Se, Te	Semiconducting ($E_g = 0.2\text{-}2\text{ eV}$). Diamagnetic.
5	V, Nb, Ta	S, Se, Te	Narrow band metals ($\rho \sim 10^{-4}\ \Omega\cdot\text{cm}$) or semimetals. Superconducting. Charge density wave (CDW). Paramagnetic, antiferromagnetic, or diamagnetic.
6	Mo, W	S, Se, Te	Sulfides and selenides are semiconducting ($E_g \sim 1\text{ eV}$). Tellurides are semimetallic ($\rho \sim 10^{-3}\ \Omega\ \text{cm}$). Diamagnetic.
7	Tc, Re	S, Se, Te	Small-gap semiconductors. Diamagnetic.
10	Pd, Pt	S, Se, Te	Sulfides and selenides are semiconducting ($E_g = 0.4\text{ eV}$) and diamagnetic. Tellurides are metallic and paramagnetic. PdTe ₂ is superconducting.

ρ , in-plane electrical resistivity.

2.1.4 TMDC-Based Gas Sensors

Layered TMDCs are being explored as promising alternatives to graphene as gas-sensing device materials, primarily because of their sizable and tunable bandgaps.²¹⁻²⁴ Single or few-layer (2D) MoS₂ has been reported as an attractive sensing material due to a some of its properties.^{25,26} First, the sizable bandgap (1.3–1.9 eV) of layered MoS₂ markedly enhances the on-off ratio and sensitivity to a level that cannot be matched by graphene-based sensors. Second, 2D MoS₂ has a high specific surface area. Each surface atom has the ability to interact with gas molecules, thereby increasing sensitivity and detection limit. Third, 2D MoS₂ provides excellent electrical properties, such as high carrier mobility (up to 200 cm² V⁻¹ s⁻¹), low electrical resistivity, and low electronic noise.¹³ The electronic signals of MoS₂, induced by the interaction between MoS₂ and analyte gases are readily observed through appropriate electrical measurements, enabling the detection of very low concentrations of target analytes without the disturbance of electrical background signals. The aforementioned properties point out that 2D MoS₂ materials are promising candidates for

ultrahigh-sensitive gas sensors in the detection of toxic, volatile, and carcinogenic gases at room temperature.

The sensing mechanisms of MoS₂-based gas sensors in response to various inorganic gases with different elements and molecular structures (e.g., NO, NH₃) are based on charge transfer properties. As demonstrated in Fig. 2.12,²⁷ Zhang's group first reported that a few-layered MoS₂ sensor was more stable than a single-layered one, and achieved an extremely low detection limit (ppb) of NO at room temperature.

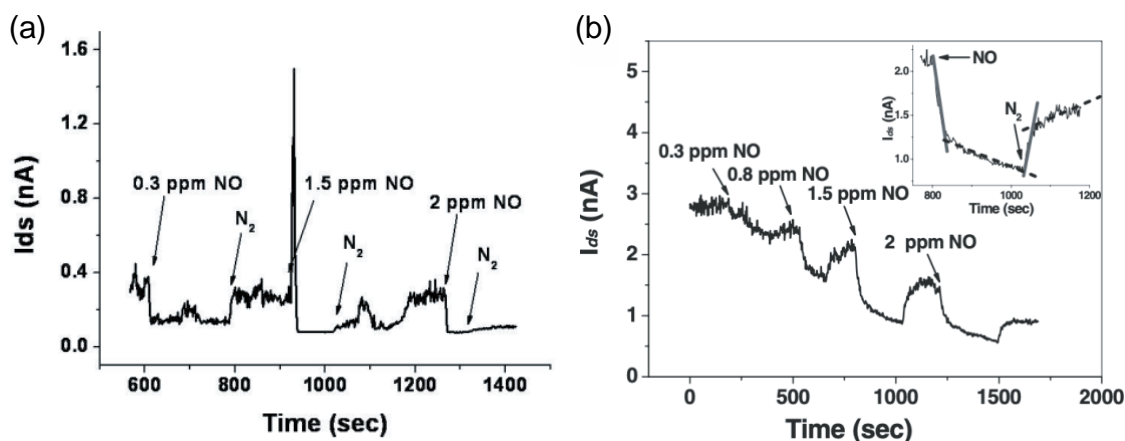


Fig. 2.7 Dynamic response curves of (a) single-layer and (b) double-layer MoS₂ sensors for NO detection.²⁷

Moreover, the influence of operating temperatures of MoS₂-based sensors on the detection of inorganic, harmful gases (NH₃ and NO₂) was studied (**Fig. 2.8**): at high temperatures, the rate of desorption was enhanced by thermal energy, resulting in an increase in recovery rate of NO₂.²⁸ 2D MoS₂-based gas sensors were also used to detect NO₂ and NH₃ in a selective manner based on an alteration of charge-transfer mechanisms as shown in **Fig. 2.9(a)** and **(b)**.²⁸ Both studies proposed the following similar sensing mechanisms. NO₂ is an oxidative gas and serves as an electron acceptor (p-doping). Therefore, upon the adsorption of NO₂ molecules onto the MoS₂, the flow of free electrons in the n-MoS₂ channel is hindered and thus causes a decrease in electrical conductivity. By contrast, reductive NH₃ gas acts as an electron donor (n-doping). Thus, when adsorbed onto the MoS₂, the NH₃ molecules donate electrons to MoS₂, rendering an increase of electron concentration and conductivity in the MoS₂.

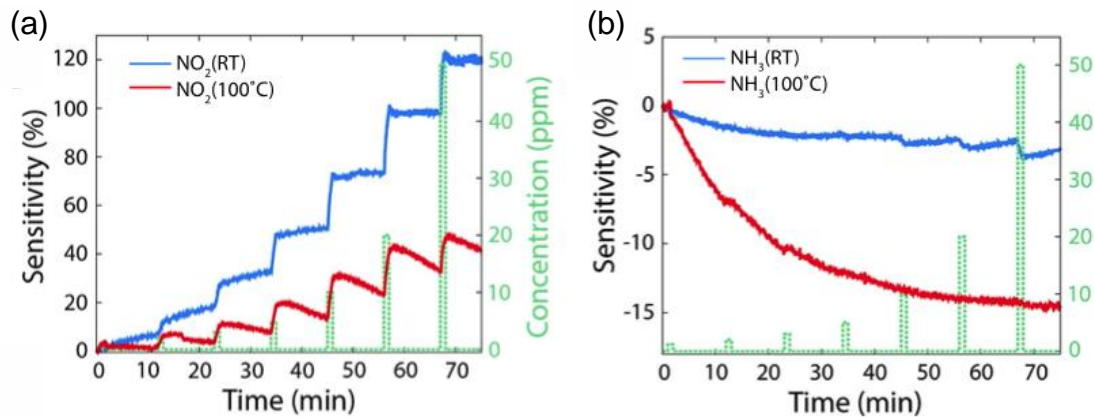


Fig. 2.8 Dynamic response curves of MoS₂-based gas sensors upon exposure to (a) NO₂ and (b) NH₃ at different temperatures.²⁸

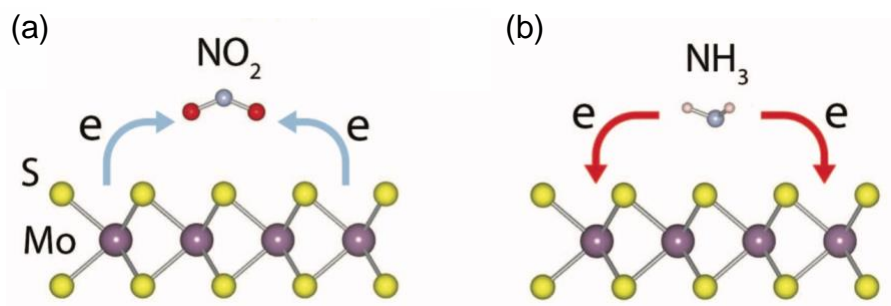


Fig. 2.9 Schematics of charge-transfer mechanisms for MoS₂ sensor in the presence of (a) NO₂ and (b) NH₃ gas molecules.²⁸

The sensing mechanism of MoS₂ in response to volatile organic compounds (VOCs) is more complicated than that of inorganic gases (NO₂ and NH₃), because it involves physisorption, chemisorption, charge transfer, and dipole-induced scattering. Perkins *et al.* reported that the selectivity and response of sensing chemical vapors for MoS₂ sensors are much higher than those for carbon nanotube (CNT) sensors (**Fig. 2.10**), indicating that the MoS₂ is more suitable than CNT for ultrahigh-selective gas-sensing applications.²⁹

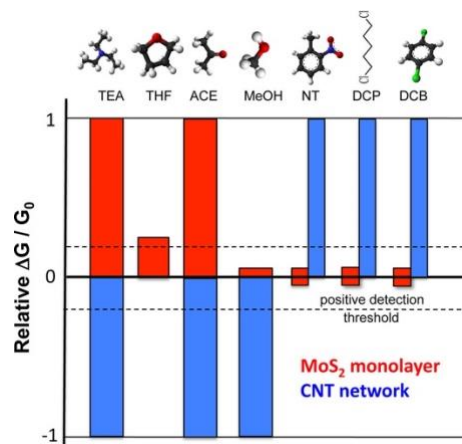


Fig. 2.10 Comparison of monolayer MoS₂ and carbon nanotube in response to triethylamine (TEA), tetrahydrofuran (THF), acetone, methanol, nitrotoluene (NT), 1,5-dichloropentane (DCP), and 1,4-dichlorobenzene (DCB).²⁹

Jung's group introduced mercaptoundecanoic acid (MUA) as a functional group to modify 2D MoS₂ gas sensors.³⁰ The mechanisms of pristine MoS₂ and MUA-MoS₂ towards sensing nonpolar [C₆H₅CH₃ and C₆H₁₄] and oxygen-containing polar [C₂H₅OH, C₂H₅COH, and (CH₃)₂CO] VOCs were studied. **Fig. 2.12(a) and (b)** depict, respectively, that the gas molecules are adsorbed on MoS₂ surface atoms or vacancy sites, and adsorbed primarily on MUA sites for MUA-MoS₂. As shown in **Fig. 2.12**, the surface modification has the advantage of increasing sensor selectivity, especially for oxygen-containing (polar) VOCs due to a modification of charge-transfer mechanisms.

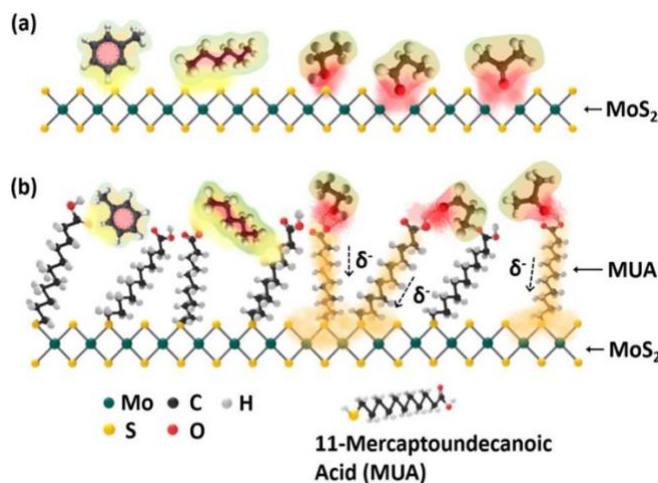


Fig. 2.11 Schematics showing the major adsorption sites of (a) MoS₂ and (b) MUA-MoS₂ in response to polar and nonpolar VOCs.³⁰

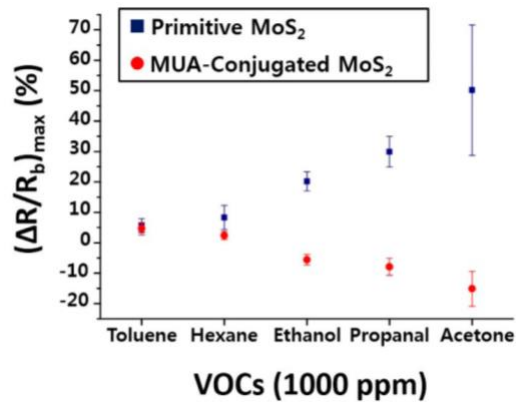


Fig. 2.12 Responsivity of pristine MoS₂ and MUA-functional MoS₂ in response to nonpolar and polar VOCs.³⁰

The polar VOCs (e.g., C₂H₅OH) are preferably adsorbed on MUA-MoS₂ through linkages between their oxygen functional groups and the exposed carboxyl groups in the MUA-MoS₂ via hydrogen bonding, subsequently creating an electron-rich region.³⁰ Then, electrons transfer toward the MoS₂ surface through the saturated alkyl chains of MUA molecules. This transfer results in a decrease in resistance of the sensing channel. By contrast, sensing of nonpolar VOCs, such as C₆H₁₄, involves dipole-induced scattering from the electron cloud of their methyl groups, resulting in a positive and small resistance change.³¹⁻³³

The detection of gases using 2D MoS₂ layered materials mainly relies on the mechanism of charge transfer, in which target analytes serve as charge donors or acceptors.³⁴ Theoretical calculations based on the density function theory were used to investigate which site was favorable for the adsorption of various gas molecules on 2D MoS₂, including the centers of hexagonal surfaces, Mo atoms, S atoms, and Mo-S bonding sites.³⁵ The gases examined were H₂, O₂, H₂O, NH₃, NO, NO₂, and CO. The charge-density-difference images (**Fig. 2.13**) revealed that O₂, H₂O, NO, NO₂, and CO act as electron acceptors to various degrees, and only NH₃ as electron donor.^{35,36} The charge transfer between 2D MoS₂ and the adsorbed gases has different quantities and flow directions (donors or acceptors), ultimately giving rise to different magnitudes of electrical signals for sensing. As an example, the resistance of 2D MoS₂ increases upon exposure to an electron-accepted gas (e.g., O₂ or H₂O), whereas their resistance decreases upon exposure to NH₃, an electron donor.³⁵ In addition, the desorption process occurs when the sensing materials are re-exposed to the air, leading to a recovery of the resistance to the initial state.

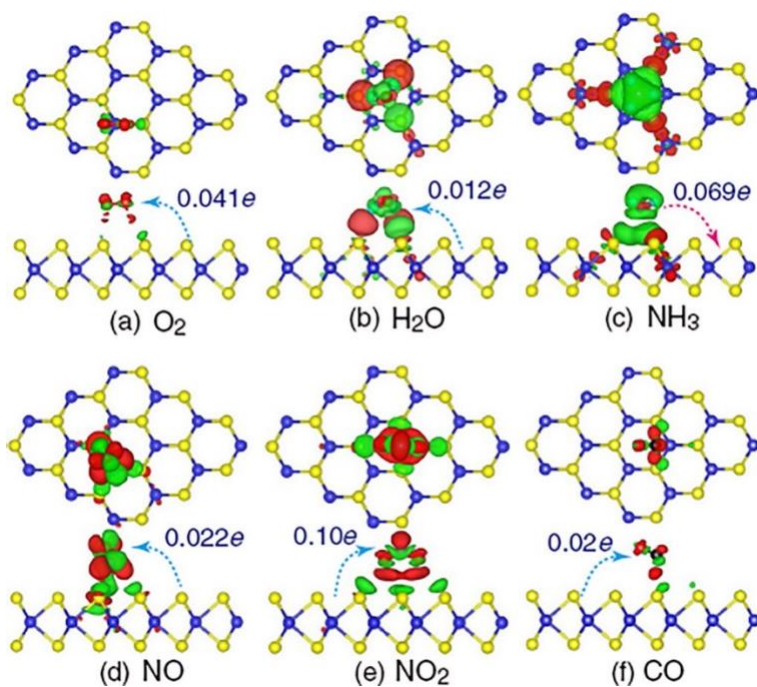


Fig. 2.13 Charge-density-difference images revealing the flow direction of charges and magnitude of charge transfer for the adsorption of (a) O₂, (b) H₂O, (c) NH₃, (d) NO, (e) NO₂, and (f) CO on 2D MoS₂.³⁵

2.2 Transition Metal Carbides/Nitrides (MXenes)

2.2.1 Structural Properties

2D transition metal carbides/nitrides (MXenes) with the general formula $M_{n+1}X_nT_x$, where M represents an early transition metal, X is carbon/nitrogen, and T_x represents surface terminations (**Fig. 2.14**). MXenes are typically prepared with three different structures, M₂XT_x, M₃X₂T_x and M₄X₃T_x, by selective etching of intermediate A layers from MAX phases, where A stands for an element of groups IIIA to VIA.⁶

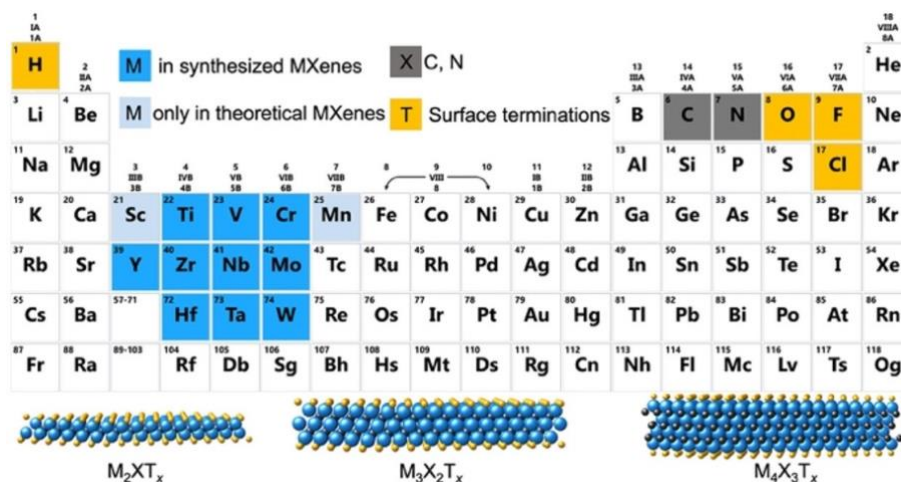


Fig. 2.14 The periodic table showing compositions of MXenes (top) and the schematics (bottom) showing the three typical structures of MXenes: M_2XT_x , $M_3X_2T_x$ and $M_4X_3T_x$.

The $Ti_3C_2T_x$ MXene has a layered hexagonal crystal structure derived from their MAX phase precursor. The transition-metal atoms are nearly close-packed with the X atoms occupying octahedral sites, as shown in the side and top views of **Fig. 2.15**. Moreover, Kajiyama *et al.* reported that the chloride terminations can be functionalized onto $Ti_3C_2T_x$ surface by etching in the Cl-containing environment.³⁷

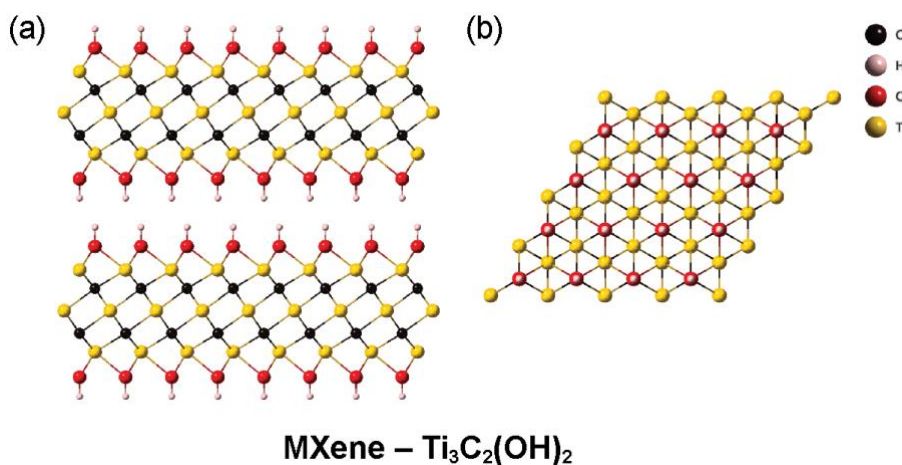


Fig. 2.15 (a) Side and (b) top views of $Ti_3C_2T_x$ MXene showing the hexagonal crystal structure with surface termination groups.

2.2.2 Optical Properties

As shown in **Fig. 2.16**, $\text{Ti}_3\text{C}_2\text{T}_x$ films exhibit a broad adsorption valley around 780–800 nm in the UV-vis transmission spectra due to the surface plasmon resonance in $\text{Ti}_3\text{C}_2\text{T}_x$.³⁸ The transmittance of the $\text{Ti}_3\text{C}_2\text{T}_x$ films varies inversely with the film thickness. For example, a 5-nm thick $\text{Ti}_3\text{C}_2\text{T}_x$ film shows a relatively flat adsorption in the visible range (≥ 450 nm) and excellent transmittance of about 93%, indicating sufficiently thin 2D MXenes have a high potential to be used as transparent conductive thin-film materials.³⁹

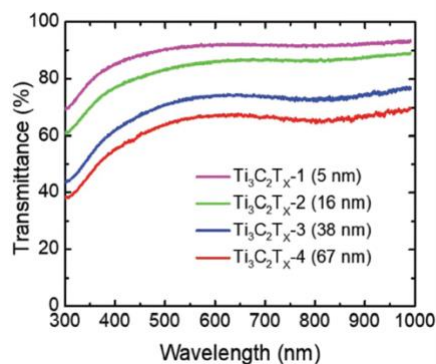


Fig. 2.16 UV-vis-NIR transmittance spectra of $\text{Ti}_3\text{C}_2\text{T}_x$ films with different thicknesses.³⁸

2.2.3 Electronic Properties

The metallic conductivity of $\text{Ti}_3\text{C}_2\text{T}_x$ MXenes ranges from less than 1000 to 9880 S cm^{-1} , depending on the sample preparation method.^{40,41} In general, a mild etching method produces MXene with less concentration of defects, thereby providing a higher conductivity. Naguib *et al.* predicted that electronic properties of MXenes could be adjusted by varying the surface termination groups. As shown in **Fig. 2.17(a)**, the $-\text{OH}$ and $-\text{F}$ terminated Ti_3C_2 MXenes exhibited a semiconductor-like behavior with a separation between valence and conduction bands of 0.05 and 0.1 eV, respectively.⁴² Furthermore, the changing of outer M layers from MXenes can also affect the electronic properties. As shown in **Fig. 2.17(b)** and **(c)** by Anasori *et al.*, after replacing the outer Ti layers with Mo layers, MXenes were converted from metal to semiconductor, yielding a band structure with a narrow band gap of 0.05 eV.⁴³

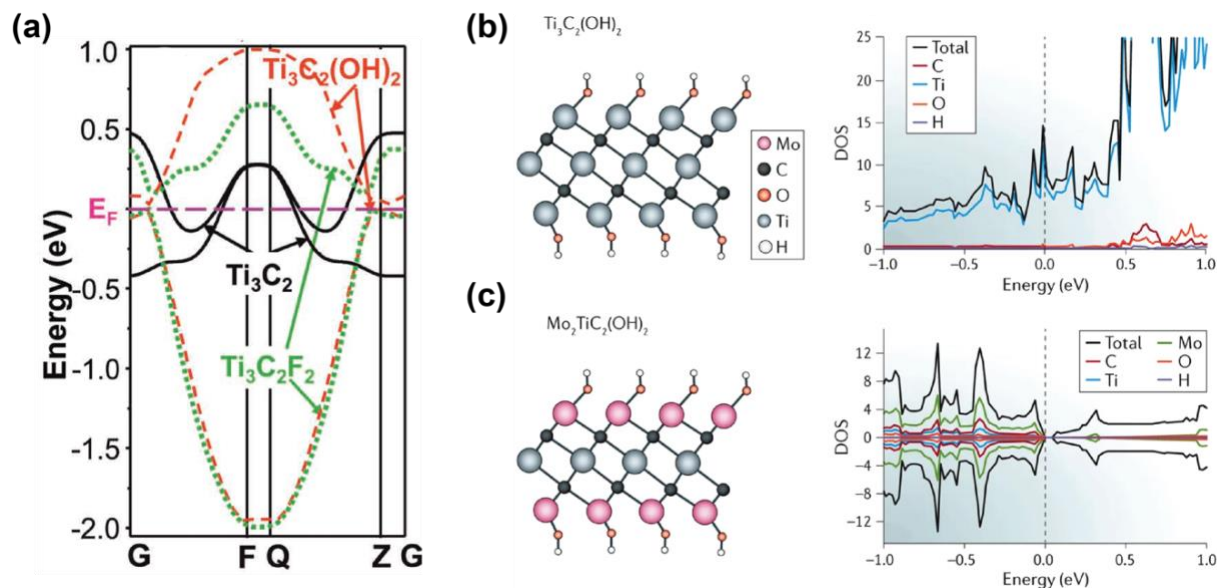


Fig. 2.17 (a) Calculated band structure of Ti_3C_2 with different surface termination groups ($-\text{OH}$ and $-\text{F}$).⁴² Calculated total density of states (DOS) of (b) $\text{Ti}_3\text{C}_2(\text{OH})_2$ and (c) $\text{Mo}_2\text{TiC}_2(\text{OH})_2$ showing a transition from metal to semiconductor by replacing outer Ti layers with Mo.⁴³

2.2.4 MXene-Based Gas Sensors

Jung *et al.* have studied the sensing behavior of metallic $\text{Ti}_3\text{C}_2\text{T}_x$ MXene and the key results are presented in **Fig. 2.18(a)-(c)**.⁷ As shown in **Fig. 2.18(a)**, the $\text{Ti}_3\text{C}_2\text{T}_x$ MXene has a highly conductive Ti_3C_2 core and its surface are fully terminated by hydroxyl ($-\text{OH}$), oxygen ($-\text{O}$), and fluorine ($-\text{F}$) groups. **Fig. 2.18(b)** demonstrates that $\text{Ti}_3\text{C}_2\text{T}_x$ sensors exhibited high selectivity toward hydrogen-bonding gases over acidic gases at room temperature. This phenomenon suggests that the hydroxyl terminal groups on the $\text{Ti}_3\text{C}_2\text{T}_x$ surface are crucial for the detection of hydrogen-bonding gases. DFT calculation results in **Fig. 2.18(c)** reveal that the hydroxyl-terminated MXene has stronger gas binding energies compared to other 2D materials (e.g., graphene, MoS_2 , BP). Moreover, $\text{Ti}_3\text{C}_2(\text{OH})_2$ exhibits a greater binding energy to acetone than ammonia. This finding is consistent with a shorter equilibrium distance of 1.23 Å for acetone, as compared to 1.81 Å for ammonia,⁷ indicating that the $\text{Ti}_3\text{C}_2\text{T}_x$ terminated with $-\text{OH}$ groups has the strongest interaction with hydrogen-bonding gases (acetone).

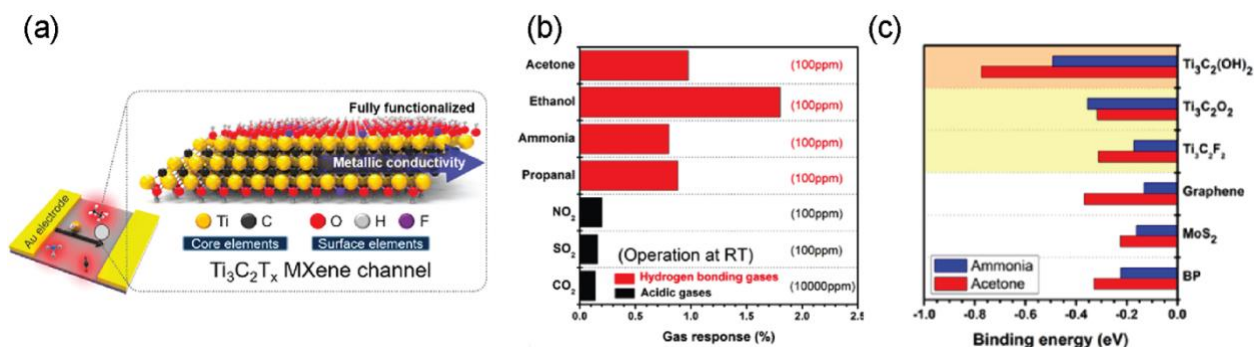


Fig. 2.18 (a) Schematic illustration of $\text{Ti}_3\text{C}_2\text{T}_x$ sensor and structure. (b) Maximal resistance changes upon exposure to various gases at room temperature (25 °C). (c) Minimum binding energies of acetone and ammonia adsorbed on $\text{Ti}_3\text{C}_2(\text{OH})_2$, $\text{Ti}_3\text{C}_2\text{O}_2$, $\text{Ti}_3\text{C}_2\text{F}_2$, graphene, MoS_2 , and BP.⁷

Moreover, the detection of gases using 2D $\text{Ti}_3\text{C}_2\text{T}_x$ MXene exhibits comprehensive positive variations of resistance regardless of gas type, indicating that the charge carrier transport channel is always impeded by the adsorption of gas molecules. This behavior is distinctive from other 2D semiconducting materials, where the resistance changes depend on the electron-donating or accepting properties of gas molecules and the dominating charge carrier type (n or p) of the sensing channel.⁷ The comprehensive increase in resistance of a $\text{Ti}_3\text{C}_2\text{T}_x$ sensor is due to the metallic properties of $\text{Ti}_3\text{C}_2\text{T}_x$, where the adsorption of gases decreases the number of charge carriers of the sensing channel.

The sensing performance of MXenes strongly depends on surface terminations. Kim's group investigated their impact on sensing performance.⁴⁴ **Fig. 2.19** displays the sensing results of a V_2CT_x sensor toward various VOCs and the associated sensing mechanism.⁴⁴ As shown in **Fig. 2.19(a)**, the V_2CT_x nanoflakes can detect various nonpolar analytes such as hydrogen (H_2) and methane (CH_4). The resistance of the V_2CT_x sensors is increased upon exposure to all reducing gases, showing the p-type sensing behavior by the charge transfer between surface terminal groups and gas analytes. The surface transition metal (V atoms) has a strong affinity to hydrogen, resulting in a highly selective detection of hydrogen.⁴⁵ **Fig. 2.19(b)** depicts the mechanism of sensing acetone (polar) and methane (nonpolar) analytes with highly oxygen-terminated V_2CT_x MXene.

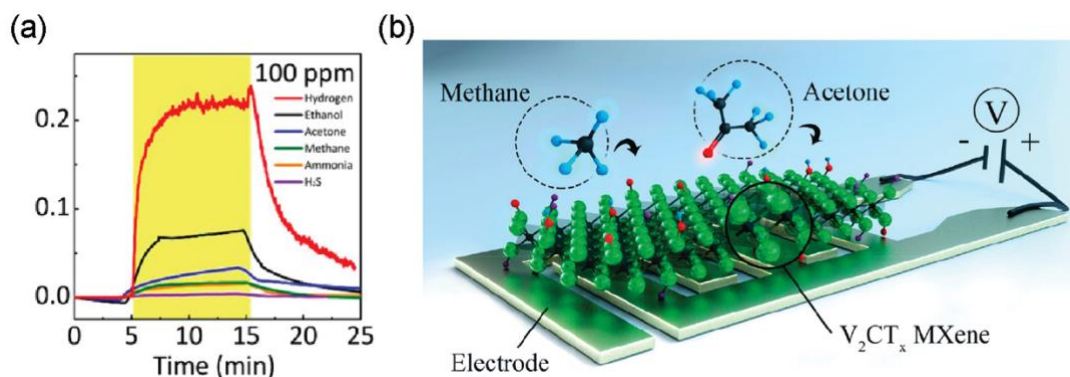


Fig. 2.19 Real-time response of V₂CT_x sensors towards various gases. (a) Schematic illustration of V₂CT_x sensor for the detection of nonpolar (methane) and polar (acetone) gas molecules.⁴⁴

The oxygen surface terminal groups act as the major gas adsorption sites, contributing to an enhanced gas-sensing performance.

2.3 Fundamental Challenges in 2D Gas-Sensing Devices

In recent years, 2D material-based gas-sensing devices have attracted great interest not only in academic research, but also in industrial applications, such as the development of electronic noses to detect (a) harmful gases to human health (b) methane gas caused by industrial pollution, (c) NO_x gas generated by automobiles, and (d) CO_x for the monitoring of air quality. The operating principle of gas-sensing devices is the monitoring of the amount of a specific gas adsorbed from an environment, which can be appropriately converted to electrical signals, such as voltage, resistance, or conductance. There are several types of solid-state gas sensors, including but not limited to conductometric (chemoresistive), catalytic combustible, electrochemical, and photoacoustic. The performance-related properties of these sensor types are summarized in **Table 2.2**.⁴⁶ Compared to traditional electrochemical sensors, 2D material-based conductometric sensors have simple device designs with the potential of yielding high responsivity, stability, portability and even at room temperature, and thus are candidates for the development of low-cost sensing devices for the internet of things (IoT) applications.

Conductometric sensors are classified into n- and p-type sensors, and their sensing properties rely on the adsorption and desorption behaviors of gaseous target analytes on the surface of sensing materials. One of the key topics for the conductometric gas sensors to be used for IoT applications is elevating response and selectivity, as well as reducing response time and detection limit, even at room temperature. These performance-related factors are primarily dependent on surface

morphology and dimension of sensing materials. A low-dimensional, porous layered material is a promising candidate for sensing applications owing to its high specific surface area.

Table 2.2 Comparison of different types of gas-sensing devices.⁴⁶

Properties/Sensor types	Conductometric	Catalytic combustion	Electrochemical	Photoacoustic
Responsivity	Excellent	Good	Good	Excellent
Selectivity	Poor	Bad	Good	Excellent
Response time	Excellent	Good	Poor	Poor
Stability	Good	Good	Poor	Good
Cost	Excellent	Excellent	Good	Poor
Portability	Excellent	Good	Poor	Bad

The working principle of a conductometric sensor is to measure the change in resistance or conductance of sensing materials upon analyte exposure.⁴⁷ The advantages of conductometric sensors are simple design, easy operation and direct measurement. Normally, the interdigitated electrodes (IDEs) are patterned on an insulating substrate, followed by depositing a sensing layer, as shown in **Fig. 2.20**.⁴⁷ The purpose of the interdigitated electrodes is to increase the contact area of the sensing material, and the change in resistance, or conductance, is directly measured from both ends of the electrodes.

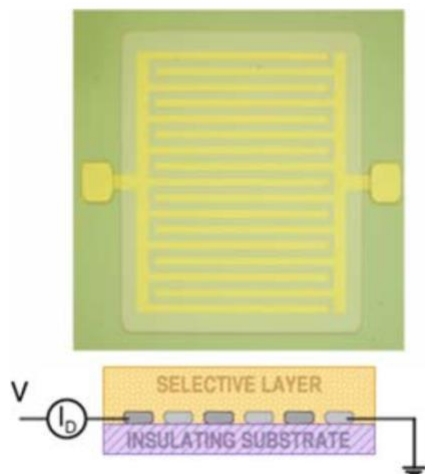


Fig. 2.20 Schematics showing the layout of interdigitated electrodes and sensing layer for conductometric sensor.⁴⁷

Sensitivity, selectivity, stability, and recovery time of gas sensors are influenced mainly by the type of sensing materials, humidity, temperature, and gas flow rate. There are several methods to improve the performance of gas sensors, such as operating the sensors at high temperatures or applying an ultraviolet light to clean the surfaces of electrode materials.^{28,48} However, a sensor operating at elevated temperature significantly increases its power consumption.

Working temperature is a significant parameter for gas sensors, and its optimization is important for the achievement of a high-performance device. Some gas-sensing materials, especially metal oxides, require high operating temperatures (e.g., > 150 °C) for the enhancement of adsorption/desorption of gases.⁴⁹⁻⁵² For example, the influence of operating temperatures of MoS₂ on the detection of NO₂ gas was studied: at high temperatures, the rate of NO₂ desorption was enhanced by thermal energy, resulting in an increase in recovery rate of the sensor. Thermal energy can excite the adsorbed gas molecules through lattice vibrations, generating a repulsive state to accelerate desorption.⁵³ Humidity is another important factor that influences sensing performance. The sensitivity of a sensor decreases in the presence of water vapors because water molecules occupy the adsorption sites, which hinders the sensing of target gases.

Gas flow rate also influences sensing behaviors. Xie's group studied the effect of total flow rates of N₂ and dry air on the detection of gas using conductive reduced graphene oxides (RGOs) as sensing materials.⁵⁴ Based on the findings of pressure changes upon exposure to various gases, they proposed the following inter-sheet sensing mechanism. Increasing the total flow rate exerts a compressive stress on the RGOs, leading to a reduction in inter-sheet distance, which in turn results in a further decrease of resistance. By contrast, the tensile stress occurs when the total flow rate is decreased. Hence, resistance of the RGOs will be increased due to an increase of inter-sheet distance.

The recent studies of VOC sensors based on 2D materials are summarized in **Table 2.3**. MoS₂-TiO₂ composites, MoO₃ nanosheets, and MoS₂-SnO₂ composites can sense tens to hundreds ppm of ethanol. However, these oxide-based composite materials require high operation temperatures ranging from 150 to 300 °C. The rest of material systems can operate at room temperature, but lack of sensitivity and selectivity to target analytes, limiting their practical sensing applications. Surface modification of materials are required to achieve high-performance, room-temperature gas sensors. 2D TMDC/MXene provides not only high specific surface area for the adsorption of gas molecules, but also potentially contributes additional active sites for surface

modification. Furthermore, surface modification and sensing principles of 2D materials for gas-sensing applications are rarely studied, and thus deserve further investigation.

Table 2.3 Summaries of key parameters and performance indicators for recent studies of sensing volatile organic compounds using various 2D materials.

Materials	Substrate	Method	Analyte	Concentration	Response	Temp.	Ref
Ti ₃ C ₂ T _x	polyimide	solution	ethanol	100 ppm	11.5 ^a	RT	55
Ti ₃ C ₂ T _x	SiO ₂ /Si	solution	ethanol	100 ppm	1.7 ^a	RT	7
3D Ti ₃ C ₂ T _x	PET	electrospinning	ethanol	10 ppm	4.4 ^a	RT	56
Ti ₃ C ₂ T _x -Na ⁺	SiO ₂ /Si	solution	ethanol	1000 ppm	9.8 ^a	RT	57
V ₂ CT _x	polyimide	solution	ethanol	100 ppm	8.1 ^a	RT	44
MUA/MoS ₂	SiO ₂ /Si	solution	ethanol	1000 ppm	20 ^a	RT	30
WSe ₂	SiO ₂ /Si	ALD	acetone	10 ppm	16.74 ^a	RT	58
MoS ₂	SiO ₂ /Si	solution	ethanol	3 ppm	1 ^a	300 °C	59
MoS ₂ /WS ₂	–	hydrothermal	ethanol	50 ppm	2 ^b	RT	60
Mo _{1-x} W _x S ₂	SiO ₂ /Si	solution	acetone	5 ppm	0.25 ^a	RT	61
Ag/WS ₂	SiO ₂ /Si	ALD	acetone	10 ppm	33 ^a	100 °C	62
Au/MoS ₂	PET	solution	acetone	10 ppm	15 ^a	RT	63
Pt/WS ₂	Al ₂ O ₃	hydrothermal	ethanol	500 ppm	9.3 ^a	RT	64
TiO ₂ /MoS ₂	Al ₂ O ₃	hydrothermal	ethanol	50 ppm	10 ^b	150 °C	49
SnO ₂ /MoS ₂	Al ₂ O ₃	hydrothermal	ethanol	50 ppm	50 ^b	280 °C	51
rGO/WS ₂	Al ₂ O ₃	hydrothermal	ethanol	30 ppm	10 ^a	33.5 °C	65
rGO/SnO ₂	PCB	hydrothermal	acetone	10 ppm	2 ^a	RT	66
graphene/ ZnO	–	solution	acetone	2 ppm	3 ^a	RT	67
graphene/MoS ₂	Al ₂ O ₃	solution	methanol	10 ppm	1.6 ^a	RT	68

^aResponse (%) = $|I_g - I_0|/I_0 \times 100$ or $|(R_g - R_0)/R_0 \times 100$, ^bResponse = I_g/I_0

3. CHARACTERIZATION OF SOLUTION-PROCESSED 2D GAS-SENSING MATERIALS

3.1 Synthesis of 2D Materials

In the early stage, the fabrication methods of layered TMDCs were the same as those of graphene. Those mechanical exfoliation methods generally involve a tape-related process to obtain small quantity of few-layered 2D materials (e.g., layered MoS₂ and WS₂), known as top-down methods. While being able to obtain high-quality MoS₂, mechanical exfoliation is difficult to achieve large quantities of layered material. By contrast, large amounts of few-layered MoS₂ can be achieved by liquid-phase exfoliation (LPE), a top-down approach. Thus, this is a high potential method to manufacture MoS₂-based sensor devices in a cost-effective manner (see the following section for a detailed discussion of the solution processing methods).

Chemical vapor deposition (CVD), a bottom-up method, is also widely used to synthesize 2D materials. Large-area MoS₂ also can be synthesized by CVD, which relies on a reaction of different precursors at high working temperatures. However, MoS₂ is quite sensitive to the pretreatment of substrates, which is a prerequisite for the improvement of layered-MoS₂ crystallinity. Zhang *et al.* have given the schematic diagrams in **Fig. 3.1(a)–(c)** summarizing the key process flows for the growth of layered MoS₂ materials using CVD with various precursors.⁶⁹

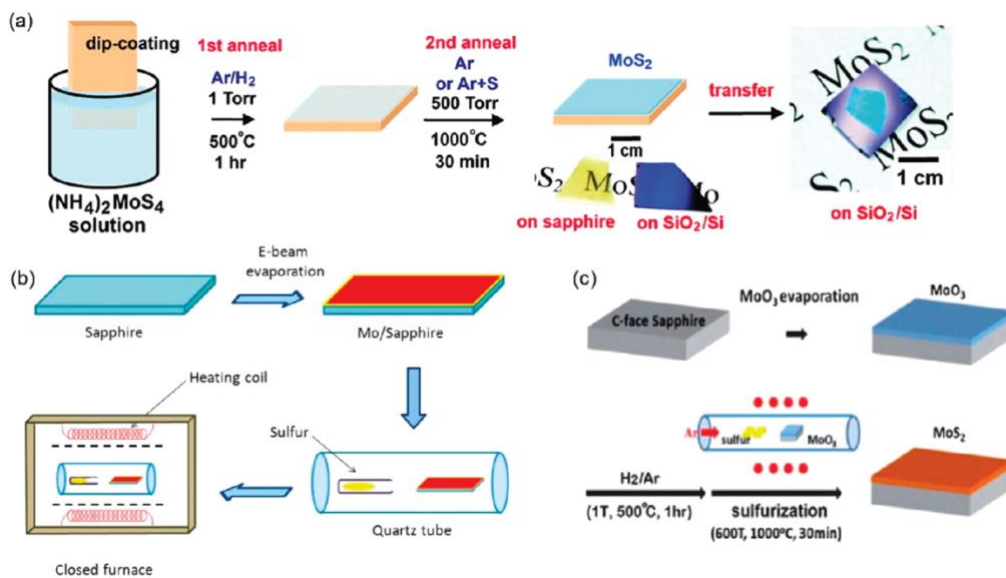


Fig. 3.1 Schematic diagrams summarizing the process flows of CVD-grown MoS₂ using various precursors: (a) ammonium thiomolybdate [(NH₄)₂MoS₄], (b) molybdenum film, and (c) molybdenum trioxide film.⁶⁹

In **Fig. 3.1(a)**, dip coating of a substrate with thiomolybdate $[(\text{NH}_4)_2\text{MoS}_4]$ is used, followed by two-step annealing (500 and 1000°C), is used to prepare low-dimensional MoS_2 . Toxic gases, such as NH_3 and H_2S , are generally involved during MoS_2 synthesis. In **Fig. 3.1(b)**, a Mo metallic thin film is pre-deposited by e-beam evaporation, which is then converted into MoS_2 through high-temperature sulfidation. In **Fig. 3.1(c)**, layered MoS_2 is fabricated by mutual reaction of two commonly used precursors, molybdenum trioxide (MoO_3) and sulfur (S). The low coverage and non-uniformity of layered MoS_2 prepared by CVD need to be addressed.⁷⁰⁻⁷²

3.1 Solution Processing of Layered TMDCs and MXenes

Fig. 3.2 illustrates that chemical solution exfoliation is classified into two broad categories: liquid-based exfoliation (LPE) and lithium-ion intercalation.⁷³ In contrast to the harsh process of lithium-ion intercalation, the liquid-based method uses a low-boiling-point solvent to exfoliate 2D materials, and thus is a mild process proven to successfully fabricate various 2D materials for sensing devices.^{9,74} In addition, lithium-intercalation is sensitive to air, whereas LPE (solvent-based) can process 2D materials in air.

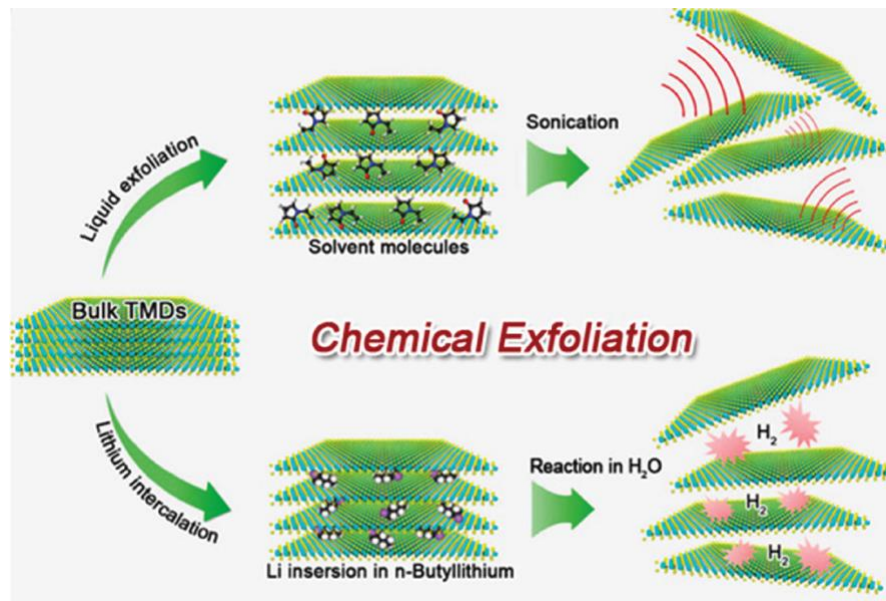


Fig. 3.2 Schematic diagram of liquid phase exfoliation (top) and Li-ion intercalation (bottom) for low-dimensional TMDC fabrication.⁷³

Ethanol, isopropyl alcohol, dimethylformamide, and NMP are commonly used solvents for liquid-phase exfoliating of various 2D materials because of their good dispersity, solubility, and

polarity. Furthermore, LPE is capable of synthesizing a variety of 2D TMDC-based materials. For example, a graphene-MoS₂ composite was synthesized by LPE using a mixture of both dispersions.⁷⁵ The MoS₂-containing solvent can be in conjunction cost-effectively with other manufacturing methods, including inkjet printing and spray coating, which are greatly beneficial to the fabrication of large-area wearable devices. However, the exfoliation level of LPE to fabricate TMDC-based 2D materials (e.g., MoS₂) is highly sensitive to power and time of ultrasonication, and thus the experimental parameters have to be optimized for mass production.

Solution etching is necessary to form 2D MXenes due to strong chemical bonds between M and A elements in MAX phases, where hydrofluoric acid (HF) or lithium fluoride (LiF)/hydrochloric acid (HCl) aqueous solution are generally used as etchant.⁷⁶ Indeed, the schematic in **Fig. 3.3**, as proposed by Gogotsi *et al.*,⁷⁷ illustrates how MXenes are produced from the MAX phases using HF etchant. The MAX phases are chemically quite stable bonded, with a combination of covalent, metallic, and ionic bonds, but the metallic A layers are chemically more reactive, resulting in a selective etching of the A layers as their bonds react differently with the HF etchant.

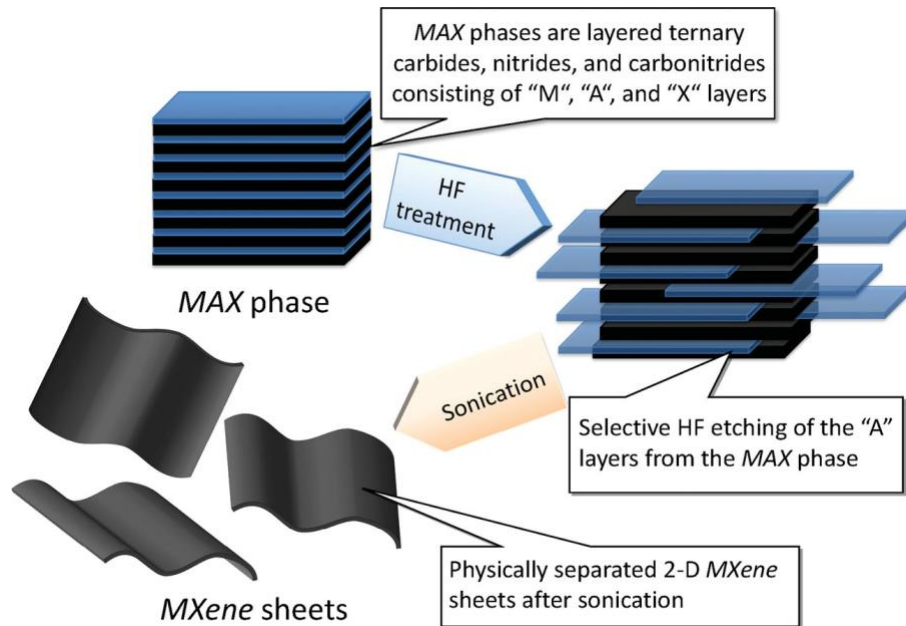


Fig. 3.3 Schematic illustrating the synthesis of MXenes from MAX phases by a selective etching process.⁷⁷

Fig. 3.4 shows the general routes of synthesizing various Ti₃C₂T_x MXene through HF etching and delamination.⁷⁶ Etching was performed by two kinds of etchants, pure HF (direct HF) and

LiF/HCl (*in-situ* HF). LiF/HCl etching is an alternative method that avoids the direct use of hazardous HF. Moreover, the use of delamination methods depends on the etching methods chosen.

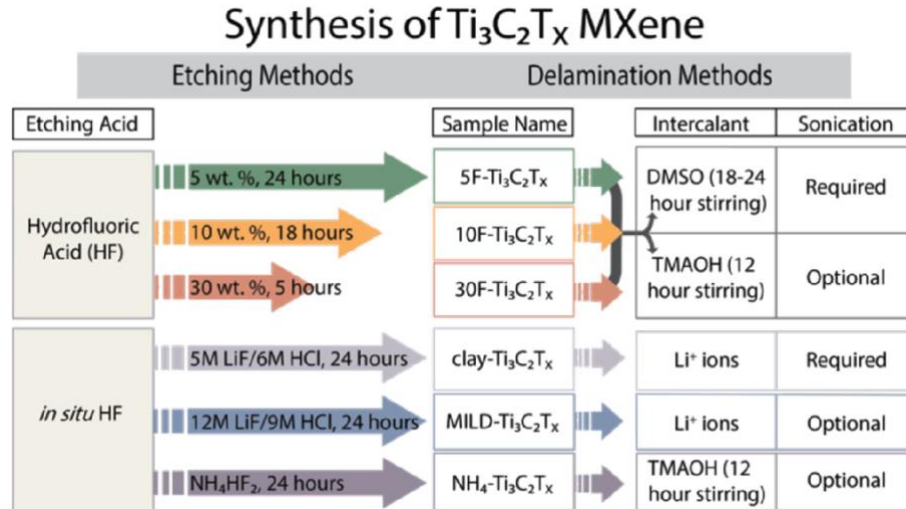


Fig. 3.4 General map for the synthesis of $Ti_3C_2T_x$ MXenes from Ti_3AlC_2 MAX phase.⁷⁶

For HF etching, the $Ti_3C_2T_x$ MXene was delaminated by introduction of dimethyl sulfoxide (DMSO) or tetramethylammonium hydroxide (TMAOH), followed by a sonication process. For LiF/HCl etching, the delamination was achieved with sonication (clay- $Ti_3C_2T_x$) or without sonication (mild- $Ti_3C_2T_x$), depending on the concentration of LiF/HCl during an etching process.

3.1 Materials Characterization

X-Ray diffractometry (XRD) is a powerful technique for the analysis of the crystal structure, lattice parameter, and interplanar spacing of crystalline materials. The diffraction peaks results from constructive interferences of scattered X-rays occurring at specific angles from each individual lattice plane shown in **Fig. 3.5**,⁷⁸ which satisfies the Bragg's law:

$$n\lambda = 2d_{hkl} \sin \theta$$

where n is the order of the reflection, λ is the wavelength of the X-rays, d_{hkl} is the interplanar spacing, θ is Bragg angle.

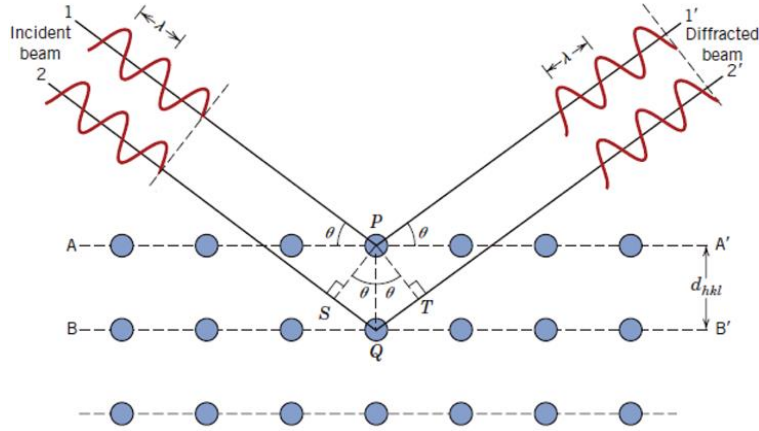


Fig. 3.5 X-ray diffraction by planes of atom.⁷⁸

In this work, high resolution XRD (X'Pert Pro MRD, Panalytical) with Cu K_{α} radiation ($\lambda = 0.15406$ nm) operating at 45 kV and 40 mA was used to characterize the crystalline structure of 2D materials. Selective results of XRD patterns of MAX Phase (Ti_3AlC_2) and as-etched MXene ($Ti_3C_2T_x$) powders are shown in **Fig. 3.6**. After the selective etching, the removal of Al from Ti_3AlC_2 is revealed by the vanishing of (104) peak at 38.9° , along with the emergence of several peaks characteristics of $Ti_3C_2T_x$.⁷⁹ The shift of the (002) peak at 9.5° to lower angle also confirms the successful delamination of 2D $Ti_3C_2T_x$ nanosheets.

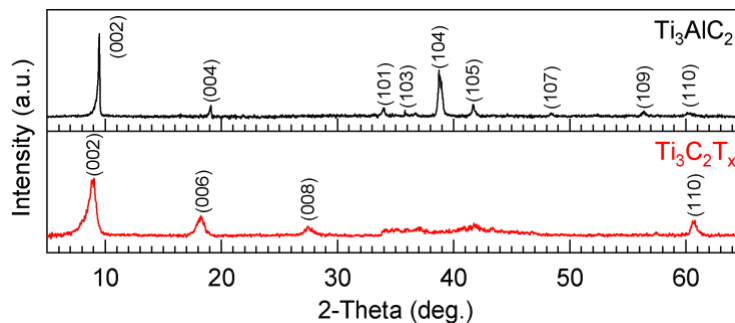


Fig. 3.6 XRD patterns of the Ti_3AlC_2 and $Ti_3C_2T_x$ powders.⁸⁰

Scanning electron microscopy (SEM; S-4800, Hitachi, 5 kV), transmission electron microscopy (TEM; TALOS 200X, FEI, 200 kV), and high-angle annular dark-field scanning transmission electron microscopy (HAADF-STEM) were used to characterize the surface morphology, crystallinity, and microstructure of 2D materials. SEM images of MAX phase

(Ti₃AlC₂) and MXene (Ti₃C₂T_x) are shown in **Fig. 3.7** Error! Reference source not found. **(a)** and **(b)**, respectively.⁸⁰ Ti₃AlC₂ MAX powders exhibit a compact morphology as expected for a bulk layered ternary carbide.

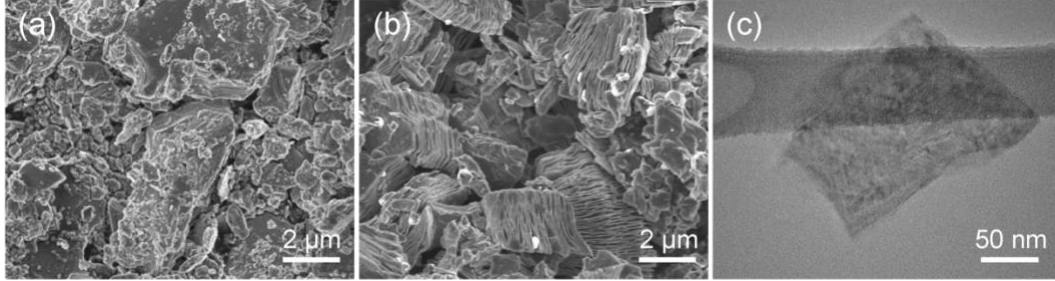


Fig. 3.7 SEM images of (a) Ti₃AlC₂ and (b) Ti₃C₂T_x.⁸⁰ (c) TEM micrograph of a single MXene nanosheet.⁸¹

The SEM imaging clearly reveals the transition from a bulk to an accordion-like structure upon the transformation of Ti₃AlC₂ to Ti₃C₂T_x nanosheets. **Fig. 3.7(c)** shows a typical TEM imaging of a single MXene nanosheet yielding clean surface and edges.⁸²

3.2 Gas-Sensing Measurements

3.2.1 Equipment Setup

In this work, gas-sensing measurements were performed in a homemade sensor testing system as shown in **Fig. 3.8**.⁸⁰ The sensors were placed in a Teflon chamber with gas inlet and outlet. The mass flow controllers (5850E, Brooks Instrument, USA) were used to control the concentration of various VOC analytes, including acetone (CH₃COCH₃), ethanol (C₂H₅OH), 2-propanol (C₃H₈O), methanol (CH₃OH), toluene (C₆H₅CH₃), hexane (C₆H₁₄), benzene (C₆H₆), by adjusting the flow rates of carrier gas and dilution gas. The bubbler containing VOC analytes was set at a controlled temperature to maintain a stable vapor pressure. The concentrations of a given VOC was calculated by equation 1 as:⁸³

$$C(\text{ppm}) = 10^6 \times \left(\frac{P_s}{P} \times \frac{f}{f+F} \right) \quad (1)$$

where C is the concentration of the VOC in ppm; f and F are the flow rates (in sccm) of the bubbling air saturated with VOC and air as dilution gas, respectively; P is the total pressure (which is atmospheric pressure in our system); P_s is the saturated partial pressure (in mm of Hg) of the VOC obtained from the following Antoine equation (equation 2), where T is the temperature, A, B, and

C are Antoine coefficients. The Antoine coefficients and associated data for vapor pressure calculations of various VOCs are summarized in **Table 3.1**.

$$\text{Log}_{10}P_s = \left(A - \frac{B}{C+T} \right) \quad (2)$$

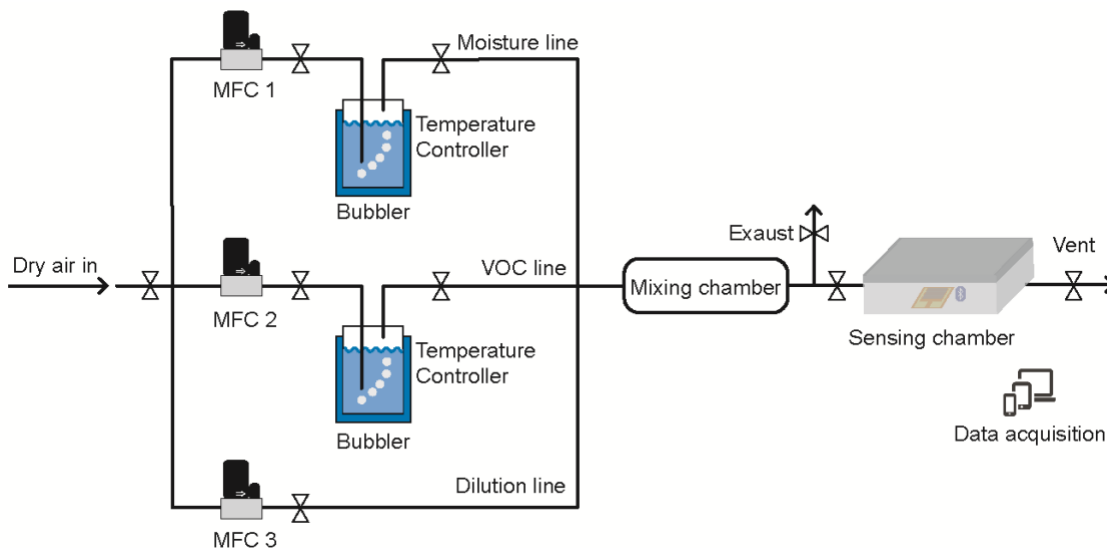
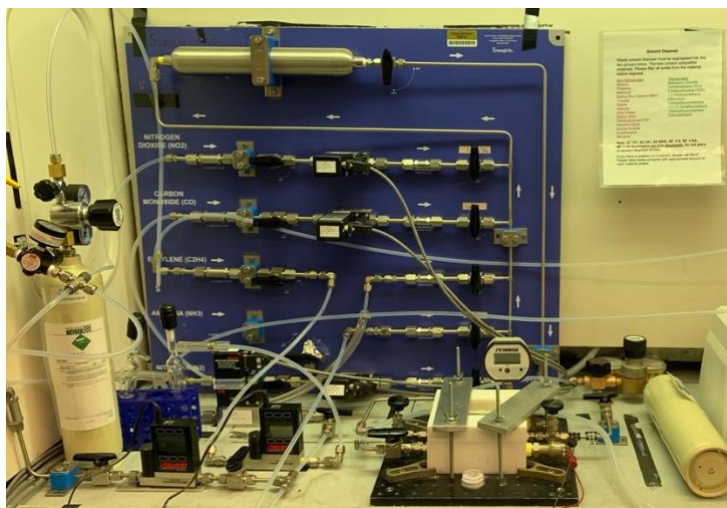


Fig. 3.8 Schematic diagram showing the setup of a homemade gas sensing system used for sensor testing.⁸⁰

The relative humidity (RH) in the chamber was monitored with a commercially available humidity sensor (HDC 2010, Texas Instruments). An input voltage of +0.1 V was applied to the sensors, and the real-time electrical signals were recorded at room temperature using a Keithley 2400 sourcemeter and a wireless sensing system.

Table 3.1 Antoine coefficients of the various solvents used for vapor sensing experiments.⁸⁴

Solvent	A	B	C	T _{min} (°C)	T _{max} (°C)
Acetone	7.31742	1315.6735	240.479	-32	234
Ethanol	8.12875	1660.8713	238.131	-5.15	241
2-propanol	7.82517	1482.1331	217.413	-0.26	235
Toluene	7.13657	1457.29	231.827	5.65	136
Hexane	6.98978	1216.9154	227.451	-24.29	92.12
Benzene	6.81432	1090.4312	197.146	-9.60	103.04

3.2.2 Wireless Sensing System

The electrical properties of the gas sensors were measured by a wireless sensing system. The corresponding functional block diagram and image of the wireless sensor system are presented in **Fig. 3.9**.⁸⁰ The wireless sensing system consists of a wireless transceiver (nRF52832 SoC), quad readout interface, 24-bit analog-to-digital converter (MCP3564) from Microchip technology, and a highly accurate humidity/temperature sensor (HDC 2010) from Texas Instruments. The transceiver features an ultralow power 32-bit microprocessor (ARM Cortex-M4F) with a built-in radio operating at 2.4 GHz ISM band, and a 512 kB flash memory for data logging. Instant signal variations from gas sensors are detected and converted into digital signals that can be wirelessly transmitted to mobile devices through the Bluetooth Low Energy (BLEs). The quad readout interface was enabled TMUX1574, a 2:1 Single Pole Double Throw (SPDT) CMOS switch with 4 channels for selecting signal from different inputs that connects into a Wheatstone bridge with a digital potentiometer (AD5241) controlled by the microprocessor via I²C bus. During operation, the digital potentiometer was adjusted automatically to match the input resistance of the sensor based on the analog-to-digital converter reading. The system was powered with a 2-stage power supply, providing dedicated power for both digital and analog circuits. The first-stage power supply was enabled with a DC-DC converter (TPS62051) from Texas Instrument and provided power for the microcontroller and the digital circuit. The second-stage power supply was enabled with a power-distribution switch (TPS2051B) from Texas Instrument for powering the analog-to-digital converter and analog circuit. This interface supported quad input simultaneously with

extremely high precision and minimal power consumption, and was powered with a CR2032 coin cell battery.

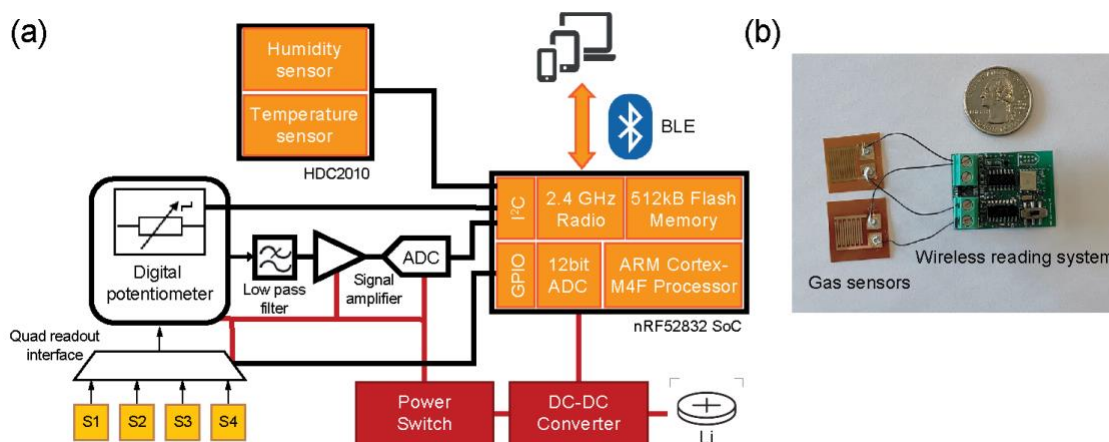


Fig. 3.9 Wireless sensor system. (a) Functional block diagram. (b) Image of a wireless-reading flexible sensor system.⁸⁰

3.2.3 Gas-Sensing Parameters

The basic principle of a conductometric gas sensor is detecting the changes in current or resistance upon gas exposure. In general, the basic performance of a gas sensor is determined by (a) gas response, (b) selectivity, (c) response/recovery time, and (d) stability, as well as operating temperature. Stability is an important factor for the evaluation of signal quality over time.⁸⁵ Sensitivity, selectivity, and response/recovery time are defined below.

(a) Gas Response

The gas response is defined as the relative change in the electrical conductance of the sensor upon gas injection compared to the baseline resistance. The gas response is defined as:

$$\Delta G/G_0 = (G_{\text{gas}} - G_0)/G_0 \times 100,$$

where G_{gas} and G_0 represent the conductance of the sensor in presence of air and target gas, respectively.

(b) Selectivity

Selectivity represents the recognition behavior of on- and off-target analytes. A good gas sensor should solely respond to the target analyte and rarely respond to off-target gases.

(c) Response/Recovery Times

Response time is defined as the time taken for conductance (or resistance) of the gas sensor to increase to 90% of a maximum value when the target gas with a specific concentration is introduced into a chamber. Recovery time is the time required to return to 90% of an initial conductance/resistance value when the target gas is turned off and the air is reintroduced into a chamber.⁸⁶

4. FLEXIBLE AU-DECORATED MoS_2 CONDUCTOMETRIC GAS SENSORS

4.1 Sensor Fabrication

Fig. 4.1 indicates that the MoS_2 -based nanoflakes, and gas sensors based on them, were prepared by the processing steps of (a) liquid-phase exfoliation of bulk MoS_2 forming 2D MoS_2 nanoflakes, (b) functionalization of MoS_2 nanoflakes with Au NPs by a solution mixing method, and (c) fabrication of sensors by drop-casting the Au-decorated MoS_2 nanoflakes onto silver interdigitated electrode printed on flexible polyethylene terephthalate (PET) substrate.

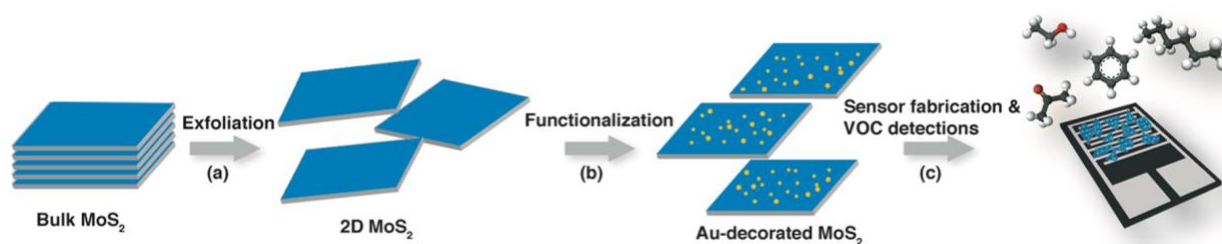


Fig. 4.1 Schematic of the process flows for the fabrication of conductometric VOC sensors on flexible substrates. (a) Liquid-phase exfoliation of bulk MoS_2 . (b) Functionalization of 2D MoS_2 nanoflakes with Au NPs. (c) Fabrication of Au-decorated MoS_2 sensors for VOC detection.⁶³

4.1 Materials Characterization

The top-view SEM imaging in **Fig. 4.2(a-c)**, including pristine MoS_2 , $\text{MoS}_2\text{-Au}(0.5)$, and $\text{MoS}_2\text{-Au}(2)$, clearly shows that MoS_2 nanoflakes have an average size of around 250 nm, and the size and coverage of Au nanoparticles increase with increasing of HAuCl_4 molar concentration. The size of Au nanoparticles on $\text{MoS}_2\text{-Au}(0.5)$ and $\text{MoS}_2\text{-Au}(2)$ are approximately 10 nm and 55 nm, respectively. As shown in **Fig. 4.2(d)**, the functionalization of Au nanoparticles onto MoS_2 nanoflakes is based on a redox reaction between the MoS_2 and noble metal ions. The work function of exfoliated MoS_2 is 5.2 eV, and its Fermi energy level is well above the reduction potential energy of AuCl_4^- (+1.002 eV versus standard hydrogen electrode; SHE).⁸⁷ Therefore, the Au nanoparticles can spontaneously attach onto the MoS_2 surface via a reduction reaction between MoS_2 and AuCl_4^- .

The high-resolution TEM and elemental mapping of high-angle annual dark-field STEM images of representative $\text{MoS}_2\text{-Au}(0.5)$ nanoflakes, shown in **Fig. 4.2(e)** and **(f)**, respectively,

indicate that the size of Au nanoparticles is about 10 nm uniformly decorated on MoS₂ nanoflakes. The HRTEM image in **Fig. 4.2(g)** presents the 9-nm-sized Au NPs. **Fig. 4.2(h)** presents the spacing measurements of MoS₂ (top) and Au (bottom) with the lattice distances of 2.7 Å and 2.3 Å, corresponding to MoS₂ (100) and Au (111) planes, respectively. The HRTEM images indicate an excellent crystallinity of the Au-decorated MoS₂ 2D materials examined here.

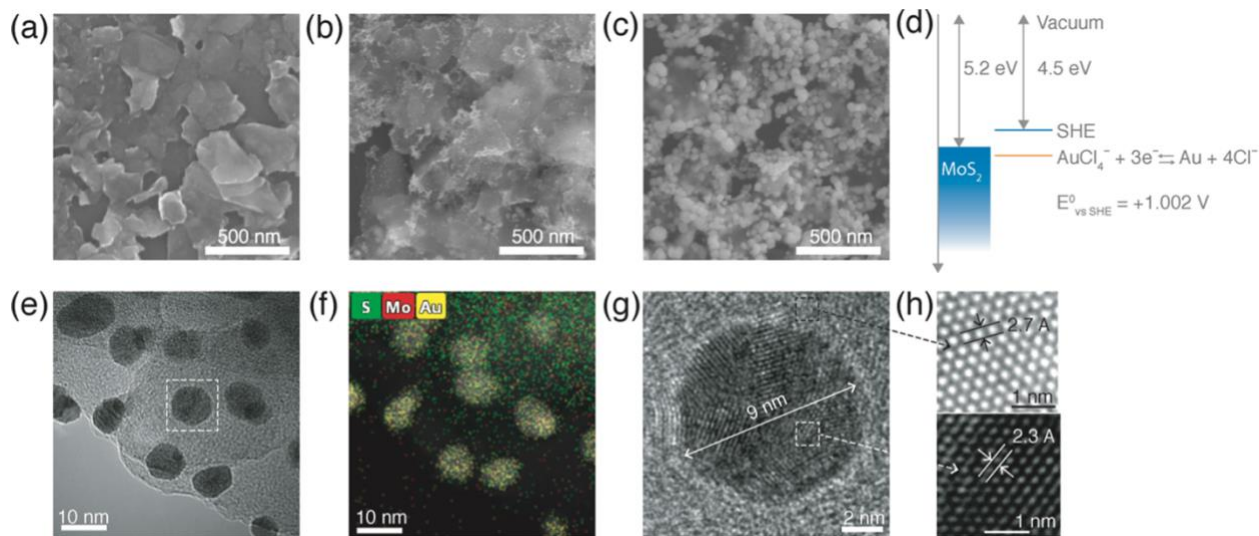


Fig. 4.2 Top-view SEM images of (a) pristine MoS₂, (b) MoS₂-Au(0.5), and (c) MoS₂-Au(2) nanoflakes, showing increase of size and coverage of Au NPs with increasing of HAuCl₄ molar concentration. (d) Energy diagram showing the relation between Fermi energy of MoS₂ and the reduction potential energy of Au³⁺ (+1.002 eV versus SHE), resulting in a spontaneous redox reaction between MoS₂ and AuCl₄⁻. (e) HRTEM image and (f) high-angle dark-field STEM image and corresponding elemental mapping of Mo, S, and Au elements for MoS₂-Au(0.5) showing a uniform distribution of Au NPs on MoS₂. (g) Enlarged HRTEM image of Au NPs on MoS₂, and corresponding (h) lattice fringes of MoS₂ (top) and Au (bottom).⁶³

X-ray photoelectron spectroscopy (XPS) was performed to identify the surface structures of MoS₂ and MoS₂-Au(0.5). The Mo 3d and S 2p XPS spectra of MoS₂ and MoS₂-Au(0.5) nanoflakes are shown in **Fig. 4.3(a)** and **(b)**, respectively. As shown in **Fig. 4.3(c)**, the Au 4f_{5/2} and Au 4f_{7/2} peaks are respectively observed at 87.68 and 84.02 eV, confirming the decoration of MoS₂ with Au nanoparticles. Notably, after Au functionalization, the binding energies of Mo 3d_{3/2} and Mo 3d_{5/2} shift from 232.03 to 232.39 eV, and 228.91 to 229.25 eV, respectively. Similarly, the binding energies of S 2p_{1/2} and S 2p_{3/2} shift from 162.93 to 163.23 eV and 161.75 to 162.01 eV, respectively. The upshifts of these peaks to higher binding energies are due to the electron-donating effect of

Au nanoparticles since its Fermi level located at the zero energy shifts toward the conduction band edge.^{44,45}

Fig. 4.3(d) shows the Raman spectra of pristine MoS₂ and Au-decorated MoS₂. The E_{12g} peak results from the opposite in-plane vibration of two S atoms with respect to the Mo atom, while the A_{1g} peak is induced by the out-off-plane vibration of only S atoms in opposite directions.¹⁷ The surface functionalization of Au nanoparticles onto MoS₂ causes a significant shift in E_{12g} and A_{1g} peaks: both E_{12g} and A_{1g} peaks are blue-shifted by 2.2 and 4.98 cm⁻¹ for MoS₂-Au(0.5) and MoS₂-Au(2) nanoflakes, respectively, indicating an electron-donating effect of Au nanoparticles on MoS₂ nanoflakes.⁸⁸

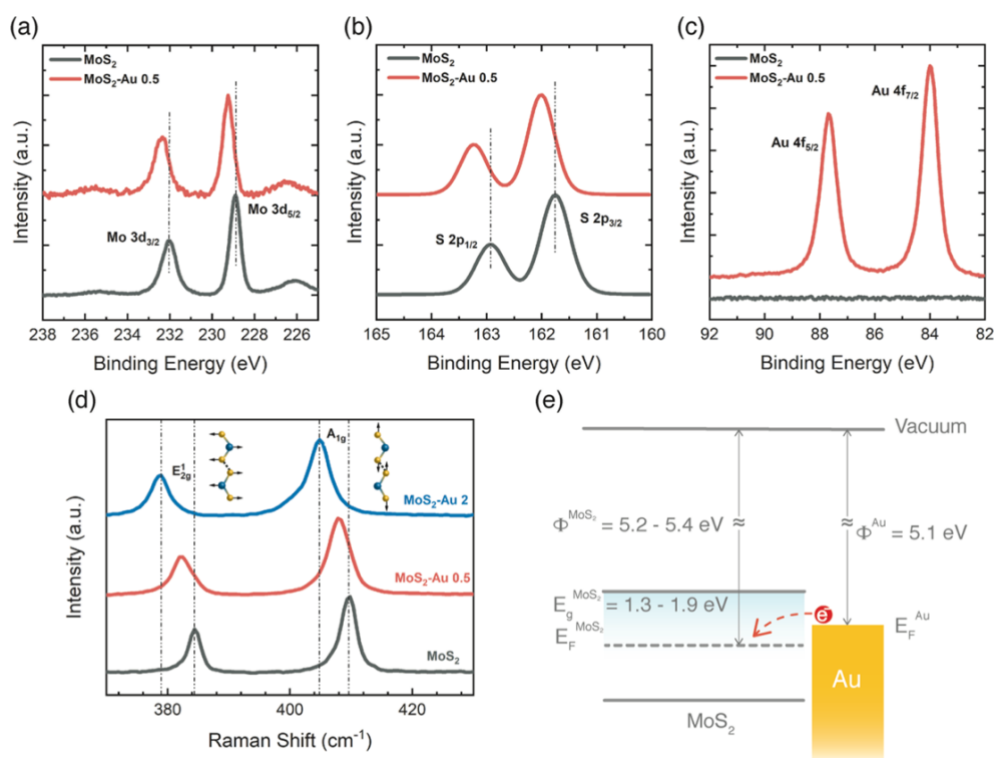


Fig. 4.3 XPS spectra of (a) Mo 3d, (b) S 2p, and (c) Au 4f for MoS₂ and MoS₂-Au(0.5). (d) Raman spectra of pristine MoS₂, MoS₂-Au(0.5), and MoS₂-Au(2) nanoflakes acquired at room temperature (λ_{ex} of 532 nm): the blue shifts in E_{12g} (in plane vibration) and A_{1g} (out-off-plane vibration) are attributed to an electron-donating effect of Au nanoparticles. (e) The energy band diagram for MoS₂ and Au, indicating electron transfer from Au nanoparticles to MoS₂.⁶³

The energy band diagram for MoS₂ and Au, as displayed in **Fig. 4.3(e)**, indicates that the transfer of electrons from Au to MoS₂. The direction of electron flow induced by the incorporation of a noble metal on MoS₂ strongly depends on the difference in work functions of the metal and MoS₂.⁸⁸

4.2 The Performance of 2D MoS₂-based Sensor Towards VOCs

4.2.1 Au Nanoparticle Size and Distribution Effect

It is crucial to optimize the decoration of Au nanoparticles for the enhancement of performance of MoS₂ conductometric gas sensors towards VOCs at room temperature. **Fig. 4.4(a)** shows that among the pristine MoS₂ and three Au-decorated (0.25, 0.5 and 1) MoS₂ sensors, the MoS₂-Au(0.5) sensor yields the highest sensitivity towards acetone (120 ppm). As suggested from imaging analysis in **Fig. 4.2**, the enhancement for the MoS₂-Au(0.5) sensor is attributed to an adequate decoration of 10-nm-sized Au nanoparticles on the MoS₂ sensing materials that induces electronic sensitization, leading to a distribution of large numbers of electrons on the MoS₂ surfaces, making them available for gas response enhancement.^{62,89} However, the MoS₂-Au(1) sensor shows no response to acetone owing to the large size and excessive number of Au NPs, leading to a metallic behavior of MoS₂ channels and thus the adsorption of acetone molecules on channel surfaces has small effect on the sensor conductivity.

The sensing performance of the MoS₂-Au(0.5) sensor were further evaluated by exposure to acetone (oxygen-based) and hexane (hydrocarbon-based) gases with concentrations ranging from 10 to 120 ppm, and the results are summarized in **Fig. 4.4(b)-(d)**. As proven by their response plots in **Fig. 4.4(b)**, the sensor exhibits much stronger response to acetone over the range of concentrations tested as compared to hexane, owing to the different degrees of molecular interaction between the sensing materials and VOC molecules as proposed in Section 4.3.4. **Fig. 4.4(c)** presents the responses of the MoS₂-Au(0.5) sensor with concentration variations of acetone and hexane. At the low VOC concentrations, the charge transfer upon gas adsorption is directly proportional to the VOC concentration due to the large active sites available on the surface. The saturation point is reached upon the increasing of the VOC concentration to a given value (about 60 ppm), resulting in a decrease in the slopes of response for both VOCs. Response and recovery times, also the important parameters for gas-sensing performance, is displayed in **Fig. 4.4(d)** for acetone, derived from **Fig. 4.4(b)**. It can be observed that the response time decreases and the recovery time increases as the acetone concentration increases over the concentrations (10 to 120 ppm). The decrease in response time with acetone concentration is attributed to the large surface active sites available for the gas adsorption; the increase in recovery time with acetone concentration is due to chemisorption of acetone molecules³⁰ and their reaction products, which do not immediately desorb from the interface.^{90,91}

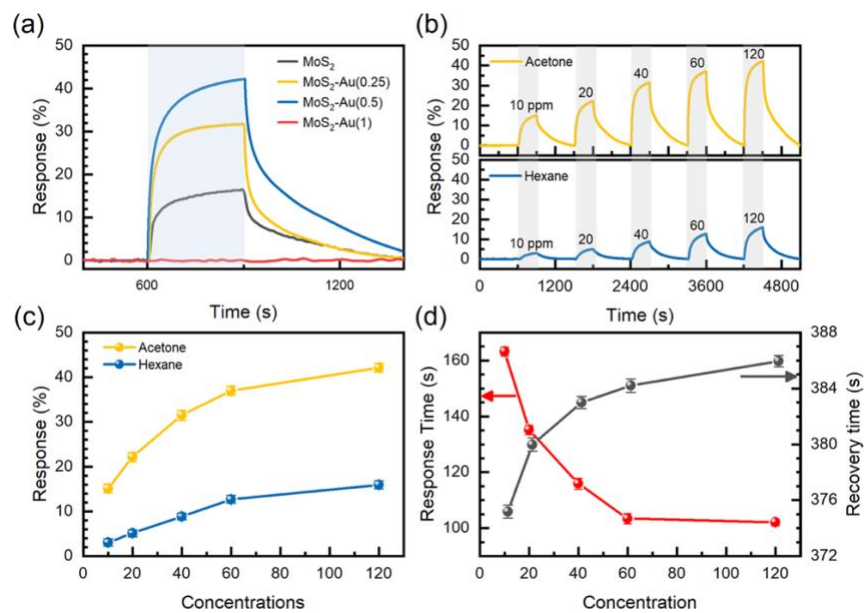


Fig. 4.4 (a) Real-time response to 120-ppm acetone by MoS₂, MoS₂-Au(0.25), MoS₂-Au(0.5), and MoS₂-Au(1). (b) Response plots of MoS₂-Au(0.5) to acetone (top) and hexane (bottom) ranging from 10 to 120 ppm. (c) Responses as a function of concentrations of acetone and hexane for MoS₂-Au(0.5). (d) Response and recovery times versus concentration curves of acetone for the MoS₂-Au(0.5) sensor derived from (b).⁶³

4.2.2 Relative Humidity Effect

Humidity is an important factor that might impact greatly the performance of 2D chemoresistive sensors.⁹² Thus, the real-time response to 10 ppm of acetone under various relative humidity (RH) levels from 10 to 80% for the MoS₂-Au(0.5) sensor was also studied. As revealed by **Fig. 4.5**, the responses of the MoS₂-Au(0.5) sensor slightly decreases at a rate of -0.15 per percentage of RH as the relative humidity increases from 10 to 60%.

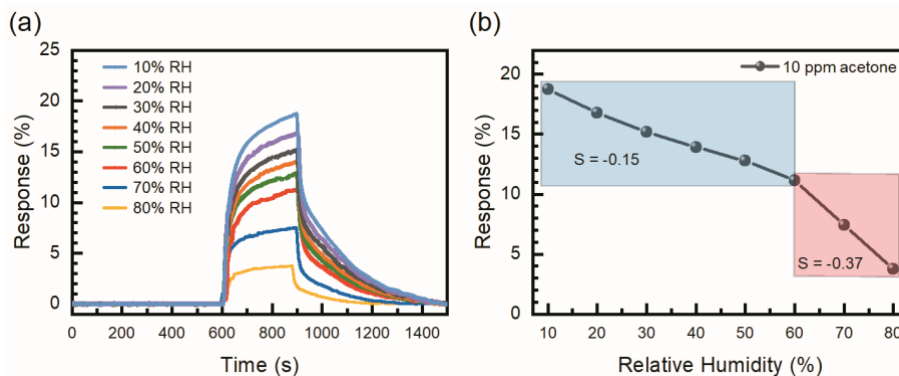


Fig. 4.5 (a) Real-time response curves of the MoS₂-Au(0.5) sensor to 10 ppm of acetone under various RH levels (10–80%) and (b) the sensing response as a function of RH levels.⁶³

Fig. 4.5 also shows that the responses dramatically decrease at a rate of -0.37 per percentage of RH over the range from 60 to 80% RH, which is attributed to the excessive occupancy of water molecules on the sensing sites, causing a decrease in sensing performance.

4.2.3 Selectivity Performance

To check the selectivity performance, the MoS₂ (as a control) and MoS₂-Au(0.5) sensors were further exposed to various VOCs, including acetone, ethanol, 2-propanol, toluene, hexane, and benzene, all with a concentration at 40 ppm, and the results are presented **Fig. 4.6(a)** and **(b)**, respectively. The maximal response changes for the MoS₂ and MoS₂-Au(0.5) sensors are summarized in **Fig. 4.6(c)**. The decoration of Au nanoparticles significantly improves the sensor's sensitivity and selectivity towards all the VOCs, particularly oxygen-containing VOCs (acetone, ethanol, and 2-propanol). For example, the response of acetone for the pristine MoS₂ sensor was only 13.7%, and was significantly improved to 31.6% by an optimal surface decoration of Au NPs for the MoS₂-Au(0.5) sensor. The mechanism for the enhancement of the oxygen-containing VOCs will be discussed in the following section.

To evaluate the reproducibility and long-term stability of sensor response, the MoS₂-Au(0.5) sensor was further tested with multiple pulses of 40-ppm acetone, and the result is depicted in the top and bottom plots in **Fig. 4.6(d)**, respectively. The sensor exhibits stable dynamic responses of 31.6% over the five consecutive cycles. The operation shelf life of the MoS₂-Au(0.5) sensor was also evaluated by testing the sensor response toward 40 ppm of acetone over a period of 30 days. The Au-decorated MoS₂ sensor reveals no significant change, demonstrating a good consistency and durability for practical sensing.

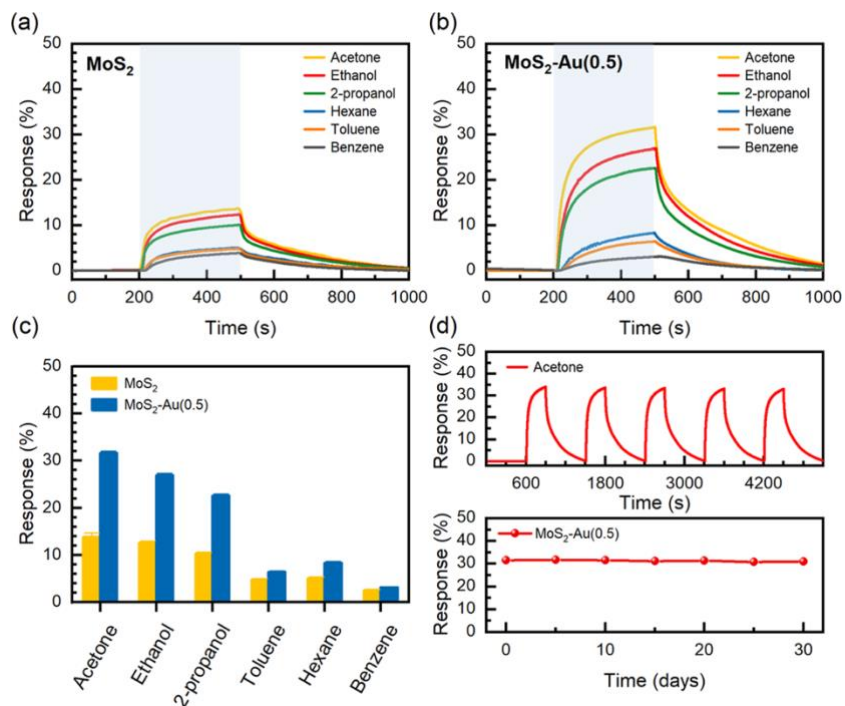


Fig. 4.6 Real-time response curves of (a) pristine MoS₂ and (b) MoS₂-Au(0.5) sensors towards 40 ppm of acetone, ethanol, 2-propanol, hexane, toluene, and benzene at room temperature. (c) Corresponding maximal response changes towards various VOCs. (d) Consecutive sensing cycles (top) and long-term stability (bottom) of MoS₂-Au(0.5) sensors toward 40 ppm of acetone.⁶³

4.2.4 Sensing Mechanism of Au-Decorated MoS₂

The interaction of a given gas molecule with MoS₂-Au sensing materials depends on its surface adsorption energy (E_a). To understand the mechanism of gas-sensing enhancement, density function theory (DFT) was thus conducted to calculate E_a of acetone molecule on MoS₂ and Au-decorated MoS₂ by the following equation:

$$E_a = E_{\text{MoS}_2\text{-Au+gas}} - (E_{\text{MoS}_2\text{-Au}} + E_{\text{gas}})$$

where $E_{\text{MoS}_2\text{-Au+gas}}$ is the total energy of the gas molecule adsorbed on MoS₂-Au, $E_{\text{MoS}_2\text{-Au}}$ is the energy of Au atom decorated on MoS₂ layer, and E_{gas} is the energy of an isolated gas molecule. The calculated adsorption energies and heights of the acetone molecule on MoS₂ and Au-decorated MoS₂ at horizontal and vertical orientation are summarized in **Table 4.1**. A larger adsorption energy value indicates a more stable configuration. The adsorption energy of acetone molecule on MoS₂-Au (-0.573 eV) is significantly greater than that on pristine MoS₂ (-0.293 eV), consistent with the extremely short equilibrium distance of 2.17 Å, implying that the superior performance of MoS₂-Au sensors in sensing acetone.

Table 4.1 Calculated adsorption energies (E_a) and heights (h) of an acetone molecule on MoS₂ and MoS₂-Au nanoflakes either at horizontal or vertical orientation.

Structure	Model gas	Orientation	h (Å)	E_a (kJ/mol)	E_a (eV)
MoS ₂	Acetone	Horizontal	2.590	28.27	-0.293
		Vertical	2.480	15.63	-0.162
MoS ₂ -Au	Acetone	Horizontal	2.170	55.29	-0.573
		Vertical	2.576	50.66	-0.526

Fig. 4.7 shows the side and top views of the most stable molecular configuration for an acetone molecule horizontally adsorbed on MoS₂-Au through DFT simulations. Stronger adsorption energy contributes to a larger amount of adsorbed gases and stronger interaction between gases and sensing materials, consistent with our experimental results on superior acetone-sensing of MoS₂-based sensor by an optimal decoration of Au nanoparticles.

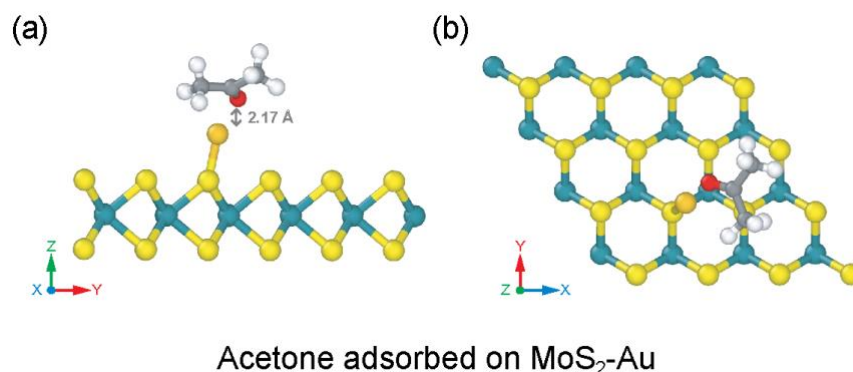


Fig. 4.7 (a) Side and (b) top views of minimum energy configurations for an acetone molecule adsorbed on MoS₂-Au surface based on DFT simulations.⁶³

The schematics in **Fig. 4.8(a)-(d)** summarize the sensing mechanisms of layered MoS₂ and Au-decorated MoS₂ towards VOCs. **Fig. 4.8(a)** depicts The sensing mechanism of hydrocarbon-based gases (hexane toluene, and benzene) using MoS₂ sensors: the interaction of these VOC molecules with MoS₂ surfaces is smaller, as electron clouds of their methyl groups induce merely dipole scattering,^{32,33} subsequently yielding a lower response. On the other hand, the response of oxygen-based VOCs (acetone, ethanol, and 2-propanol) is much stronger for MoS₂-based sensors because of the direct charge transfer mechanism. Upon adsorption of oxygen-based VOCs

(ethanol as an example) to MoS₂ surfaces, the injection of electrons occurs through direct charge transfer mechanism induced by electron-donating property of ethanol (**Fig. 4.8(b), right**), thus resulting in an increase in conductance.³⁰ Another mechanism important to the sensing enhancement involving the interaction between MoS₂, adsorbed oxygen species, and VOC molecules is also proposed (**Fig. 4.8(b), left**). In fresh air, the electrons on the MoS₂ surface are trapped by adsorbed oxygen species. Upon exposure to oxygen-based VOCs, such as acetone, the adsorbed active oxygen species react with acetone molecules and subsequently form volatile gases (H₂O and CO₂), returning the electrons back to MoS₂ channel, and ultimately causing an increase in conductance of the sensor. More importantly, the electron donating effect of Au NPs significantly increases the electron concentrations in Au-decorated MoS₂, resulting in a higher content of adsorbed oxygen species on MoS₂ surface and the trapping of more electrons from Au-MoS₂ (**Fig. 4.8(c)**). As demonstrated in **Fig. 4.8(d)**, upon exposure to oxygen-based VOCs, MoS₂ channel receives more electrons from an electron-donating process via the chemical interaction between ethanol and the adsorbed oxygen species, thus significantly improving the sensing response and selectivity in detecting oxygen-containing VOCs.

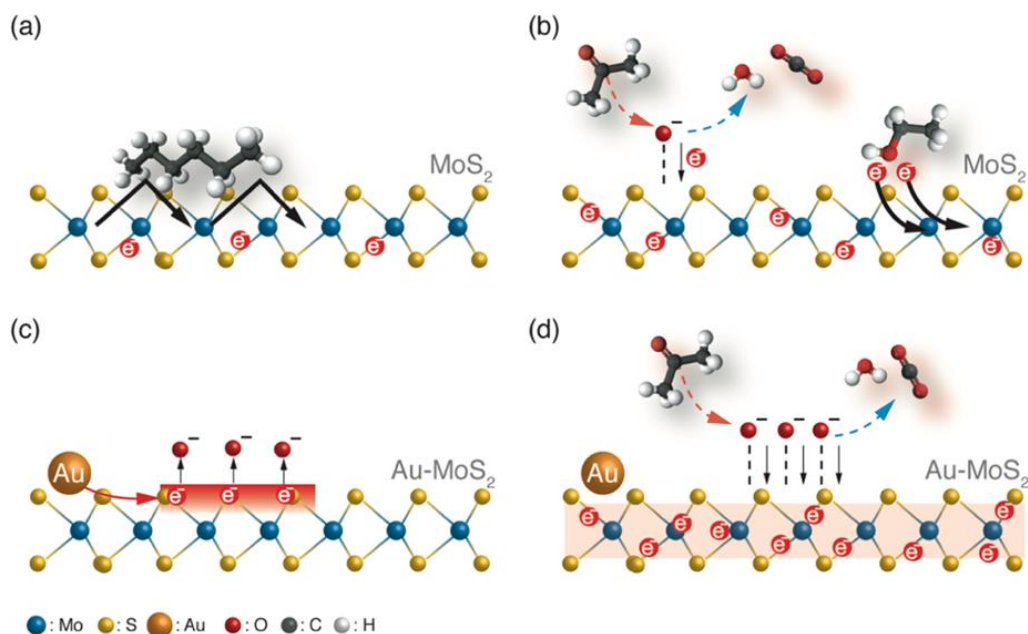


Fig. 4.8 Enhanced sensing mechanism of Au-MoS₂ hybrid materials. (a) Hydrocarbon-based VOC molecules adsorbed onto MoS₂ creating only dipole scattering through electron clouds of their methyl groups and thus contributing a small change in electrical conductance. (b) Oxygen-based VOCs adsorbed onto MoS₂ creating the injection of electrons by the electron-donating properties of ethanol (right), and the interaction between oxygen species (O₂⁻ and O⁻) adsorbed on MoS₂ creating volatile species (CO₂ and H₂O), subsequently releasing electrons back to MoS₂; both mechanisms contributing to an increase in gas response. (c) Decoration of Au NPs resulting in an increasing of electron concentration on MoS₂, leading to an increase of adsorbed oxygen species and thus (d) for the Au-decorated MoS₂ to have higher responsivity and selectivity to oxygen-based VOCs owing to the returning of more electrons species to MoS₂ channel.⁶³

5. SELECTIVE DETECTION OF ETHYLENE FOR CU(I)-PINCER COMPLEXES COATED MOS₂-SCNT

5.1 Sensor Fabrication

Fig. 5.1 shows a schematic flow chart for the fabrication of conductometric ethylene sensors based on MoS₂-SCNT films coated with Cu(I)-pincer complexes: (a) homogeneous mixture of exfoliated MoS₂ nanoflakes and SCNTs was prepared, followed by casting these materials onto Ag IDEs printed on flexible PET substrates; (b) the MoS₂-SCNT film was functionalized by depositing solutions of Cu(I)-trispyrazolylborate (Cu-Tp) **1** or Cu(I)-tris(mercaptoimidazolyl)borate (Cu-Tm) **2** (denoted respectively as **1**-MoS₂-SCNT or **2**-MoS₂-SCNT); (c) these MoS₂-SCNT sensors were operated with a wireless sensing system for ethylene detection.

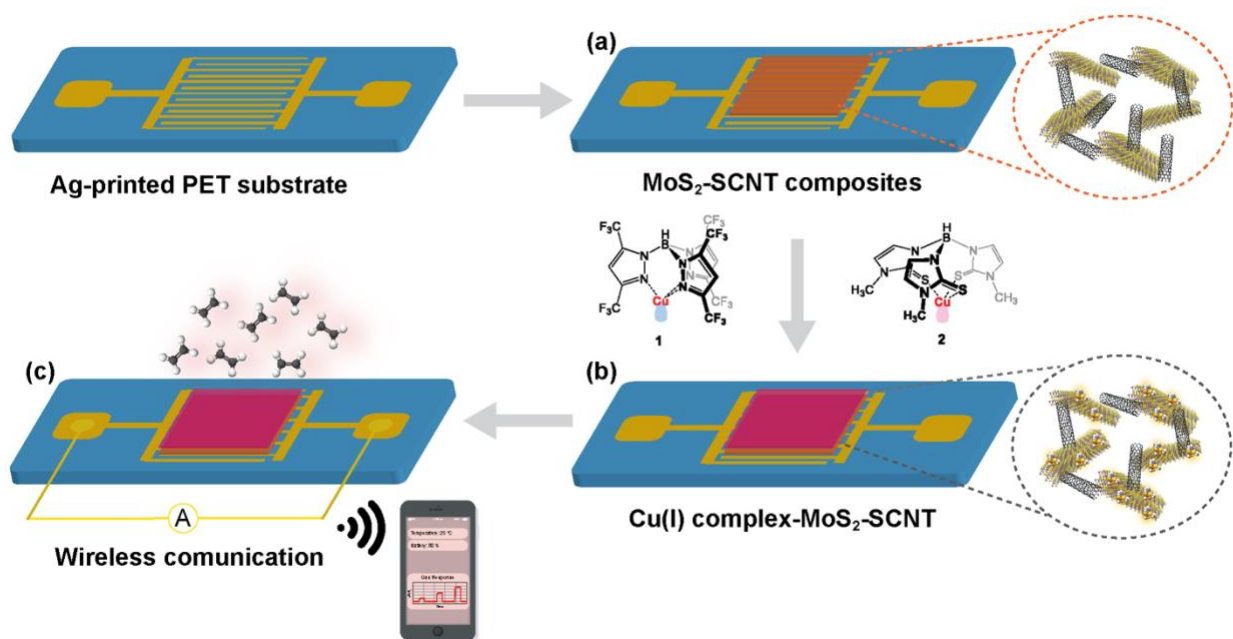


Fig. 5.1 Schematic illustration of fabrication of MoS₂-SCNT based conductometric sensors on flexible substrates. (a) MoS₂-SCNT mixture cast onto Ag IDEs screen-printed on PET substrate; (b) MoS₂-SCNT film functionalized with Cu(I)-pincer complexes (Cu-Tp **1** and Cu-Tm **2**); (c) thin-film sensors in the detection of ethylene using a wireless monitoring system.⁹³

5.1 Materials Characterization

Fig. 5.2(a)-(e) displays a set of SEM and TEM micrographs for the MoS₂-SCNT nanocomposites. The SEM micrograph (**Fig. 5.2(a)**) reveals that the exfoliated MoS₂ nanoflakes are uniformly distributed and form a three-dimensional (3D) network connected by SCNTs. This 3D network structure is highly porous and provides a high specific surface area for effective gas adsorption to enhance gas sensing. TEM image of the MoS₂-SCNT nanocomposite (**Fig. 5.2(b)**) also confirms that a single MoS₂ nanoflake is surrounded by a network of carbon nanotubes. HRTEM image of the MoS₂ nanoflake (**Fig. 5.2(c)**; top) indicates lattice fringes with a spacing of 2.7 Å, which corresponds to the (100) planes of MoS₂, and individual SCNTs ($d = 1.5$ nm) protruding from the nanoflake edge (**Fig. 5.2(c)**; bottom). High-angle annular dark-field-scanning transmission electron microscopy (HAADF-STEM) imaging and elemental mapping of C, Mo, and S elements, respectively presented in **Fig. 5.2(d)** and **(e)**, confirm the MoS₂ nanoflakes being embedded within a network of carbon nanotubes.

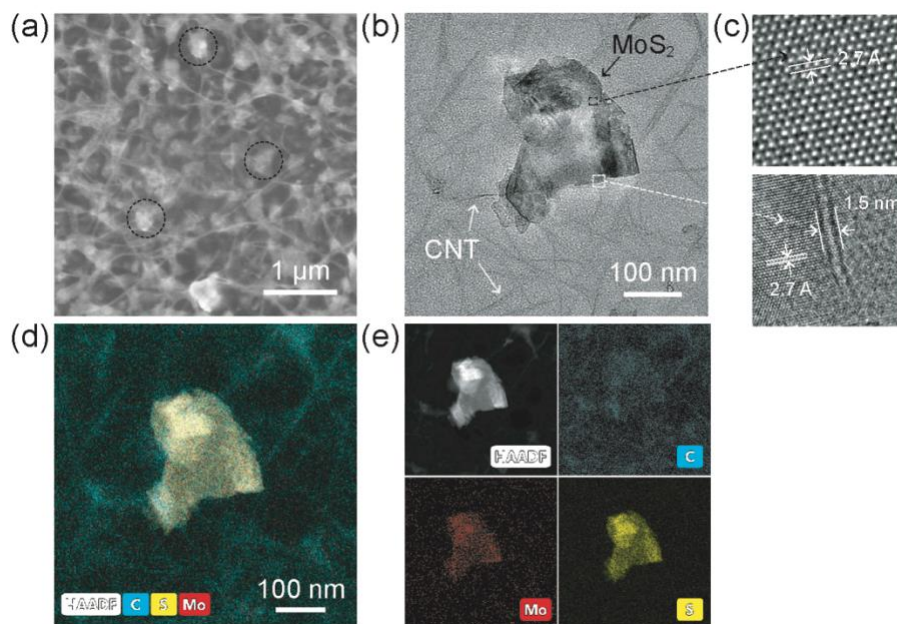


Fig. 5.2 (a) SEM image of MoS₂-SCNT nanocomposite with network-like architecture; dotted circles show individual MoS₂ nanoflakes. (b) Conventional TEM image and (c) associated high-resolution TEM images of MoS₂ (top) and SCNT (bottom), showing a lattice spacing of 2.7 Å for MoS₂ (100) plane and a diameter of 1.5 nm for SCNT. (d) HAADF-STEM image and (e) corresponding elemental mapping of the MoS₂-SCNT nanocomposite.⁹³

The doping effects of Cu–Tp **1** and Cu–Tm **2** were characterized by Raman spectroscopy, XPS, and DFT calculations. Modulations in the electronic properties of MoS₂ can be characterized by energy shifts in Raman bands^{94,95} and XPS conduction band edges,⁹⁶⁻⁹⁸ with *n*- or *p*-type doping defined by shift direction. Undoped MoS₂–SCNT produces Raman signals at 389.8 and 414.7 cm⁻¹, corresponding to the *E*¹_{2g} (opposite in-plane vibration of two S atoms) and *A*_{1g} (out-of-plane vibration of S atoms along opposite directions) vibrational modes within MoS₂ (**Fig. 5.3(a)** and **Table 5.1**).¹⁷ Deposition of Cu(I)–pincer complexes onto MoS₂–SCNT causes a significant shift in *E*¹_{2g} and *A*_{1g} peak values: in the case of **1**-MoS₂–SCNT, the upward-shifting of the peaks by less than 1 cm⁻¹ suggest modest *p*-type doping of MoS₂, whereas the *E*¹_{2g} and *A*_{1g} bands of **2**-MoS₂–SCNT are downward-shifted by more than 3 cm⁻¹, indicating strong *n*-type doping behavior.⁹⁴ By contrast, no significant changes in energy are observed for the Raman peaks at 1347 and 1590 cm⁻¹ in **Fig. 5.3(b)**, which are characteristic of the D- and G-bands of SCNTs.⁹⁹ In addition, the extremely low intensities of the D-bands in all samples imply a low density of structural defects within the SCNT networks.¹⁰⁰ The divergent roles of Cu–Tp **1** and Cu–Tm **2** as *p*- and *n*-type dopants of MoS₂, respectively, suggest a difference in the associated surface charge-transfer mechanisms,¹⁰¹ which is further supported by DFT calculations, presented in **Fig. 5.3(c)** revealing the electrostatic potential maps of Cu–Tp **1** and Cu–Tm **2**. In the case of Cu–Tp **1**, the electron density is the lowest around the Cu(I) center, mainly due to the electron-withdrawing character of the bis(trifluoromethyl)pyrazole ligands. On the other hand, the Cu(I) center of Cu–Tm **2** is electron-rich, as the *N*-methylmercaptoimidazole units donate electron density via Cu–S interactions.^{102,103}

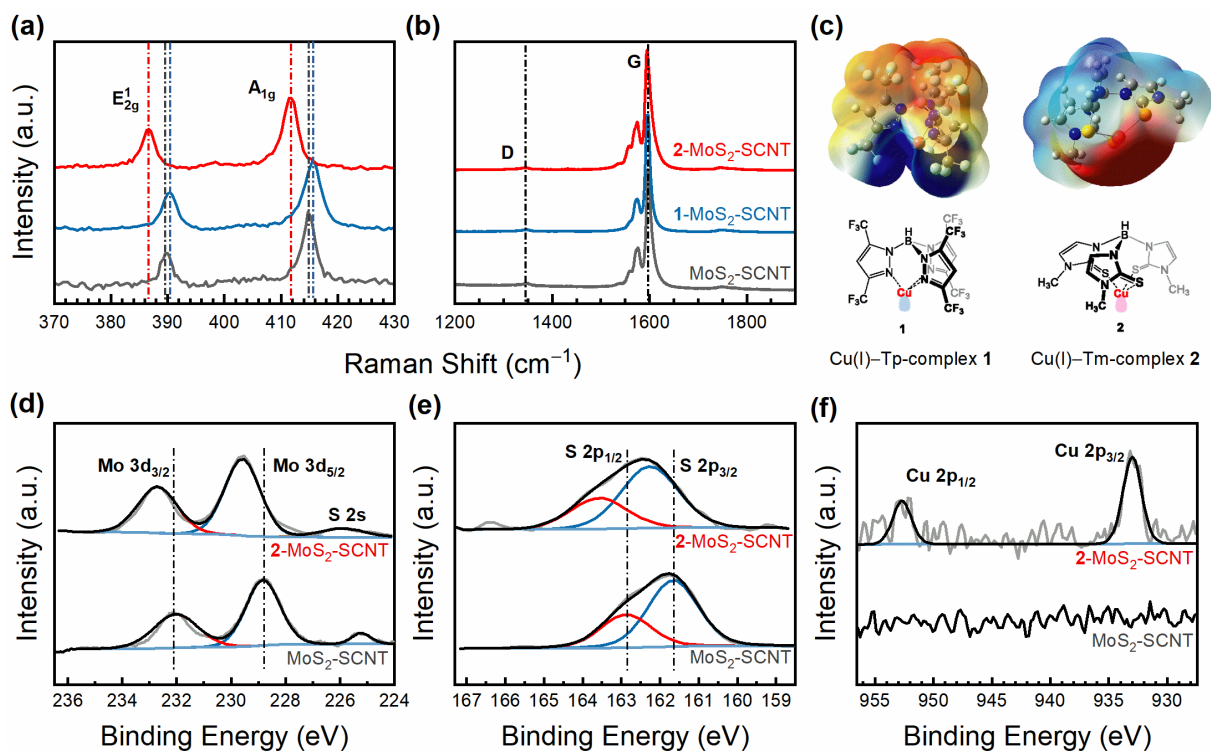


Fig. 5.3 Raman spectra, measured at room temperature (λ_{ex} 532 nm), showing (a) E_{2g}^1 and A_{1g} vibrational modes of MoS_2 and (b) D and G bands of SCNTs for MoS_2 -SCNT, **1**- MoS_2 -SCNT, and **2**- MoS_2 -SCNT. (c) Electrostatic potential maps of Cu-Tp **1** and Cu-Tm **2** indicates electron-rich (in red) and electron-deficient (in blue) surface regions, respectively. (d–f) XPS surface analysis of MoS_2 -SCNT and **2**- MoS_2 -SCNT: (d) Mo 3d region; (e) S 2p region; (f) Cu 2p region. Dashed lines indicate binding energies of the peaks before deposition of **2**.⁹³

Table 5.1 Selected Raman and XPS signals from MoS_2 -SCNT, coated with two different Cu(I)-pincer complexes.⁹³

Thin film	Raman (cm^{-1})		XPS binding energies (eV)			
	E_{2g}^1	A_{1g}	Mo 3d _{3/2}	Mo 3d _{5/2}	S 2p _{1/2}	S 2p _{3/2}
1 - MoS_2 -SCNT	390.4	415.6	--	--	--	--
2 - MoS_2 -SCNT	386.6	411.6	232.70	229.58	163.58	162.26
MoS_2 -SCNT	389.8	414.7	232.03	228.83	162.89	161.65

The strong *n*-doping effect of Cu-Tm **2** on MoS_2 is further confirmed by XPS analysis, using MoS_2 -SCNT as a reference. As shown in **Fig. 5.3(d)–(f)**, deposition of Cu-Tm **2** increases the binding energies of the peaks for Mo 3d_{3/2}, Mo 3d_{5/2}, and S 2p_{3/2} by roughly 0.7 eV (**Table 5.1** and

Fig. 5.3(d),(e)), comparable to the largest binding energy shifts reported to date for *n*-doped MoS₂.¹⁰¹ The upshift in the binding energy of MoS₂ has been attributed to a rise in Fermi energy, with a subsequent increase in electron mobility and reduction in Schottky barrier.⁹⁶⁻⁹⁸ XPS analysis (**Fig. 5.3(f)**) also confirms that **2**-MoS₂-SCNT yields the binding energy values of Cu 2p_{1/2} and Cu 2p_{3/2} at 952.7 and 933.0 eV, respectively, corresponding to copper(I) ions. This result confirms that the Tm ligand effectively prevents copper(I) from aerobic oxidation into copper(II). The relatively low signal-to-noise ratio for Cu 2p is expected, as only a few layers of Cu-Tm **2** are deposited. The results of Raman and XPS analyses, along with the DFT calculations, consistently confirm charge transfer by adsorbed Cu(I)-pincer complexes as the primary doping mechanism.

5.2 The Performance of Ethylene Sensors

5.2.1 Sensitivity and Selectivity Performance

Various MoS₂-based sensors were first exposed to 10 ppm of ethylene (C₂) for the evaluation of their sensing performance (**Fig. 5.4(a)** and **Fig. 5.5(a)**). Benefiting from surface functionalization of Cu(I) complexes, the **1**-MoS₂-SCNT, **2**-MoS₂-SCNT, and **2**-MoS₂ showed the response to C₂, producing a rapid spike in relative conductance ($-\Delta G/G_0$) upon initial C₂ exposure before settling to steady-state values, with Cu-Tm **2** far outperforming Cu-Tp **1**. The spike in $\Delta G/G_0$ indicates a transient perturbation in electronic states at the sensor surface caused by structural reorganization of Cu(I)-pincer complexes upon ethylene binding,¹⁰⁴ possibly amplified by minor changes in air flow and pressure upon switching between mass flow controllers. Moreover, the **2**-SCNT sensor was unresponsive to ethylene (**Fig. 5.5(a)**), confirming MoS₂ to be vital for signal transduction, whereas the **2**-MoS₂ sensor produced an ethylene response that was compromised by poor conductance (< 4 nS) and a high noise level (0.2%), as evaluated by the mean fluctuation in conductance prior to C₂ exposure (**Fig. 5.5(b)**). In comparison, the MoS₂-SCNT sensors revealed a 10⁵-fold increase in conductance with a noise level of approximately 0.02%, whereas MoS₂-SCNT coated with **1** or **2** experienced an additional 5-fold increase in conductance with a noise level of 0.005%, allowing a lower limit of detection for selective detection of ethylene and benefits the development of low-powered sensing devices.

While Cu(I)-pincer complexes **1** (Cu-Tp **1**) and **2** (Cu-Tm **2**) both serve as transducers of C₂ adsorption, the signal modulation observed with **2**-MoS₂-SCNT is much greater than with **1**-

MoS₂-SCNT, consistent with a stronger doping effect of Cu-Tm **2** on the semiconducting network found from the XPS, Raman results presented before. This effect is most likely dominated by charge-transfer interactions between Cu(I)-pincer complexes and exfoliated MoS₂, as the signal modulation in the control study with **2**-MoS₂ is nearly as large as that observed with **2**-MoS₂-SCNT. Previous studies have proposed similar charge-transfer interactions between Cu-Tp **1** and SCNTs,¹⁰⁵ as well as chemically induced dipole fluctuations within ultrathin layers of Cu-Tp **1** over graphene.¹⁰⁴

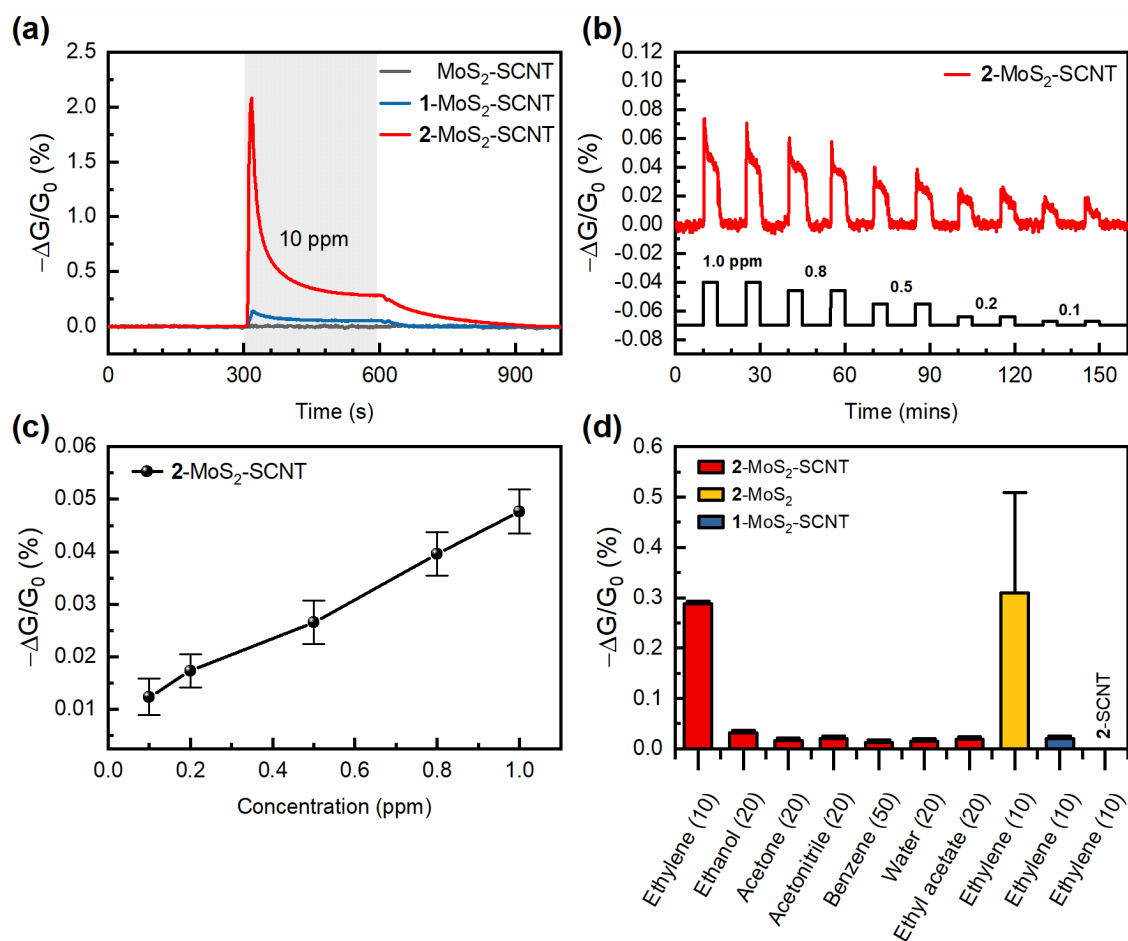


Fig. 5.4 (a) Real-time response to 10 ppm of C₂ by MoS₂-SCNT, 1-MoS₂-SCNT, and 2-MoS₂-SCNT; (b) response of 2-MoS₂-SCNT to C₂ concentrations ranging from 1.0 to 0.1 ppm; (c) steady-state response of 2-MoS₂-SCNT as a function of C₂ concentration ($\pm 1\sigma$; $N = 3$); (d) sensitivity of 2-MoS₂-SCNT to C₂ (steady-state response at 10 ppm; \pm noise) versus other volatile species (20–50 ppm). Responses of 1-MoS₂-SCNT, 2-MoS₂, and 2-SCNT to C₂ (10 ppm) provided for reference.⁹³

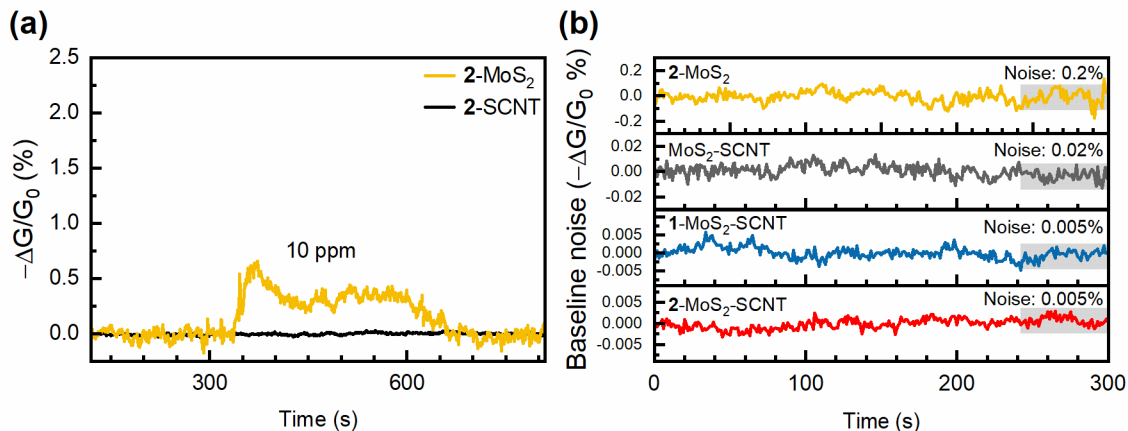


Fig. 5.5 (a) Real-time response curves of **2-MoS₂** to 10 ppm of ethylene (b) Electrical noise measurements of **2-MoS₂**, **MoS₂-SCNT**, **1-MoS₂-SCNT**, **2-MoS₂-SCNT** during nitrogen exposure.⁹³

The sensitivity, stability and detection limit of the **2-MoS₂-SCNT** sensors were evaluated by their conductometric response to ethylene or off-target analytes during continuous flow. Changes in steady-state $\Delta G/G_0$ values upon C₂ exposure were approximately linear between 1.0 and 0.1 ppm (**Fig. 5.4(b),(c)**), corresponding to a low fractional occupancy in surface adsorption. The signal-to-noise ratio at 0.1 ppm is slightly above 4, based on mean and relative standard deviation values of 1.2×10^{-2} and 0.3×10^{-2} %, respectively ($N = 3$), which represents a lower limit of detection. For selectivity tests, the **2-MoS₂-SCNT** sensors were also exposed to water vapor and various VOCs between 20 and 50 ppm, namely acetone, acetonitrile, benzene, ethanol, and ethyl acetate, with the last two commonly produced by fruit (**Fig. 5.4(d)**).¹⁰⁶ Conductometric responses to these VOCs and water were lowered by at least one order of magnitude relative to 10 ppm of C₂, confirming the selective adsorption of ethylene.

It is worth noting that experiments performed in synthetic air (79:21 N₂:O₂) indicated that the **2-MoS₂-SCNT** sensor shows a similar response to ethylene when compared to its response under a nitrogen atmosphere (**Fig. 5.6**). This behavior establishes that the sensing mechanism of the MoS₂-SCNT based sensors is dominated by reversible ethylene adsorption rather than electrochemical oxidation, as will be discussed later.

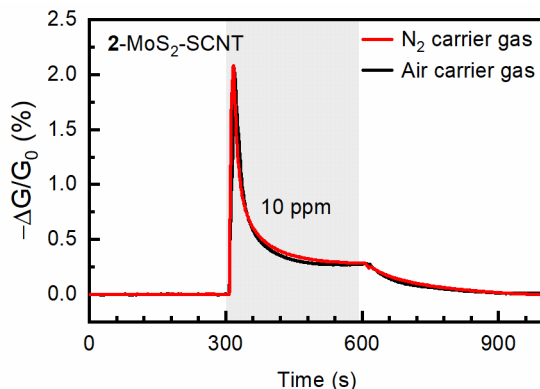


Fig. 5.6 Real-time response to ethylene (C₂; 10 ppm) by 2-MoS₂-SCNT using different carrier gases (N₂ and air).⁹³

To evaluate their potential for long shelf life, the 2-MoS₂-SCNT sensors were stored in a desiccator at standard atmospheric pressure, and removed every two days to measure their response to 1 ppm of C₂ for 5 min, with no decline in signal observed over the course of one month (**Fig. 5.7**). In practice, we have found 2-MoS₂-SCNT to be far more stable and tolerant to air exposure than 1-MoS₂-SCNT, an important consideration for future field applications.

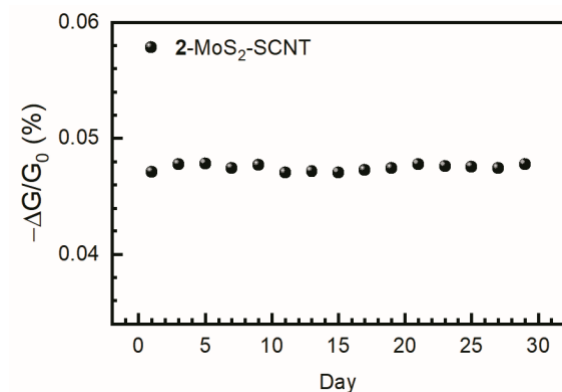


Fig. 5.7 Long-term stability of the 2-MoS₂-SCNT sensor under exposure to 1 ppm of ethylene for 5 min every two days over one month. Data points represented steady-state $-\Delta G/G_0$ values.⁹³

5.2.2 Produce Testing

The 2-MoS₂-SCNT sensors were further used to monitor ethylene from five different fruits, using a wireless system presented in Chapter 2. Fruits are classified as climacteric or non-climacteric types according to their ripening mechanisms and capacity to produce ethylene.¹⁰⁷ Both

types of fruits were obtained from a local grocery store and placed in a sealed environmental chamber at ambient temperature (21 °C) over a 24-hour window, with periodic outgassing for monitoring their C₂ emissions (**Fig. 5.8(a)**). Gas samples were passed through a filter to remove excessive humidity and CO₂ prior to C₂ readings by the conductometric sensor, which was encapsulated in a flow cell with a constant flow rate and supported by a wireless transceiver on a battery-operated platform (**Fig. 5.9**).

As expected, the 2-MoS₂-SCNT sensor registered stronger conductometric responses over time from climacteric fruits (apples, bananas, and tomatoes) than from non-climacteric ones (strawberries and oranges; **Fig. 5.8(b)**).¹⁰⁸

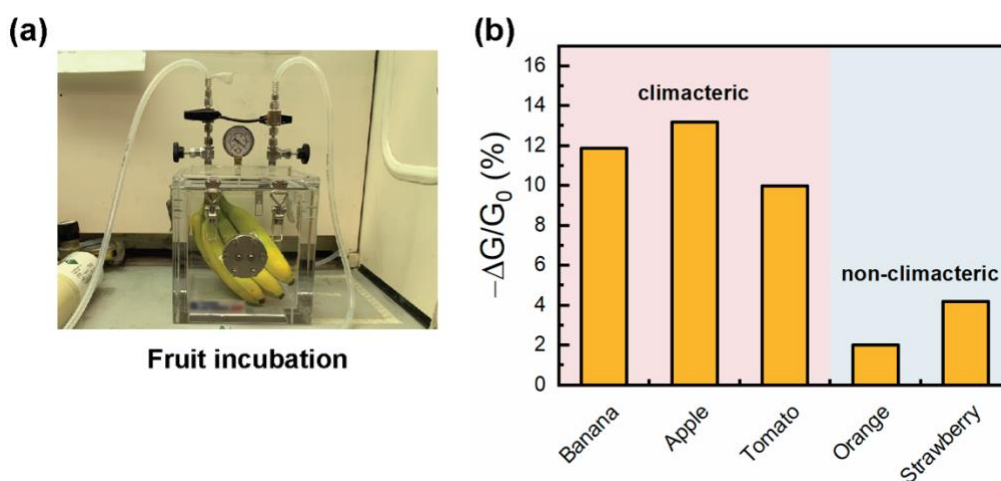


Fig. 5.8 (a) Experimental setup for monitoring ethylene released by various fruit samples at room temperature, monitored by a wireless 2-MoS₂-SCNT sensor. (b) Conductometric response of the 2-MoS₂-SCNT sensor to various fruit samples incubated for 8 h.⁹³

All climacteric fruits in this study exhibited large changes in $\Delta G/G_0$ within the first eight hours, an indicator of early-stage ripening when ethylene production rates are high.¹⁰⁹ It must be noted that while C₂ production correlates strongly with the fruit ripening process, absolute C₂ levels could vary dramatically depending on storage conditions and history, post-harvest maturation stage, and interplay with other phytohormones.¹¹⁰

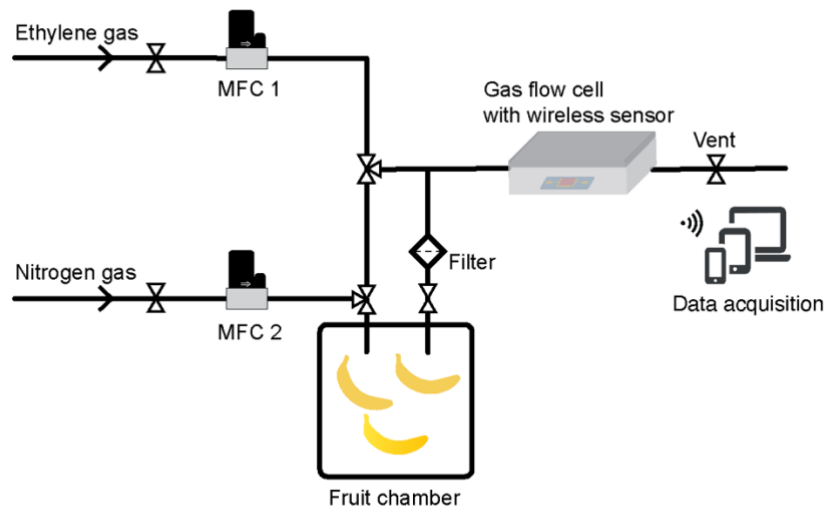


Fig. 5.9 Experimental setup for gas-sensing measurements using a wireless MoS₂-SCNT-based sensor. The masses of each fruit tested were as follows: bananas (1.09 kg), apples (1.2 kg), tomatoes (1.08 kg), oranges (1.19 kg), and strawberries (1.08 kg).⁹³

Nevertheless, our study with authentic fruit samples is sufficient to demonstrate the practical utility of the wireless 2-MoS₂-SCNT sensors for C₂ detection and monitoring in future field applications

5.2.3 Mechanism for Selective Sensing of Ethylene

The dual role of Cu-Tm **2** as a dopant of MoS₂ and a transducer of C₂ binding is illustrated in **Fig. 5.10**. The deposition of Cu-Tm **2** produces a charge-transfer effect that is likely mediated by the coordination of Cu(I) to surface atoms of MoS₂ and results in an increased charge mobility (**Fig. 5.10(b)**), as observed by a fivefold increase in conductance. When introduced, ethylene competes with the MoS₂ substrate for the Cu(I) binding site, which disrupts the charge-transfer coupling between Cu-Tm **2** and MoS₂ and decreases conductance (**Fig. 5.10(c)**). However, Cu-Tm **2** cannot be displaced from the substrate by ethylene as its volatility is negligible, so its charge-transfer interaction with MoS₂ is partially retained during gas adsorption and fully restored upon gas desorption. It was also noted that the smaller size of ethylene supports a rapid equilibration between free and surface-bound states, and may contribute selective binding in the presence of larger-sized VOC molecules.

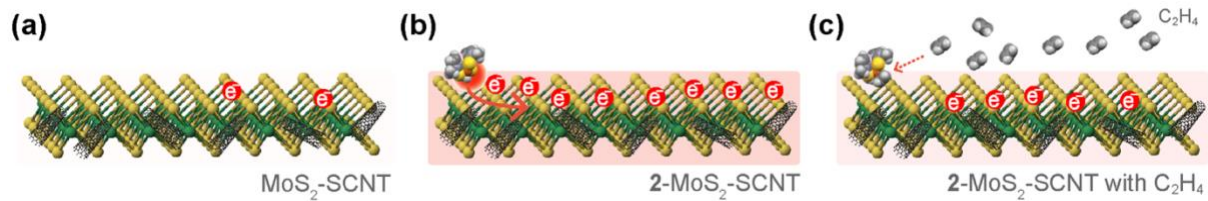


Fig. 5.10 Illustration of ethylene sensing mechanism by 2-MoS₂-SCNT: (a) semiconducting MoS₂-SCNT nanocomposite; (b) increased electron mobility due to charge-transfer interactions between Cu-Tm **2** and MoS₂-SCNT; (c) partial disruption of doping effect upon exposure to ethylene.⁹³

6. FLEXIBLE $\text{Ti}_3\text{C}_2\text{T}_x/\text{WSe}_2$ HYBRID CONDUCTOMETRIC GAS SENSORS

6.1 Sensor Fabrication

Fig. 6.1(a) shows a schematic flow for the preparation of $\text{Ti}_3\text{C}_2\text{T}_x$ nanosheets from sequential etching and exfoliating of Ti_3AlC_2 powders and $\text{CTA}^+\text{-WSe}_2$ nanoflakes from cetyltrimethylammonium bromide (CTAB) functionalized WSe_2 powders, followed by solution mixing to form $\text{Ti}_3\text{C}_2\text{T}_x/\text{WSe}_2$ nanohybrids. The $\text{Ti}_3\text{C}_2\text{T}_x/\text{WSe}_2$ nanohybrids were further prepared as ink for the inkjet printing and the fabrication of flexible VOC sensors operating at room temperature using a wireless monitoring system shown in **Fig. 6.1(b)**.

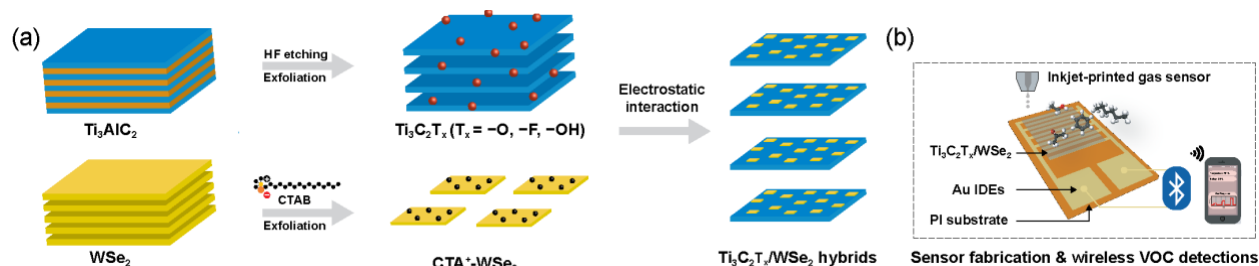


Fig. 6.1 (a) Schematic illustration of preparation processes for $\text{Ti}_3\text{C}_2\text{T}_x/\text{WSe}_2$ nanohybrids. (b) Schematic illustration of inkjet-printed sensors for wireless VOC detections.⁸⁰

6.2 Materials Characterization

SEM image reveals that the as-printed $\text{Ti}_3\text{C}_2\text{T}_x/\text{WSe}_2$ film have a uniform surface morphology over a broad range of the samples area, as shown in **Fig. 6.2(a)**. TEM image and diffraction analysis present further insight into the microstructures of the $\text{Ti}_3\text{C}_2\text{T}_x/\text{WSe}_2$ nanohybrids. The TEM bright-field image in **Fig. 6.2(b)** shows that WSe_2 nanoflakes homogeneously disperse on the $\text{Ti}_3\text{C}_2\text{T}_x$ matrix. A clear differentiable contrast in this bright-field micrograph is identified as WSe_2 has a large atomic weight, with the darker WSe_2 nanoflakes landed on the brighter $\text{Ti}_3\text{C}_2\text{T}_x$ nanosheets. The TEM image of a single $\text{Ti}_3\text{C}_2\text{T}_x/\text{WSe}_2$ nanohybrid, as presented in **Fig. 6.2(c)**, discloses (a) uniform decoration of several WSe_2 nanoflakes (typical < 30 nm) on the $\text{Ti}_3\text{C}_2\text{T}_x$ matrix (approximately 300 nm) and (b) the formation of a numerous heterojunction interfaces by the hybridization process that may benefit gas-sensing performance. Furthermore, dynamic light scattering measurements (**Fig. 6.3**) confirm that $\text{Ti}_3\text{C}_2\text{T}_x/\text{WSe}_2$

nanohybrids has an average particle size of 350 ± 100 nm. As demonstrated in HRTEM image in **Fig. 6.2(d)**, WSe₂ nanoflakes with a lattice fringe of 0.28 nm are distributed on the edges of the Ti₃C₂T_x nanosheets, corresponding to WSe₂ (100) planes.¹¹¹ Moreover, the selected area electron diffraction pattern in **Fig. 6.2(e)** shows diffraction rings (denoted as T) and diffraction spots (denoted as W), indexed as from the matrix of the hexagonal Ti₃C₂T_x nanosheets and the adsorbed WSe₂ nanoflakes, respectively. HAADF-STEM imaging in **Fig. 6.2(f)** further indicates a uniform distribution of Ti, W, and Se within the nanohybrid material.

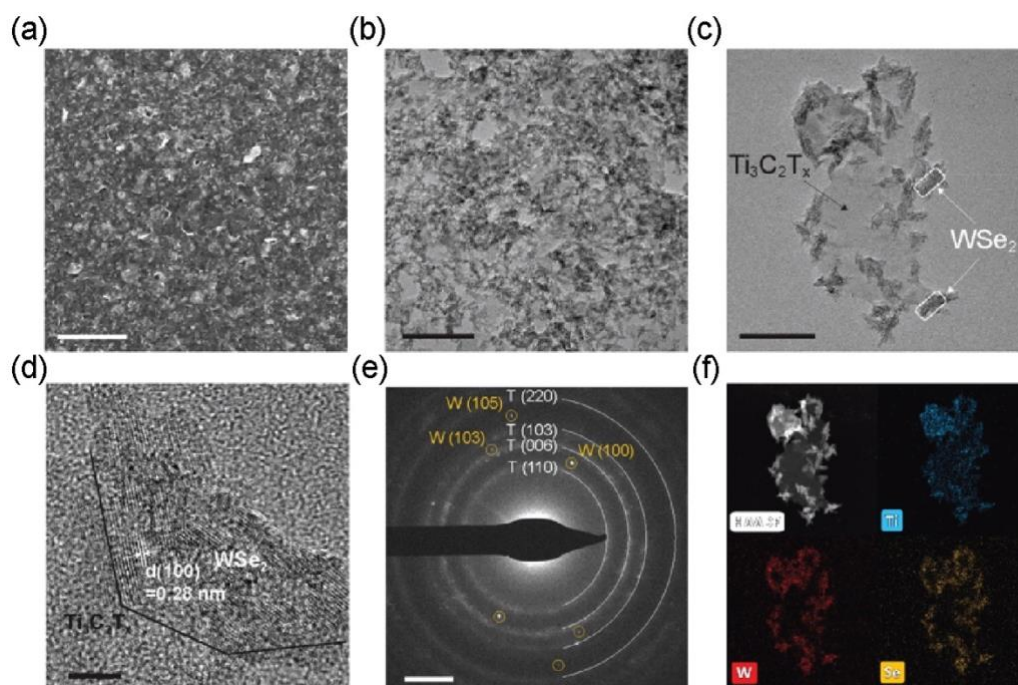


Fig. 6.2 (a) SEM image of Ti₃C₂T_x/WSe₂ nanohybrid film (scale bar, 2 μ m). (b) Low magnification TEM image (scale bar, 200 nm), with (c) showing image of a single Ti₃C₂T_x/WSe₂ nanohybrid (scale bar, 100 nm). (d) High-resolution TEM image of Ti₃C₂T_x/WSe₂ nanohybrid (scale bar, 100 nm). (e) Selected area electron diffraction pattern of Ti₃C₂T_x/WSe₂ nanohybrids (scale bar, 2 nm⁻¹). (f) HAADF-STEM image and corresponding elemental mapping of Ti, W, and Se for the Ti₃C₂T_x/WSe₂ nanohybrid showing a uniform decoration of WSe₂ nanoflakes on Ti₃C₂T_x matrix.⁸⁰

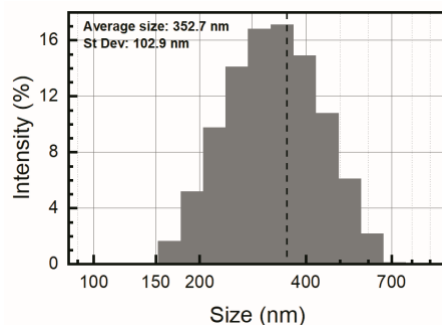


Fig. 6.3 The size distribution of $\text{Ti}_3\text{C}_2\text{T}_x/\text{WSe}_2$ nanohybrids measured by dynamic light scattering.⁸⁰

Fig. 6.4(a)-(d) respectively shows the high-resolution XPS spectra of Ti 2p, O 1s, C 1s, and W 4f, taken from $\text{Ti}_3\text{C}_2\text{T}_x/\text{WSe}_2$ nanohybrids. Interpreting these spectra can identify the chemical structures of WSe_2 nanoflakes and $\text{Ti}_3\text{C}_2\text{T}_x$ nanosheets, as well as the successful fabrication of $\text{Ti}_3\text{C}_2\text{T}_x/\text{WSe}_2$. According to **Fig. 6.4(a)**, the Ti 2p high-resolution spectrum of $\text{Ti}_3\text{C}_2\text{T}_x/\text{WSe}_2$ was fitted with four doublets (Ti 2p_{3/2} and Ti 2p_{1/2}) with a fixed area ratio of 2:1 and a doublet separation of 5.8 eV. The binding energies of the Ti 2p_{3/2} peaks were located at 454.5, 455.3, 456.9, and 458.9 eV, corresponding to Ti–C, Ti²⁺, Ti³⁺, and Ti–O, respectively.¹¹²⁻¹¹⁴ The O 1s spectrum (**Fig. 6.4(b)**) was deconvoluted into four peaks centered at 530.9, 531.7, 532.6, and 533.6 eV, corresponding to surface species of C–Ti–O_x, C–Ti–OH, adsorbed oxygen and H₂O, respectively.^{115,116} This finding suggests that the surface of the $\text{Ti}_3\text{C}_2\text{T}_x$ nanosheet indeed is terminated by an abundance of functional groups, facilitating its hybridization with WSe_2 . The C 1s spectrum in **Fig. 6.4(c)** was deconvoluted into four peaks located at 281.7, 284.8, 286.3, and 288.6 eV, corresponding to C–Ti, C–C, CH_x/CO and COO, respectively.¹¹³ As revealed by **Fig. 6.4(d)**, the $\text{Ti}_3\text{C}_2\text{T}_x/\text{WSe}_2$ also yields the binding energy values of W 4f_{7/2} and W 4f_{5/2} at 32.2 and 34.3 eV, respectively, confirming the existence of WSe_2 nanosheets.

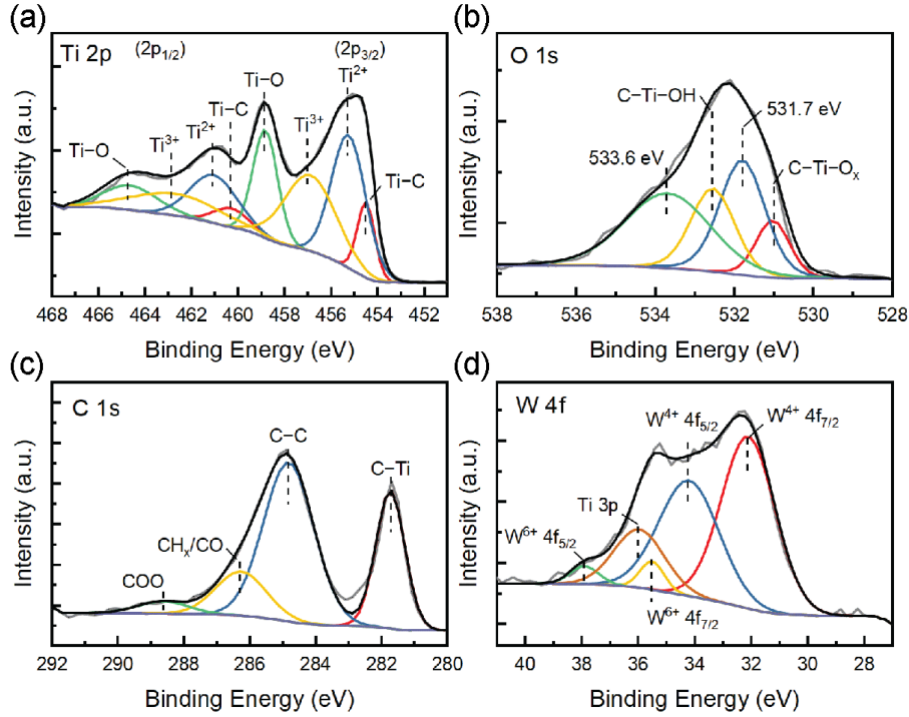


Fig. 6.4 XPS spectra of (a) Ti 2p, (b) O 1s, (c) C 1s, and (d) W 4f from $\text{Ti}_3\text{C}_2\text{T}_x/\text{WSe}_2$ nanohybrids, showing chemical compositions and bonding configurations of $\text{Ti}_3\text{C}_2\text{T}_x/\text{WSe}_2$ nanohybrids.⁸⁰

6.3 The Performance of 2D $\text{Ti}_3\text{C}_2\text{T}_x$ -based Sensor Towards VOCs

6.3.1 Composition Ratio Effect

The sensing performance of the $\text{Ti}_3\text{C}_2\text{T}_x$ decorated with 2 and 4 wt% of WSe_2 towards 40-ppm ethanol at room temperature was first examined using $\text{Ti}_3\text{C}_2\text{T}_x$ and WSe_2 as reference, and the results are presented in **Fig. 6.5(a)-(d)**. We also evaluated the electrical noises of the sensors by their mean fluctuations in conductance during air exposure, as presented in **Fig. 6.5(e)**. These measurements provides evidence for the understanding of the effect of the composition ratios and WSe_2 incorporation on the sensor performance.

The responses of $\text{Ti}_3\text{C}_2\text{T}_x$ and WSe_2 sensors were both inferior to that of the $\text{Ti}_3\text{C}_2\text{T}_x$ loaded with a moderate amount of WSe_2 nanoflakes (2 wt%), the latter yielding the strongest and fastest response towards ethanol among all the sensors tested. The response decreases as the WSe_2 amount increases from 2 to 4 wt%, owing to the excessive number of WSe_2 nanoflakes blocking heterojunctions of $\text{Ti}_3\text{C}_2\text{T}_x/\text{WSe}_2$ hybrids (proposed as the major adsorption sites), also observed from HAADF-STEM images **Fig. 6.5(f)** and **(g)**.

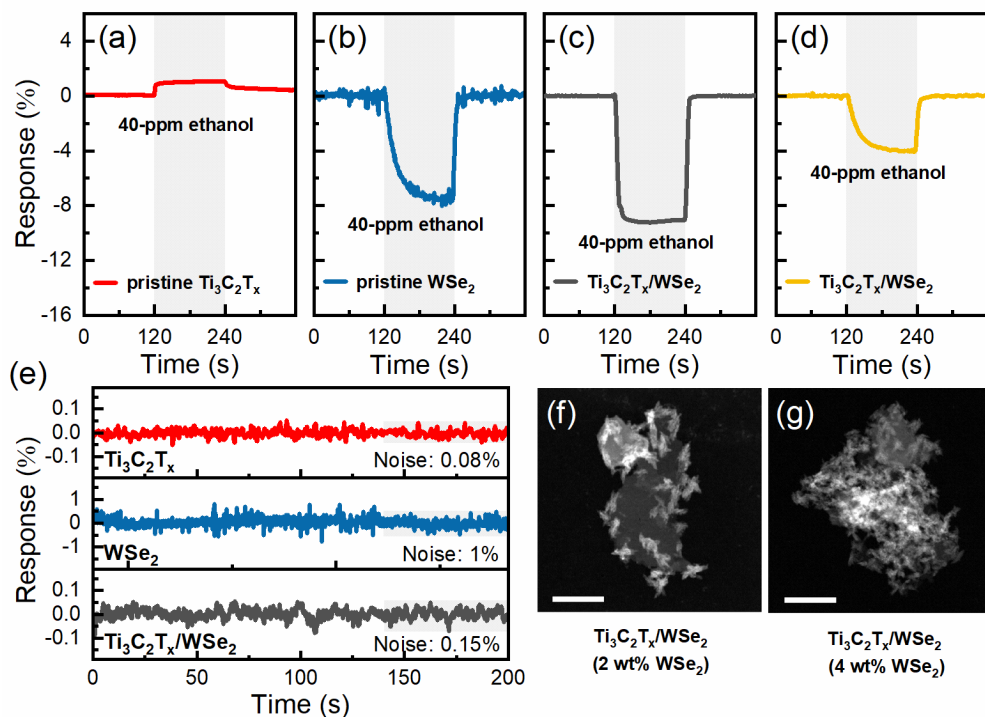


Fig. 6.5 Comparison of room-temperature sensing responses of (a) pristine $\text{Ti}_3\text{C}_2\text{T}_x$, (b) WSe_2 , (c) $\text{Ti}_3\text{C}_2\text{T}_x/\text{WSe}_2$ (2 wt%), and (d) $\text{Ti}_3\text{C}_2\text{T}_x/\text{WSe}_2$ (4 wt% WSe_2) upon exposure to 40-ppm ethanol. (e) Electrical noise measurements. HAADF-STEM images of (f) $\text{Ti}_3\text{C}_2\text{T}_x/\text{WSe}_2$ (2 wt% WSe_2) and (g) $\text{Ti}_3\text{C}_2\text{T}_x$ (4% WSe_2). Scale bars: 100 nm.⁸⁰

The electrical noise levels of WSe_2 , $\text{Ti}_3\text{C}_2\text{T}_x$, and $\text{Ti}_3\text{C}_2\text{T}_x/\text{WSe}_2$ (2 wt%) sensors were approximately 1%, 0.08%, and 0.15%, respectively. The high noise level registered for WSe_2 stems from its high electrical resistance. Moreover, the pristine WSe_2 film has a sheet resistance ($\pm 1\sigma$; $N = 3$) of $26.3 \pm 5.2 \text{ M}\Omega$ per square, whereas the $\text{Ti}_3\text{C}_2\text{T}_x$ films loaded with 2 wt% WSe_2 experienced more than 4 orders of magnitude in conductivity increase ($3.3 \pm 0.5 \text{ k}\Omega$ per square), owing to the hybridization of WSe_2 with $\text{Ti}_3\text{C}_2\text{T}_x$ having high metallic conductivity. The $\text{Ti}_3\text{C}_2\text{T}_x/\text{WSe}_2$ nanohybrid not only exhibits the highest gas response, but also displays a low electrical noise, further cementing the finding that the hybridization of MXenes with a TMDC material yields superior VOC sensing performance in conductometric devices compared to individual MXene and TMDC.

6.3.2 Film Thickness Effect

The thickness of a sensing film is an important factor affecting sensor performance. Thus, gas-sensing response of $\text{Ti}_3\text{C}_2\text{T}_x/\text{WSe}_2$ films with thicknesses of 60, 120, and 180 nm toward 40-ppm ethanol and acetone was evaluated (**Fig. 6.6**). The response of the $\text{Ti}_3\text{C}_2\text{T}_x/\text{WSe}_2$ sensors to both VOC gases decreases with increasing film thickness; this may be attributed to increasing of film thickness results in a decrease in surface-to-volume ratios of $\text{Ti}_3\text{C}_2\text{T}_x/\text{WSe}_2$ channel, subsequently impeding the transport and uptake of the VOC gases within the film.

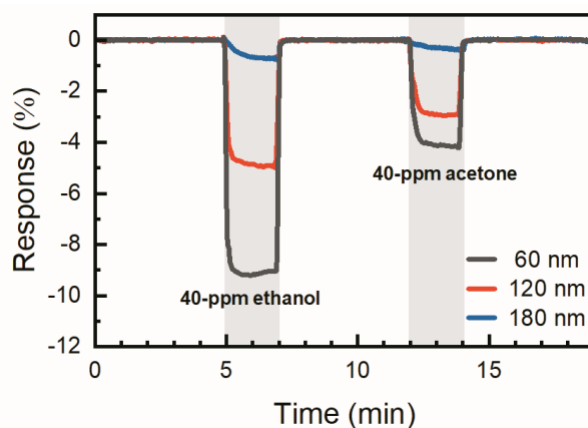


Fig. 6.6 Thickness-dependent responses of 60, 120, and 180-nm-thick $\text{Ti}_3\text{C}_2\text{T}_x/\text{WSe}_2$ films toward 40 ppm of ethanol and acetone.⁸⁰

6.3.3 Environmental and Mechanical Stability

A serious challenge for $\text{Ti}_3\text{C}_2\text{T}_x$ nanosheets being used as functional coatings or truly useful device materials is their high susceptibility to environmental degradation under humid atmosphere or in aqueous solution.¹¹⁷⁻¹¹⁹ Thus, sensing experiments were performed by selecting water vapor over a wide range of relative humidity (RH) levels, from 5 to 80%, as an interference component for the testing environmental stability of the $\text{Ti}_3\text{C}_2\text{T}_x/\text{WSe}_2$ sensors using pristine $\text{Ti}_3\text{C}_2\text{T}_x$ sensors as control (**Fig. 6.7**). **Fig. 6.7(a)** shows small changes in electrical conductance of the $\text{Ti}_3\text{C}_2\text{T}_x$ and $\text{Ti}_3\text{C}_2\text{T}_x/\text{WSe}_2$ films in the dry environment (5% RH) over a period of 10 days. However, after exposure to 80% RH humid environment, the conductance of $\text{Ti}_3\text{C}_2\text{T}_x$ dramatically decreased to 21% of initial conductance and did not recover at all in dry environment (5% RH), whereas the $\text{Ti}_3\text{C}_2\text{T}_x/\text{WSe}_2$ remained 88% of initial conductance, and recovered to 92% in dry environment (**Fig. 6.7(b)**). The responses of the $\text{Ti}_3\text{C}_2\text{T}_x/\text{WSe}_2$ sensors to 40 ppm of ethanol under various RH

levels from 5 to 80% were also measured, presented in **Fig. 6.7(c)** and **(d)**. The response of the $\text{Ti}_3\text{C}_2\text{T}_x/\text{WSe}_2$ sensors changed from -12% to -6.1% as the humidity level increased from 5 to 80%, indicating that although there is a humidity effect, the hybrid sensor is still functioning well in high humidity environment. The decrease in response under elevated RHs is attributed to partial occupancy of water molecules on the sensing sites, causing a decrease in sensing performance.¹²⁰ The $\text{Ti}_3\text{C}_2\text{T}_x/\text{WSe}_2$ hybrid sensors effectively detects ethanol under an extremely high humidity level of 80%, indicating that decorating of WSe_2 on the edges of $\text{Ti}_3\text{C}_2\text{T}_x$ nanosheets is an effective way to block the direct interaction of H_2O with MXenes, which thus is an approach to promoting MXene materials for real-life sensor applications.

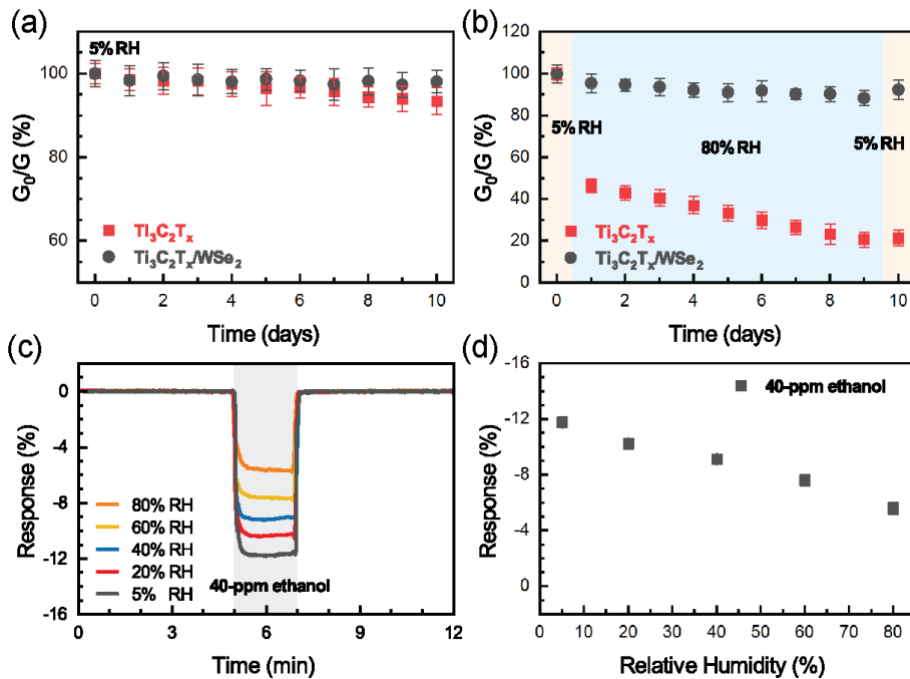


Fig. 6.7 Changes in electrical conductance of pristine $\text{Ti}_3\text{C}_2\text{T}_x$ and hybrid $\text{Ti}_3\text{C}_2\text{T}_x/\text{WSe}_2$ sensors under **(a)** 5% RH and **(b)** alternative RHs of 5 and 80% over 10 days. **(c)** Real-time responses of $\text{Ti}_3\text{C}_2\text{T}_x/\text{WSe}_2$ sensors toward 40 ppm ethanol under various RHs and **(d)** the sensing responses versus various RHs from 5 to 80%.⁸⁰

The stability of conductance and sensing response of inkjet-printed flexible $\text{Ti}_3\text{C}_2\text{T}_x/\text{WSe}_2$ gas sensor against mechanical bending was also evaluated. **Fig. 6.8(a)** shows a photograph of a flexible $\text{Ti}_3\text{C}_2\text{T}_x/\text{WSe}_2$ sensor. As depicted in **Fig. 6.8(b)**, the sensors reveal invariant conductance over 1000 cycles of bending at a radius of curvature of 5 mm; instead, sensing response toward 40 ppm ethanol increased slightly over bending cycles, which may be contributed to the creation of

bending-induced reactive sensing sites, such as microcracks and wrinkles by the strain force.¹¹¹ The retaining of the conductance level on the baseline of the sensor suggests that prolonged bending confirms good flexibility and high mechanical strength of the $\text{Ti}_3\text{C}_2\text{T}_x/\text{WSe}_2$ sensor.

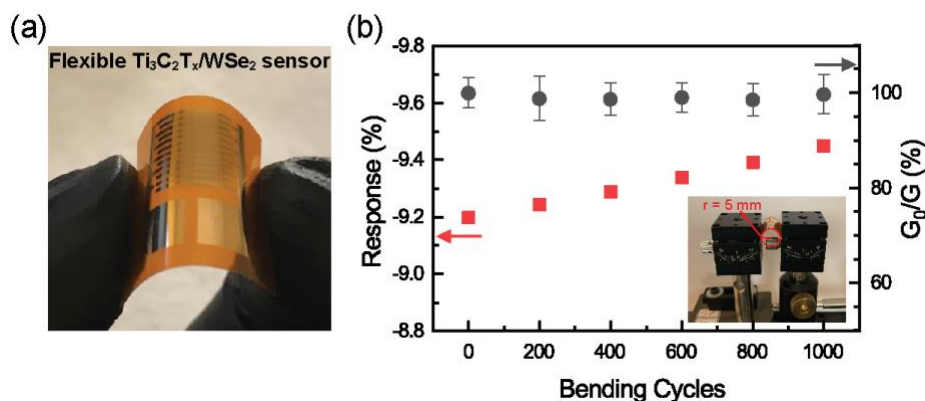


Fig. 6.8 (a) Photograph of a flexible $\text{Ti}_3\text{C}_2\text{T}_x/\text{WSe}_2$ nanohybrid sensor. (b) Bending test over 1000 cycles revealing stable electrical conductance and slightly increases in ethanol sensing response.⁸⁰

6.3.4 Sensitivity and Selectivity Performance

Fig. 6.9(a) presents the responses of pristine $\text{Ti}_3\text{C}_2\text{T}_x$ and hybrid $\text{Ti}_3\text{C}_2\text{T}_x/\text{WSe}_2$ sensors upon exposure to ethanol gas from 1 to 40 ppm. The $\text{Ti}_3\text{C}_2\text{T}_x$ sensor shows a positive but relatively small increase of resistance to ethanol, indicating that its charge carrier transport channel is always hindered when ethanol molecules are adsorbed. The positive response is owing to the metallic conductivity of $\text{Ti}_3\text{C}_2\text{T}_x$, where gas adsorption reduces the number of charge carriers, thereby increasing the channel resistance.¹²¹ The unrecoverable response of the $\text{Ti}_3\text{C}_2\text{T}_x$ sensor was observed by a slight drift of the baseline because of an incomplete gas desorption from $\text{Ti}_3\text{C}_2\text{T}_x$ caused by chemisorption of ethanol.³² By contrast, the $\text{Ti}_3\text{C}_2\text{T}_x/\text{WSe}_2$ sensor obviously displays negative variations of resistance to ethanol all through the concentrations tested (1 to 40 ppm), indicating that the $\text{Ti}_3\text{C}_2\text{T}_x/\text{WSe}_2$ heterostructured sensor is dominated by a different sensing mechanism compared to pristine $\text{Ti}_3\text{C}_2\text{T}_x$. **Fig. 6.9(b)** displays the responses of the $\text{Ti}_3\text{C}_2\text{T}_x$ and $\text{Ti}_3\text{C}_2\text{T}_x/\text{WSe}_2$ sensors as a function of ethanol concentrations. Over the testing concentrations between 1 to 40 ppm, the response of the $\text{Ti}_3\text{C}_2\text{T}_x$ sensor was insensitive to concentration variations but, after hybridization with WSe_2 , the $\text{Ti}_3\text{C}_2\text{T}_x/\text{WSe}_2$ sensor exhibited an approximately linear and strong variation in response. Here, the sensitivity of the sensors was defined as the slope (response/ppm), showing a significant increase of sensitivity from 0.02 ($\text{Ti}_3\text{C}_2\text{T}_x$) to 0.24 ($\text{Ti}_3\text{C}_2\text{T}_x/\text{WSe}_2$). The formation of $\text{Ti}_3\text{C}_2\text{T}_x/\text{WSe}_2$ heterojunctions not only

provide fast electron transport but also act as effective catalysts due to its appropriate chemical potential¹²², both thus contributing to the gas-sensing enhancement.

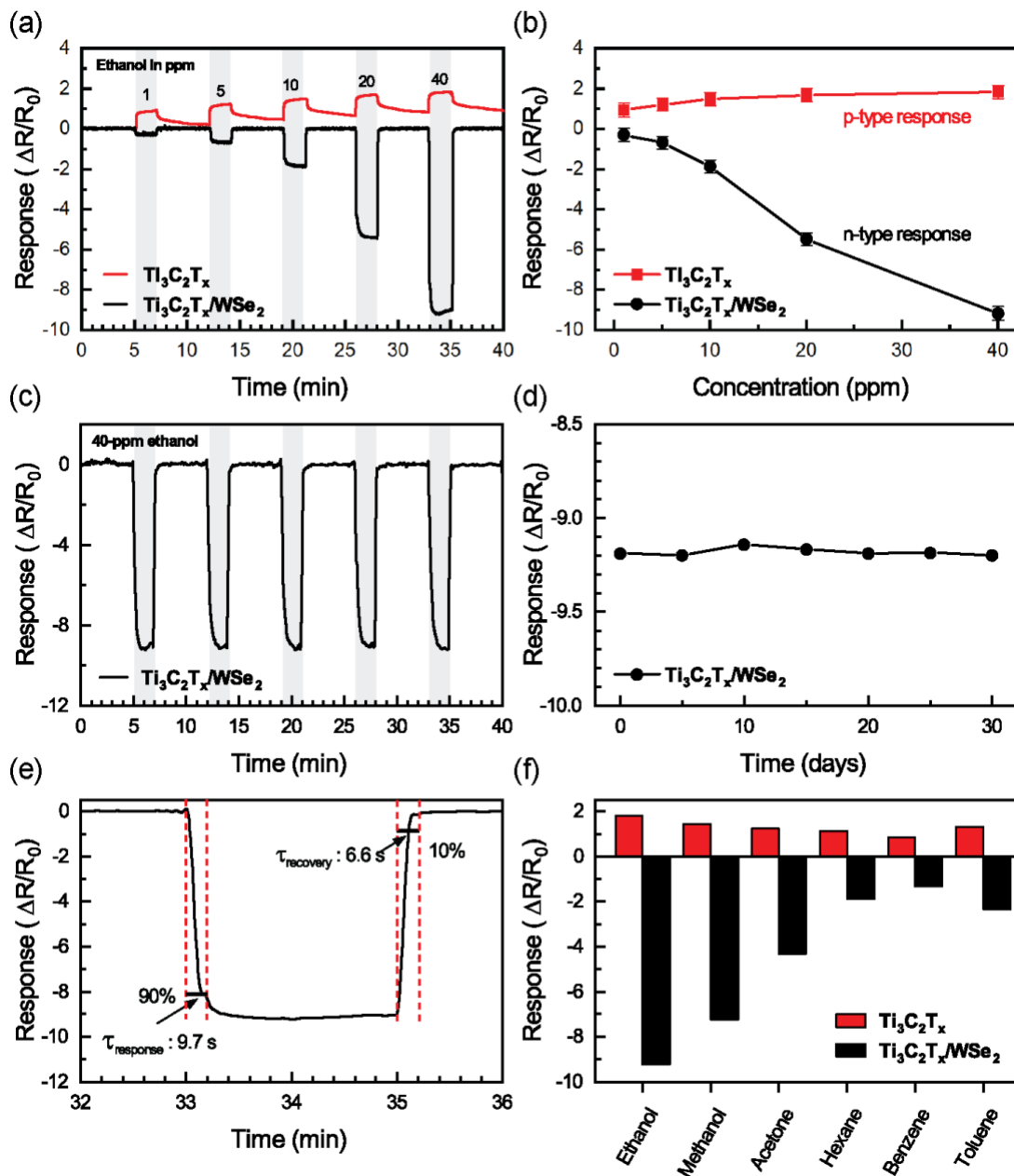


Fig. 6.9 (a) Real-time sensing response of $Ti_3C_2T_x$ and $Ti_3C_2T_x/WSe_2$ gas sensors upon exposure to ethanol from 1 to 40 ppm. (b) Gas response versus ethanol concentrations for $Ti_3C_2T_x$ and $Ti_3C_2T_x/WSe_2$ sensors. (c) Cycling responses and (d) long-term (one-month) stability of response of $Ti_3C_2T_x/WSe_2$ sensors toward 40 ppm of ethanol. (e) Response and recovery times of $Ti_3C_2T_x/WSe_2$ gas sensors. (f) Selectivity test of the $Ti_3C_2T_x$ and $Ti_3C_2T_x/WSe_2$ sensors toward various VOCs at 40 ppm.⁸⁰ All the experiments were performed at room temperature.

Fig. 6.9(c) shows the response of the $\text{Ti}_3\text{C}_2\text{T}_x/\text{WSe}_2$ sensor tested under 40 ppm of ethanol for five consecutive cycles, demonstrating its repeatable, fast gas response and recovery. The long-term stability of $\text{Ti}_3\text{C}_2\text{T}_x/\text{WSe}_2$ sensor was also tested under 40 ppm of ethanol at an interval of 30 days. As proven by **Fig. 6.9(d)**, the response remained at around -9.2% after a month of testing, indicating good stability of the $\text{Ti}_3\text{C}_2\text{T}_x/\text{WSe}_2$ sensors for practical applications.

The hybridization process might also be an effective strategy to overcome the oxidation of MXenes.^{114,123} For efficient operation, the sensor must recover to baseline resistance with short response and quick recovery. **Fig. 6.9(e)** indicates that the response time and recovery time of the $\text{Ti}_3\text{C}_2\text{T}_x/\text{WSe}_2$ sensor towards 40-ppm ethanol were 9.7 and 6.6 s, respectively, demonstrating ultrafast response and recovery properties even at room temperature. The heterojunction formation effectively accelerates the transport of electrons and serves as a catalyst lowering the activation energy of gas analytes.^{122,124}

To realize further the benefit of hybridizing $\text{Ti}_3\text{C}_2\text{T}_x$ with WSe_2 in the detection of various VOCs, the pristine $\text{Ti}_3\text{C}_2\text{T}_x$ and $\text{Ti}_3\text{C}_2\text{T}_x/\text{WSe}_2$ sensors were exposed to various oxygen-containing VOCs: ethanol, methanol, and acetone and carbon-based VOCs: hexane, benzene, and toluene, with concentration of 40 ppm, and the results are presented in **Fig. 6.9(f)**. Upon exposure to these gases, the $\text{Ti}_3\text{C}_2\text{T}_x$ sensor showed a positive, smaller response value, while the $\text{Ti}_3\text{C}_2\text{T}_x/\text{WSe}_2$ sensor exhibited a negative and much higher response value. In general, the interaction of carbon-based VOCs with sensing surface is minimal by their electron clouds inducing slightly dipole scattering, which results in relatively small resistance variations for both sensors. Both $\text{Ti}_3\text{C}_2\text{T}_x$ and $\text{Ti}_3\text{C}_2\text{T}_x/\text{WSe}_2$ sensors exhibit a slightly higher response to toluene and hexane, as compared to benzene, owing to an induction of dipole scattering by their methyl groups.³³ On the other hand, the response of the $\text{Ti}_3\text{C}_2\text{T}_x/\text{WSe}_2$ sensor to oxygen-containing molecules exhibited an enhancement of selectivity and sensitivity. The mechanism for the enhancement of detecting oxygen-containing VOCs will be discussed in the following section.

6.3.5 Sensing Mechanism

A sensing mechanism for the enhancement of detecting oxygen-based VOCs with $\text{Ti}_3\text{C}_2\text{T}_x/\text{WSe}_2$ nanohybrids is depicted in **Fig. 6.10(a)** and **(b)**. **Fig. 6.10(a)** reveals that the $\text{Ti}_3\text{C}_2\text{T}_x/\text{WSe}_2$ nanohybrids have a partially occupied band structure crossing the Fermi level, offering a good catalytic enhancement to sensing reactions because the highly conductive $\text{Ti}_3\text{C}_2\text{T}_x$

nanosheets readily supply a flow of electrons to WSe_2 .¹²² Therefore, in fresh air, the electrons are trapped by adsorbed oxygen species (O_2^- and O^-) owing to its electron deficient nature, thereby creating a depletion layer. Upon exposure to oxygen-based VOCs, such as ethanol (**Fig. 6.10(b)**), the adsorbed active oxygen species react with ethanol molecules subsequently forming volatile gases (CO_2 and H_2O) and releasing electrons back to the conduction band, thereby resulting in a reduction in thickness of the depletion layer and resistance of the sensor (n-type sensing behavior in $\text{Ti}_3\text{C}_2\text{T}_x/\text{WSe}_2$ channels). Notably, the oxygen species adsorbed onto $\text{Ti}_3\text{C}_2\text{T}_x/\text{WSe}_2$ nano hybrids are significantly increases, because of the numerous heterojunction interfaces formed, which in turn raise the electron content trapped. Upon exposure to ethanol, a large number of captured electrons release back to the $\text{Ti}_3\text{C}_2\text{T}_x/\text{WSe}_2$ channel and thus significantly improve the sensing response and selectivity in detection of oxygen-containing VOCs.

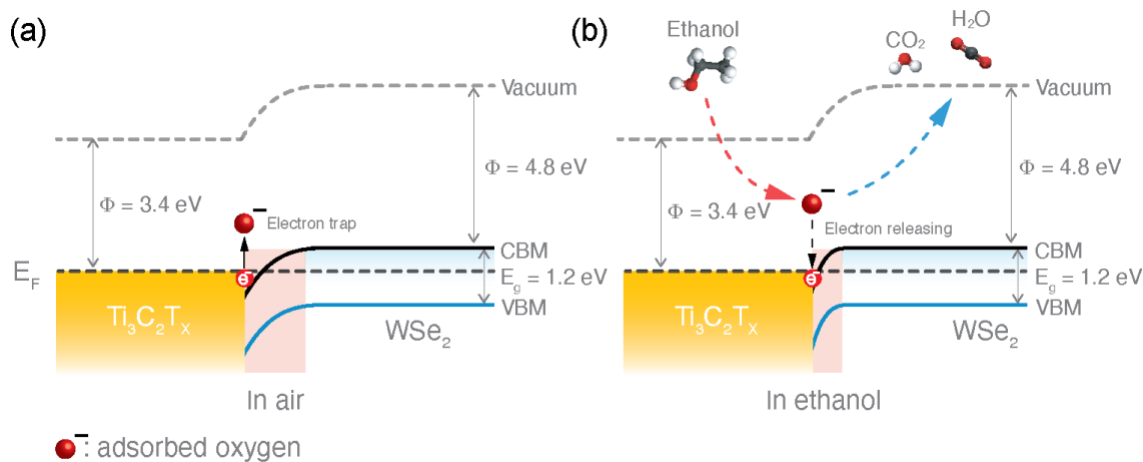


Fig. 6.10 Enhanced sensing mechanism of $\text{Ti}_3\text{C}_2\text{T}_x/\text{WSe}_2$ heterostructure. Energy-band diagram of the $\text{Ti}_3\text{C}_2\text{T}_x/\text{WSe}_2$ in (a) air and (b) ethanol, showing the variation of the depletion layer with an interaction between adsorbed oxygen species and ethanol molecules.⁸⁰

7. FLEXIBLE SILANE-FUNCTIONALIZED $\text{Ti}_3\text{C}_2\text{T}_x$ CONDUCTOMETRIC GAS SENSORS

7.1 Sensor Fabrication

First, the $\text{Ti}_3\text{C}_2\text{T}_x$ nanosheets were fabricated by selective etching the Al layers in the Ti_3AlC_2 powders with LiF/HCl aqueous solution. The surface of $\text{Ti}_3\text{C}_2\text{T}_x$ nanosheets possess an abundance of hydroxyl ($-\text{OH}$) and oxygen ($-\text{O}$) terminal groups, acting as covalent linking sites for functionalization of a self-assembled monolayer (SAM). The $\text{Ti}_3\text{C}_2\text{T}_x$ MXene nanosheets were functionalized by (3-chloropropyl)trimethoxysilane (CPTMS), denoted $\text{Ti}_3\text{C}_2\text{T}_x\text{-Cl}$; others were functionalized by 1H, 1H, 2H, 2H-perfluorooctyltriethoxysilane (FOTS), labeled $\text{Ti}_3\text{C}_2\text{T}_x\text{-F}$. **Fig. 7.1** depicts the preparation process of silane-modified $\text{Ti}_3\text{C}_2\text{T}_x$ nanosheets, using $\text{Ti}_3\text{C}_2\text{T}_x\text{-F}$ as an example.

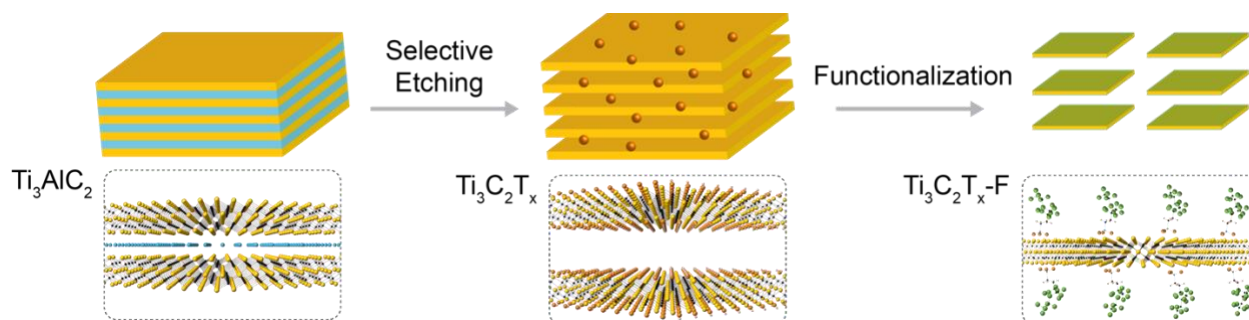


Fig. 7.1 Schematic process flows for the preparation of silane-modified $\text{Ti}_3\text{C}_2\text{T}_x$.⁸¹

7.2 Materials Characterization

The XRD patterns in **Fig. 7.2(a)** reveal that etching of Ti_3AlC_2 powder results in a downshift of the (002) peak from 9.5° to 7.0° , and a greatly weakened (104) peak at 38.9° , thus verifying the successful formation of $\text{Ti}_3\text{C}_2\text{T}_x$ nanosheets.⁷⁶ After silanization (SAM functionalization), the (002) peak of $\text{Ti}_3\text{C}_2\text{T}_x$ downshifts from 7.0° to 6.6° ($\text{Ti}_3\text{C}_2\text{T}_x\text{-Cl}$) and 5.5° ($\text{Ti}_3\text{C}_2\text{T}_x\text{-F}$), indicating that the increase of interplanar distance from 12.5 to 13.4 and 16.0 \AA , respectively. The magnitude of the interlayer spacing expansion is smaller than the molecular sizes of FOTS and CPTMS. This could be due to their molecular flexibility allowing them to ‘squeeze’ into narrow spaces, as also previously observed by other groups.¹²⁵⁻¹²⁷ The SEM images of Ti_3AlC_2 and as-etched $\text{Ti}_3\text{C}_2\text{T}_x$,

displayed in **Fig. 7.2(b)** and **(c)**, respectively, clearly show the transition from a bulk Ti_3AlC_2 to $\text{Ti}_3\text{C}_2\text{T}_x$ nanosheets.

The SEM image of spray-coated $\text{Ti}_3\text{C}_2\text{T}_x\text{-F}$ film in **Fig. 7.2(d)** exhibits a porous 3D architecture consisting of wrinkled and crumpled nanosheets, which promotes gas diffusion and enhances the sensing performance as observed later. HAADF-STEM image and EDS mappings of the $\text{Ti}_3\text{C}_2\text{T}_x\text{-F}$ present a uniform distribution of Ti, C, and F elements within the nanosheet (**Fig. 7.2(e)**), confirming a homogeneous functionalization of $\text{Ti}_3\text{C}_2\text{T}_x$ with FOTS molecules. The EDS spectrum in **Fig. 7.3**, obtained from $\text{Ti}_3\text{C}_2\text{T}_x\text{-F}$ nanosheets, further confirms a successful functionalization of $\text{Ti}_3\text{C}_2\text{T}_x$ surface with FOTS as a strong silicon peak at 1.73 eV is identified, which is exclusively found in the FOTS silane monolayer.¹²⁸

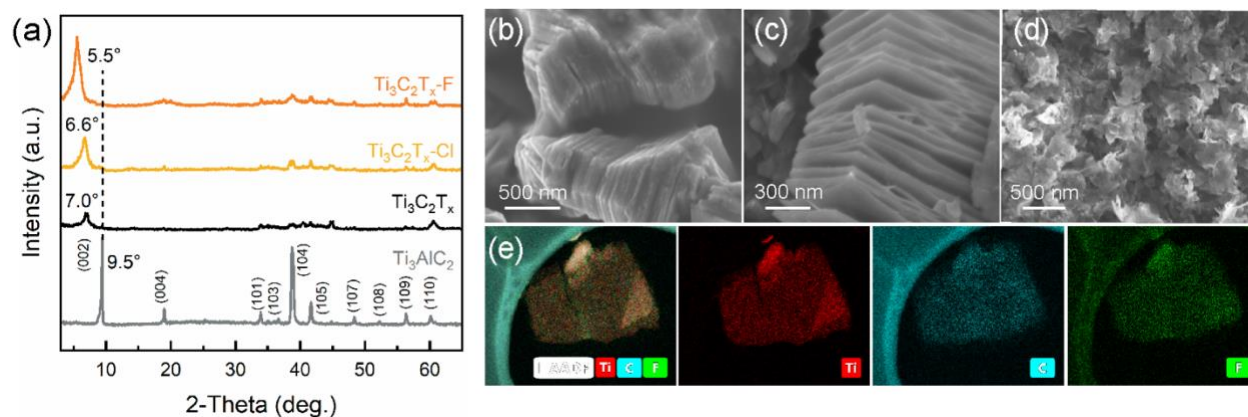


Fig. 7.2 (a) XRD patterns of Ti_3AlC_2 , $\text{Ti}_3\text{C}_2\text{T}_x$, $\text{Ti}_3\text{C}_2\text{T}_x\text{-Cl}$, and $\text{Ti}_3\text{C}_2\text{T}_x\text{-F}$ samples. SEM images of (b) Ti_3AlC_2 , (c) as-etched $\text{Ti}_3\text{C}_2\text{T}_x$, and (d) spray-coated $\text{Ti}_3\text{C}_2\text{T}_x\text{-F}$ film. (e) HAADF-STEM image and corresponding element mappings of $\text{Ti}_3\text{C}_2\text{T}_x\text{-F}$ nanosheets showing a uniform distribution of Ti, C, and F.⁸¹

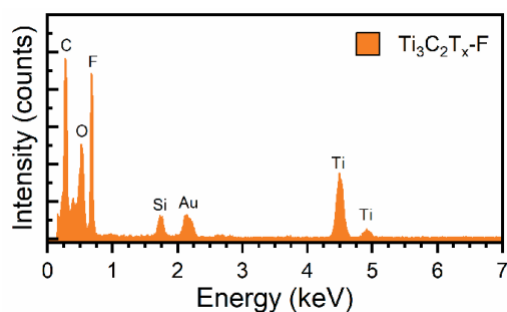


Fig. 7.3 EDS spectrum of FOTS-functionalized $\text{Ti}_3\text{C}_2\text{T}_x$ with a silicon characteristic peak of FOTS at 1.73 keV.

The specific surface areas of Ti_3AlC_2 , $\text{Ti}_3\text{C}_2\text{T}_x$, $\text{Ti}_3\text{C}_2\text{T}_x\text{-Cl}$ and $\text{Ti}_3\text{C}_2\text{T}_x\text{-F}$ samples were analyzed by the Brunauer-Emmett-Teller (BET) method under nitrogen adsorption/desorption at 77 K. The nitrogen adsorption/desorption isotherms for Ti_3AlC_2 , $\text{Ti}_3\text{C}_2\text{T}_x$, $\text{Ti}_3\text{C}_2\text{T}_x\text{-Cl}$ and $\text{Ti}_3\text{C}_2\text{T}_x\text{-F}$ samples (**Fig. 7.4**) all exhibited a Type 3 hysteresis loop (IUPAC classification) at high relative pressure that was typically related to adsorption within aggregates of plate-like particles.¹²⁹ The BET specific surface areas for Ti_3AlC_2 and $\text{Ti}_3\text{C}_2\text{T}_x$ particulates were 2.6 and 10.9 m^2/g , respectively; the significant increase in specific surface area also confirmed the successful exfoliation of $\text{Ti}_3\text{C}_2\text{T}_x$ upon the selective etching process. Furthermore, while $\text{Ti}_3\text{C}_2\text{T}_x\text{-Cl}$ exhibited an elevated specific surface area of 20.4 m^2/g , the specific surface area of $\text{Ti}_3\text{C}_2\text{T}_x\text{-F}$ was even much higher 32.9 m^2/g . The increase in specific surface areas observed here is attributed to the increase of the interplanar distance by the intercalating SAM molecules (as confirmed from the XRD analysis in **Fig. 7.2**). Notably, a larger specific surface area not only contributes more active sites for gas adsorption but also offers faster gas diffusion that enhances gas-sensing performance. The sensing topics will be presented in Section 7.3.3.

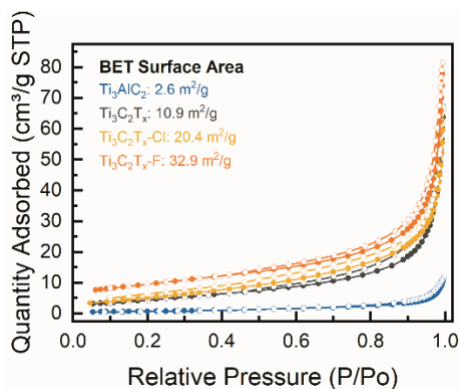


Fig. 7.4 Nitrogen adsorption/desorption isotherms for Ti_3AlC_2 , $\text{Ti}_3\text{C}_2\text{T}_x$, $\text{Ti}_3\text{C}_2\text{T}_x\text{-Cl}$ and $\text{Ti}_3\text{C}_2\text{T}_x\text{-F}$ samples.⁸¹

As evidenced from measurements of water contact angle in **Fig. 7.5(a)**, the SAM modifications significantly altered the wettability of $\text{Ti}_3\text{C}_2\text{T}_x$ nanosheets. The pristine $\text{Ti}_3\text{C}_2\text{T}_x$ film had a hydrophilic surface with a water contact angle (θ) of 33° stemming from its oxygen-based ($-\text{OH}$ and $-\text{O}$) terminal groups,¹³⁰ whereas the chlorine-containing ($\text{Ti}_3\text{C}_2\text{T}_x\text{-Cl}$) and fluorine-containing ($\text{Ti}_3\text{C}_2\text{T}_x\text{-F}$) films presented much higher contact angles of 96° and 156° , respectively. Notably, the pristine $\text{Ti}_3\text{C}_2\text{T}_x$ surface only functionalized with FOTS-SAM exhibited superhydrophobicity (defined as $\theta > 150^\circ$), indicating that FOTS molecules play a critical role in

lowering surface energy due to their firm interaction with surface hydroxyl groups of $\text{Ti}_3\text{C}_2\text{T}_x$. The evolution of contact angles of $\text{Ti}_3\text{C}_2\text{T}_x$ with silanization times of FOTS molecules was further monitored to ensure their full assembling onto $\text{Ti}_3\text{C}_2\text{T}_x$. As shown in **Fig. 7.5****Error! Reference source not found.**(b), the contact angle sharply increased with silanization time and levelled off after 6 h of reaction, indicating the presence of a fully ordered FOTS molecular layer on the surface of the nanosheets. **Fig. 7.5**(c) displays the results of zeta-potential measurements, confirming the formation of the SAM on the $\text{Ti}_3\text{C}_2\text{T}_x$ surface. The as-prepared $\text{Ti}_3\text{C}_2\text{T}_x$ nanosheets exhibited a negatively charged surface of -28.7 mV, which is attributed to the anionic nature of $-\text{OH}$ and $-\text{O}$ species terminated on $\text{Ti}_3\text{C}_2\text{T}_x$ surfaces.¹³¹ After surface functionalization, the $\text{Ti}_3\text{C}_2\text{T}_x\text{-Cl}$ and $\text{Ti}_3\text{C}_2\text{T}_x\text{-F}$ nanosheets had more negative charged surface of -35.8 and -50.1 mV, respectively, owing to the presence of an SAM with grafting end-chlorine (CPTMS) and end-fluorine (FOTS) on the $\text{Ti}_3\text{C}_2\text{T}_x$ surface.¹³²

The surface functionalization of $\text{Ti}_3\text{C}_2\text{T}_x$ with superhydrophobic and highly negatively charged FOTS-SAM could be an effective strategy to mitigate the oxidation tendency of $\text{Ti}_3\text{C}_2\text{T}_x$ by forming a protection layer. This will be discussed later.

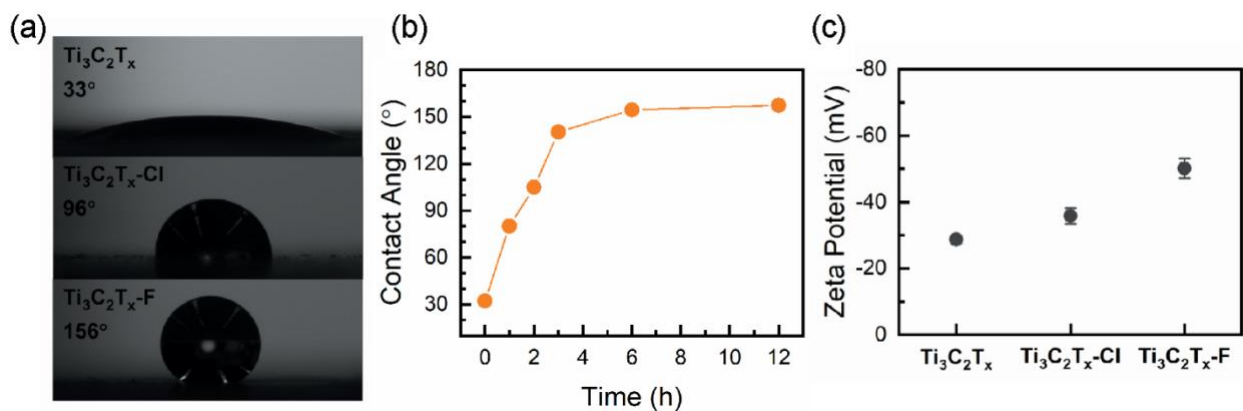


Fig. 7.5 (a) Water contact angle images of $\text{Ti}_3\text{C}_2\text{T}_x$, $\text{Ti}_3\text{C}_2\text{T}_x\text{-Cl}$, and $\text{Ti}_3\text{C}_2\text{T}_x\text{-F}$ films. (b) Evolution of contact angles of $\text{Ti}_3\text{C}_2\text{T}_x\text{-F}$ versus reaction times. (c) Zeta potential plots of $\text{Ti}_3\text{C}_2\text{T}_x$, $\text{Ti}_3\text{C}_2\text{T}_x\text{-Cl}$, and $\text{Ti}_3\text{C}_2\text{T}_x\text{-F}$ samples.⁸¹

The formation of an SAM is conventionally performed in a wet-chemical solution through hydrolysis of their molecule units.^{127,133} The schematics in **Fig. 7.6** illustrate that the hydrolysis reaction of FOTS transforms the $\text{Si}-\text{OCH}_2\text{CH}_3$ groups into $\text{Si}-\text{OH}$ groups with $\text{CH}_3\text{CH}_2\text{OH}$ being released as a reaction side product. Hydrogen bonds between the silanol groups of FOTS and $-\text{OH}$

surface termination groups of $\text{Ti}_3\text{C}_2\text{T}_x$ are then formed, followed by the formation of Si–O covalent bonds between $\text{Ti}_3\text{C}_2\text{T}_x$ and hydrolyzed FOTS.

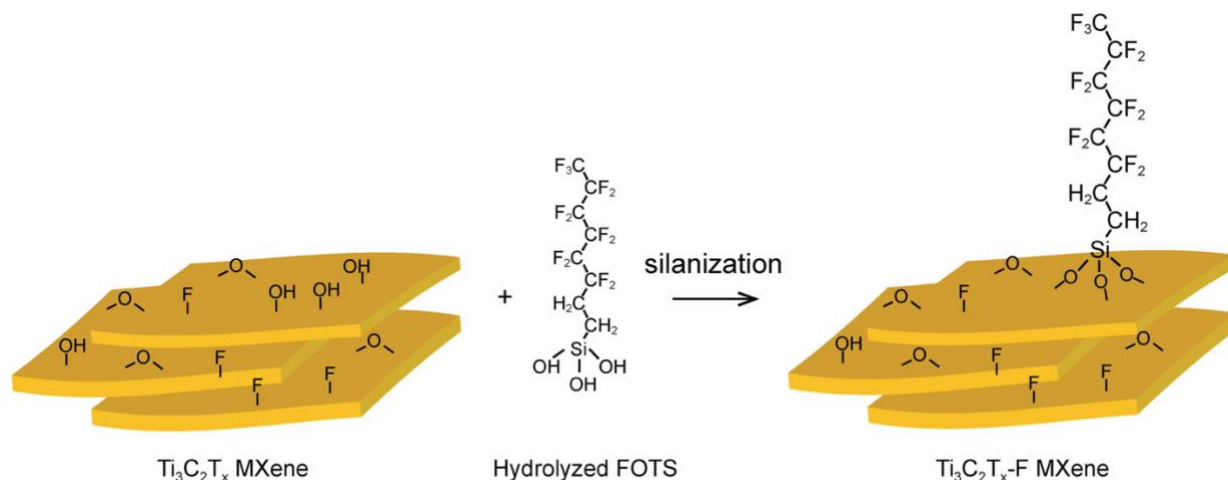


Fig. 7.6 Schematic illustration of surface functionalization of $\text{Ti}_3\text{C}_2\text{T}_x$ MXene with FOTS.⁸¹

The survey spectra of pristine $\text{Ti}_3\text{C}_2\text{T}_x$ and $\text{Ti}_3\text{C}_2\text{T}_x\text{-F}$ (**Fig. 7.7**) revealed that both $\text{Ti}_3\text{C}_2\text{T}_x$ and $\text{Ti}_3\text{C}_2\text{T}_x\text{-F}$ had a significant number of fluorine and oxygen-containing groups; however, the F/Ti atomic ratio of $\text{Ti}_3\text{C}_2\text{T}_x\text{-F}$ (4.92) is significantly larger than that of $\text{Ti}_3\text{C}_2\text{T}_x$ (2.21), suggesting that the $\text{Ti}_3\text{C}_2\text{T}_x\text{-F}$ has more fluorine terminal groups than pristine $\text{Ti}_3\text{C}_2\text{T}_x$.

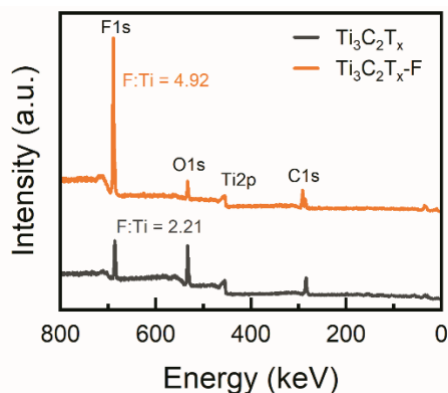


Fig. 7.7 XPS survey spectra of pristine $\text{Ti}_3\text{C}_2\text{T}_x$ (bottom) and FOTS-functionalized $\text{Ti}_3\text{C}_2\text{T}_x$ (top).⁸¹

High resolution XPS spectra of $\text{Ti}_3\text{C}_2\text{T}_x\text{-F}$ were also acquired, as shown in **Fig. 7.8**. The Ti 2p spectrum in **Fig. 7.8(a)** was fitted with a fixed area ratio of 2:1 and a doublet separation of 5.7 eV comprising four doublets of Ti $2p_{3/2}$ and Ti $2p_{1/2}$.¹³⁴ The binding energy of Ti $2p_{3/2}$ for Ti–C, Ti^{2+} , Ti^{3+} , and Ti–O are 454.5, 455.4, 457.6 and 458.7 eV, respectively, in agreement with previous

XPS studies.¹¹³⁻¹¹⁵ The signals of anatase titania appearing in the XPS spectrum are due to partial oxidation of $\text{Ti}_3\text{C}_2\text{T}_x$ MXenes during the synthesis process.¹³⁵ The C 1s spectrum in **Fig. 7.8(b)** was deconvoluted into two groups of peaks: (1) the peaks centered at 281.6, 284.7, 285.9, and 288.2 eV were identified as C–Ti– T_x , C–C, CH_x/CO and COO, respectively;¹¹³ (2) the peaks centered at 291.0 and 293.2 eV were attributed to $-\text{CF}_2$ and $-\text{CF}_3$, respectively.¹³⁶ Calculations of the fitted peak areas revealed that the ratio of $-\text{CF}_2$ to $-\text{CF}_3$ groups was about 4.8, reasonably close to a $-\text{CF}_2/-\text{CF}_3$ ratio of 5 for the theoretical molecular structure of FOTS;¹³⁷ the calculated results indicated the formation of an intact FOTS layer on $\text{Ti}_3\text{C}_2\text{T}_x$ nanosheets. The presence of an intense Si–O peak centered at 532.9 eV for the O 1s spectrum in **Fig. 7.8(c)** suggested that the surface hydroxyl groups in $\text{Ti}_3\text{C}_2\text{T}_x$ interact with the polar $\text{Si}(\text{OH})_3$ groups in FOTS molecules, leading to the formation of covalent bonds.¹³⁸ The F 1s spectrum in **Fig. 7.8(d)**, the dominant peak located at 687.9 eV was associated with the C–F species from FOTS,¹³⁹ whereas the peak at a reduced binding energy of 685.2 eV was given by the C–Ti– F_x from $\text{Ti}_3\text{C}_2\text{T}_x$ surface groups.¹¹³ This finding further confirmed the successful functionalization of $\text{Ti}_3\text{C}_2\text{T}_x$ with FOTS molecules.

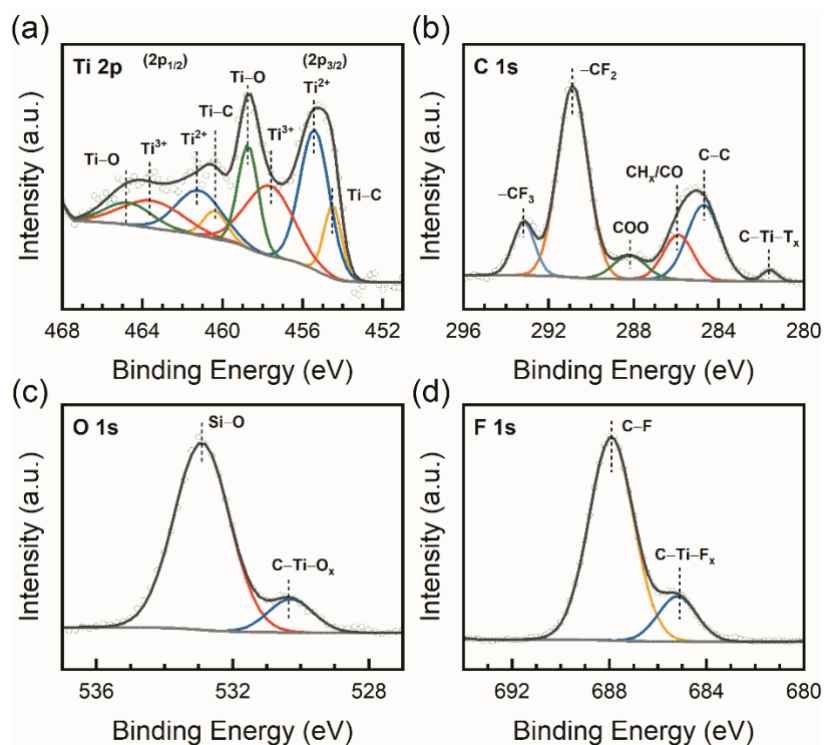


Fig. 7.8 XPS spectra of (a) Ti 2p, (b) C 1s, (c) O 1s, and (d) F 1s revealing chemical compositions and bonding characteristics of the FOTS-functionalized $\text{Ti}_3\text{C}_2\text{T}_x$ nanosheets.⁸¹

To serve as functional coatings for practical applications, MXenes have to be highly stable in terms of maintaining their functionalities upon exposure to realistic environments, such as hazardous substances or humid atmosphere, which could cause a serious degradation of MXene materials.^{117,118} The water contact angle measurements were conducted after immersing $\text{Ti}_3\text{C}_2\text{T}_x$ -F films to various hazardous liquids, including hydrochloric acid (HCl), ammonia hydroxide (NH_3OH), and deionized water, with pH values of 1.1, 11.3, and 6.8 respectively. The associated plots depicted in **Fig. 7.9(a)** can evaluate the effectiveness of the FOTS-SAM as a protection layer. The $\text{Ti}_3\text{C}_2\text{T}_x$ -F films maintained a contact angles over 150° even after exposure to strong acid/base solutions and water for 20 s, indicating that FOTS functionalization indeed results in the formation of an effective protection layer on $\text{Ti}_3\text{C}_2\text{T}_x$ surface. Moreover, the $\text{Ti}_3\text{C}_2\text{T}_x$ -F films also maintained their superhydrophobicity ($> 150^\circ$) after storage in air for 2 months (**Fig. 7.9(b)**), showing an excellent long-term stability in real environment.

Furthermore, the $\text{Ti}_3\text{C}_2\text{T}_x$ and $\text{Ti}_3\text{C}_2\text{T}_x$ -F films were stored under 5 and 100% RH, and their electrical conductance were measured over a period of two weeks. According to **Fig. 7.9(c)**, under 5% of RH environment, the changes in electrical conductance were small for both $\text{Ti}_3\text{C}_2\text{T}_x$ and $\text{Ti}_3\text{C}_2\text{T}_x$ -F films, suggesting that both films are relatively stable in the dry environment. However, after storing in an extremely wet environment (100% of RH) for two weeks, the electrical conductance of the $\text{Ti}_3\text{C}_2\text{T}_x$ films dramatically decreased to 2.7% of the initial conductance. By contrast, the $\text{Ti}_3\text{C}_2\text{T}_x$ -F films remained 86.2% of the initial conductance and recovered to 92.5% in dry environment. This difference indicates that the FOTS protection layer effectively retards $\text{Ti}_3\text{C}_2\text{T}_x$ degradation under extremely humid atmosphere.

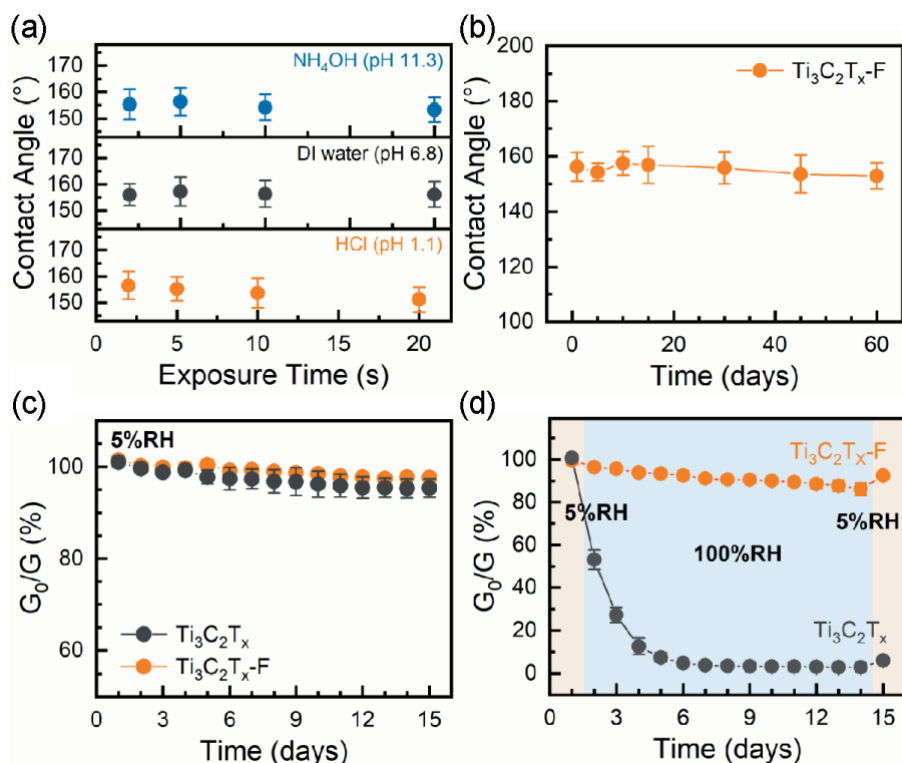


Fig. 7.9 (a) Water contact angle for $\text{Ti}_3\text{C}_2\text{T}_x\text{-F}$ films after exposure to NH_4OH (pH 11.3), DI water (pH 6.8), and HCl (pH 1.1) for 2, 5, 10, and 20 s, respectively. (b) Water contact angle variations of $\text{Ti}_3\text{C}_2\text{T}_x\text{-F}$ films for 2-month storage in air. Changes in electrical conductance of $\text{Ti}_3\text{C}_2\text{T}_x$ and $\text{Ti}_3\text{C}_2\text{T}_x\text{-F}$ under (c) 5% RH and (d) alternative RHs of 5 and 100% over a period two weeks.⁸¹

XPS was performed by recording the Ti XPS spectra and the changes of their Ti peaks for pristine $\text{Ti}_3\text{C}_2\text{T}_x$ (**Fig. 7.10**[Error! Reference source not found.](#)(a-c)) and $\text{Ti}_3\text{C}_2\text{T}_x\text{-F}$ (**Fig. 7.10**[Error! Reference source not found.](#)(d-f)) after a 100% HR treatment for two weeks. The $\text{Ti}_3\text{C}_2\text{T}_x$ and $\text{Ti}_3\text{C}_2\text{T}_x\text{-F}$ had similar Ti chemical species. However, the $\text{Ti}_3\text{C}_2\text{T}_x$ was unstable and fully oxidized to anatase titania after the prolonged humid treatment. By contrast, there was no prominent difference in the XPS spectra of the $\text{Ti}_3\text{C}_2\text{T}_x\text{-F}$ after the humid treatment, and the proportions of the various Ti species maintained in the same range as before treatment. These results indicate that $\text{Ti}_3\text{C}_2\text{T}_x$ indeed is prone to oxidation in moisture environments, but FOTS functionalized (superhydrophobic) $\text{Ti}_3\text{C}_2\text{T}_x$ exhibits a significantly improved environmental stability, offering an approach to overcoming the notorious oxidation tendency and structural instability, as well as undurable gas sensing properties, of MXenes.

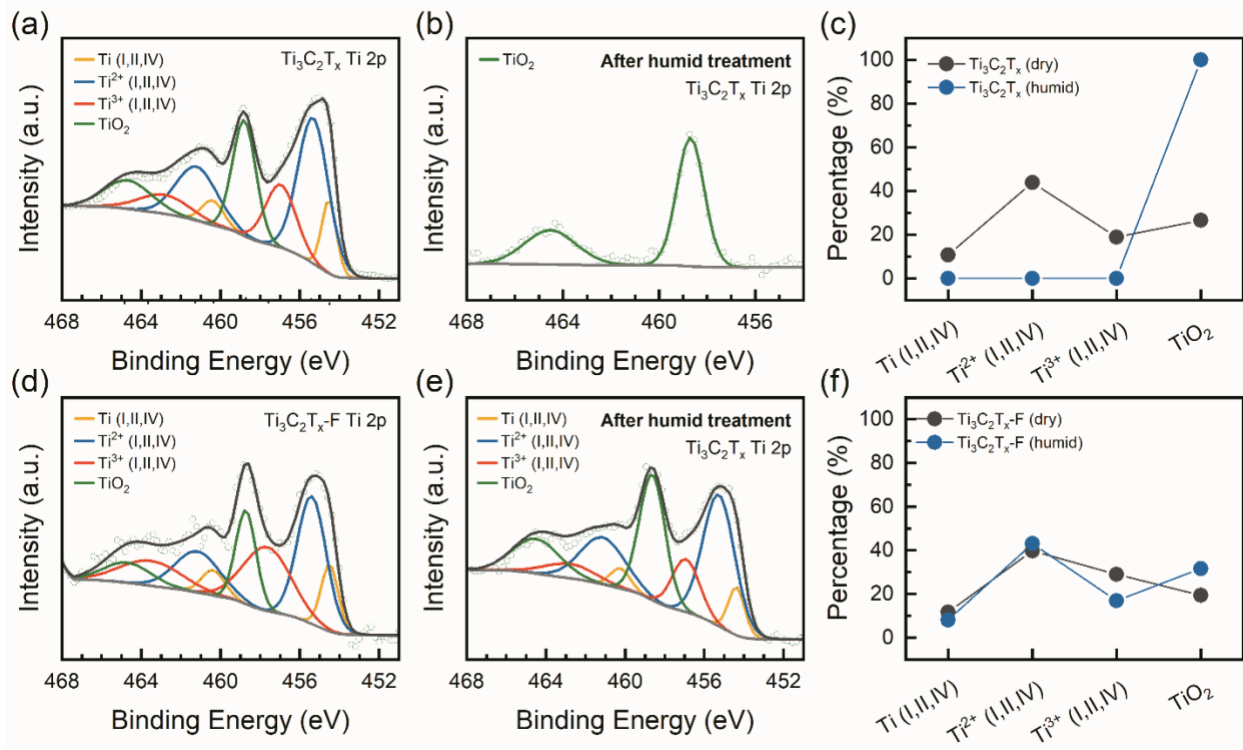


Fig. 7.10 Ti 2p XPS spectra showing the alternation of Ti chemical species contained in pristine (a) and (b) humidity treated $\text{Ti}_3\text{C}_2\text{T}_x$ films, along with the (c) plots showing proportion changes of the various Ti species derived from integrated peak areas; (d)-(f) revealing the corresponding results of $\text{Ti}_3\text{C}_2\text{T}_x\text{-F}$.⁸¹

7.3 The Performance of 2D $\text{Ti}_3\text{C}_2\text{T}_x$ -based Sensor Towards VOCs

7.3.1 Film Thickness Effect

The film thickness is a key factor affecting sensing performance.⁷ As presented later in the following sections, $\text{Ti}_3\text{C}_2\text{T}_x\text{-F}$ films have the best VOC-sensing performance. Here, we thus evaluated the gas-sensing response of the $\text{Ti}_3\text{C}_2\text{T}_x\text{-F}$ films with various thicknesses of 50, 100, and 200 nm toward the detection of 30-ppm acetone and ethanol (**Fig. 7.11**). The response of the $\text{Ti}_3\text{C}_2\text{T}_x\text{-F}$ sensors to both VOCs decreased dramatically with increasing film thickness. This is because an increase in film thickness lowers the surface-to-volume ratios of $\text{Ti}_3\text{C}_2\text{T}_x\text{-F}$ channel, subsequently hindering gas uptake and transport within the film.

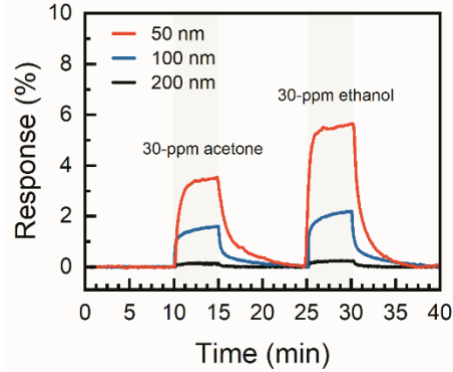


Fig. 7.11 Thickness-dependent responses of 50, 100, and 200-nm-thick $\text{Ti}_3\text{C}_2\text{T}_x\text{-F}$ films toward 30 ppm of acetone and ethanol.⁸¹

7.3.2 Signal-to-Noise Ratio

One of the advantages of $\text{Ti}_3\text{C}_2\text{T}_x$ MXene gas sensor is its high signal-to-noise ratio. We thus evaluated the effect of FOTS and CPTMS functionalization on $\text{Ti}_3\text{C}_2\text{T}_x$'s based sensor noise levels by measuring the average response fluctuation during air introduction. The noise levels, as calculated from **Fig. 7.12**, were approximately 0.05%, 0.1%, and 0.1% for $\text{Ti}_3\text{C}_2\text{T}_x$, $\text{Ti}_3\text{C}_2\text{T}_x\text{-Cl}$, and $\text{Ti}_3\text{C}_2\text{T}_x\text{-F}$ sensors, respectively. The results indicated that the SAM functionalization only caused a slight increase in noise levels.

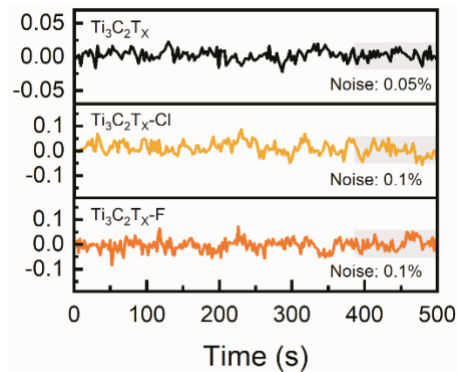


Fig. 7.12 Electrical noise levels of $\text{Ti}_3\text{C}_2\text{T}_x$, $\text{Ti}_3\text{C}_2\text{T}_x\text{-Cl}$, and $\text{Ti}_3\text{C}_2\text{T}_x\text{-F}$ sensors during air exposure.⁸¹

After FOTS (or CPTMS) functionalization, the $\text{Ti}_3\text{C}_2\text{T}_x$ based sensors showed no significant variation in baseline resistance levels (**Table 7.1**), which is consistent with previous studies for other silane-functionalized materials.¹⁴⁰ In contrast to other 2D materials (*e.g.*, MoS_2 and WSe_2),⁷ the Ti_3C_2 core materials have high electrical conductivity and extremely low noise levels and thus

these materials are an attractive choice for the development of high-performance electrochemical sensing devices.

Table 7.1 Average baseline resistances of $\text{Ti}_3\text{C}_2\text{T}_x$, $\text{Ti}_3\text{C}_2\text{T}_x\text{-Cl}$, and $\text{Ti}_3\text{C}_2\text{T}_x\text{-F}$ films measured in the gas sensing chamber at room temperature under air flow.⁸¹

Materials	Average baseline resistance
$\text{Ti}_3\text{C}_2\text{T}_x$	0.183 k \square
$\text{Ti}_3\text{C}_2\text{T}_x\text{-Cl}$	0.327 k \square
$\text{Ti}_3\text{C}_2\text{T}_x\text{-F}$	0.354 k \square

7.3.3 Sensitivity and Selectivity Performance

As presented in **Fig. 7.13(a)**, the $\text{Ti}_3\text{C}_2\text{T}_x$, $\text{Ti}_3\text{C}_2\text{T}_x\text{-Cl}$, and $\text{Ti}_3\text{C}_2\text{T}_x\text{-F}$ sensors were first examined by comparing their response curves toward the detection of ethanol with consecutive variations of concentrations from 5 to 120 ppm at room temperature. All the sensing films had the thickness of 50 nm, and triplicate sensing measurements were performed. **Fig. 7.13(b)** shows the response versus concentration of ethanol for $\text{Ti}_3\text{C}_2\text{T}_x$, $\text{Ti}_3\text{C}_2\text{T}_x\text{-Cl}$, and $\text{Ti}_3\text{C}_2\text{T}_x\text{-F}$ sensors. All the sensors exhibited a standard deviation ($n=3$) of less than 5% of average responses, indicating very good reproducibility of sensing response. Such small deviations suggest that the spray-coating method used here indeed offers high repeatability of sensor fabrication, thus giving low device-to-device variations. Among these sensors, the $\text{Ti}_3\text{C}_2\text{T}_x\text{-F}$ sensor yields the highest responses over the wide range of concentrations (5–120 ppm). For example, the response of $\text{Ti}_3\text{C}_2\text{T}_x\text{-F}$ sensor is 14% toward 120 ppm of ethanol, whereas the responses of $\text{Ti}_3\text{C}_2\text{T}_x$ and $\text{Ti}_3\text{C}_2\text{T}_x\text{-Cl}$ sensors are 6.6 and 10.1%, respectively. Moreover, the gas responses of these sensors are almost linear to ethanol ($R^2 > 0.98$), which is important in terms of a wide detection range and low detection limit for practical sensing applications.

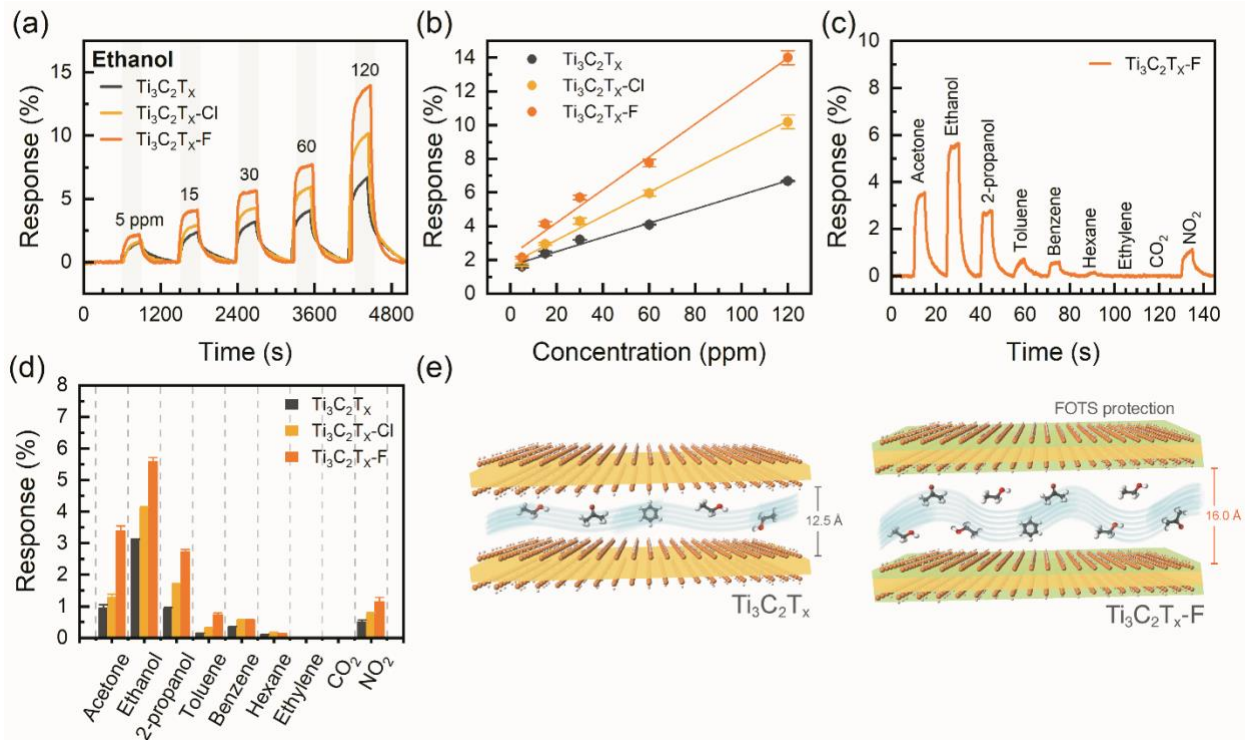


Fig. 7.13 (a) Real-time response curves of $Ti_3C_2T_x$, $Ti_3C_2T_x-Cl$, and $Ti_3C_2T_x-F$ sensors toward ethanol from 5 to 120 ppm and (b) the response as a function of ethanol. (c) Gas response of $Ti_3C_2T_x-F$ sensors upon exposure to 30 ppm of acetone, ethanol, 2-propanol, toluene, benzene, hexane, ethylene, carbon dioxide, and nitrogen dioxide. (d) Maximal response variations toward various gases at room temperature. (e) Schematics of $Ti_3C_2T_x$ and $Ti_3C_2T_x-F$ films upon exposure to VOCs.⁸¹

Fig. 7.13(c) shows that the response changes of the $Ti_3C_2T_x-F$ sensor toward 30 ppm of acetone (CH_3COCH_3), ethanol (C_2H_5OH), 2-propanol (C_3H_8O), toluene (C_7H_8), hexane (C_6H_{14}), ethylene (C_2H_4), carbon dioxide (CO_2), and nitrogen dioxide (NO_2) at room temperature. The corresponding maximal response changes for the $Ti_3C_2T_x$, $Ti_3C_2T_x-Cl$, and $Ti_3C_2T_x-F$ sensors toward these gases are summarized in **Fig. 7.13(d)**. The $Ti_3C_2T_x-F$ sensor exhibits markedly higher sensitivity to the oxygen-containing VOCs (acetone, ethanol, and 2-propanol), as compared to the hydrocarbon-based VOCs (toluene, benzene, hexane, and ethylene). The $Ti_3C_2T_x-F$ sensor shows no response to nonpolar inorganic gases (*e.g.*, CO_2).

In general, the hydrocarbon-based molecules have minimal interaction with the sensing surface because the electron clouds of their methyl groups induce merely dipole scattering,³² resulting in a relatively small resistance change for sensing channels. The $Ti_3C_2T_x-F$ sensor shows much higher selectivity and sensitivity toward the oxygen-based molecules, as compared to other

gases examined. It has been reported that acetone, ethanol, and 2-propanol gases are electron-donating gases.^{30,55} Notably, $\text{Ti}_3\text{C}_2\text{T}_x$ is a metallic-based material and thus should not exhibit either *p*- or *n*-type sensing behavior, which is the mechanism used to explain the performance of the sensors using semiconducting working electrode materials. Instead, the sensing mechanisms at play for MXene-based sensors reported herein can be understood by comparing the sensing behavior of the $\text{Ti}_3\text{C}_2\text{T}_x\text{-F}$ based sensor toward strong oxidizing (electron-accepting) NO_2 and electron-donating VOCs (acetone, ethanol, *etc.*). This sensor shows comprehensive positive changes of resistance regardless of gas type, implying that the charge-carrier-transport channel is always impeded upon the adsorption of a gas molecule. Such behavior is distinctive from other 2D semiconducting electrode materials, where the resistance change depends on the electron-donating or accepting properties of gas molecules and the type (*p*- or *n*-type) of channel materials.^{31,141}

The comprehensive positive response of the MXene-based sensor is due to the metallic conductivity of $\text{Ti}_3\text{C}_2\text{T}_x$, where gas adsorption reduces the number of charge carriers, thereby increasing the channel resistance.^{7,80} The gas-sensing enhancement of $\text{Ti}_3\text{C}_2\text{T}_x\text{-F}$ is contributed to its significantly increased interlayer distance and surface area compared to pristine $\text{Ti}_3\text{C}_2\text{T}_x$ and $\text{Ti}_3\text{C}_2\text{T}_x\text{-Cl}$ (confirmed by XRD and BET analyses). **Fig. 7.13(e)** shows an increase of the interlayer distance of $\text{Ti}_3\text{C}_2\text{T}_x$ from 12.5 to 16.0 Å after FOTS functionalization, which facilitate gas diffusion within the layers and thus causing the gas-sensing enhancement.

7.3.4 Response, Recovery and Durability of Sensors

We also evaluated the response and recovery properties of $\text{Ti}_3\text{C}_2\text{T}_x$, $\text{Ti}_3\text{C}_2\text{T}_x\text{-Cl}$, and $\text{Ti}_3\text{C}_2\text{T}_x\text{-F}$ sensors, and a typical result for the $\text{Ti}_3\text{C}_2\text{T}_x\text{-F}$ sensor upon exposure to 5 ppm of ethanol is shown in **Fig. 7.14(a)**. The response and recovery times of the $\text{Ti}_3\text{C}_2\text{T}_x$, $\text{Ti}_3\text{C}_2\text{T}_x\text{-Cl}$, and $\text{Ti}_3\text{C}_2\text{T}_x\text{-F}$ sensors versus different concentrations of ethanol (5 to 120 ppm) are respectively presented in **Fig. 7.14(b)** and **(c)**, demonstrating that the response time decreases and the recovery time increases with increasing ethanol concentrations. The decrease in response time may be due to the fact that the large gas adsorption sites are available, and the increase in recovery time may be attributed to the chemisorbed ethanol and reaction products not immediately desorbed from the surface.^{90,141} Notably, using 120 ppm as an example, the response/recovery times of $\text{Ti}_3\text{C}_2\text{T}_x\text{-F}$ sensor are about 39/139 s, whereas the response/recovery times of $\text{Ti}_3\text{C}_2\text{T}_x$ and $\text{Ti}_3\text{C}_2\text{T}_x\text{-Cl}$ sensors are much slower, at around 150/407 s and 120/332 s, respectively. This significant enhancement is owing to the

increase of interlayer spacing and specific surface area of $\text{Ti}_3\text{C}_2\text{T}_x$ induced by the intercalation of FOTS molecules, which benefits the gas transport and uptake within the film.

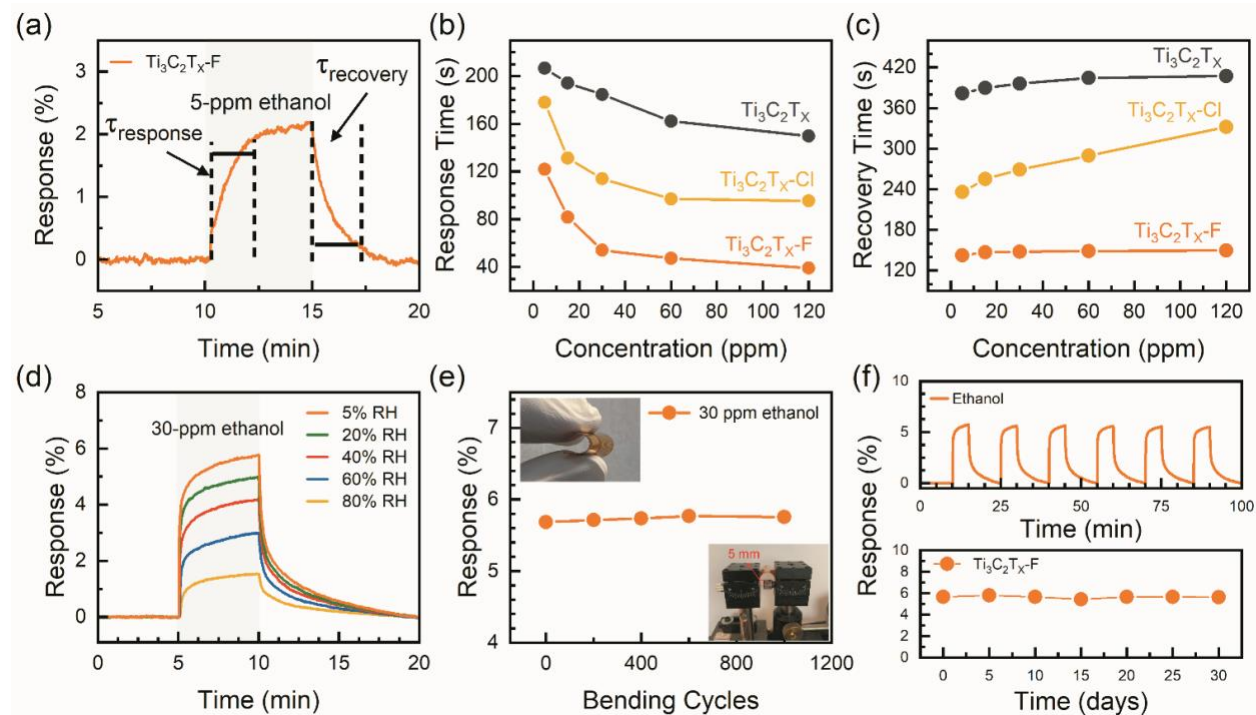


Fig. 7.14 (a) Response and recovery plot of $\text{Ti}_3\text{C}_2\text{T}_x\text{-F}$ toward 5 ppm of ethanol. (b) Response and (c) recovery times under different ethanol concentrations for the $\text{Ti}_3\text{C}_2\text{T}_x$, $\text{Ti}_3\text{C}_2\text{T}_x\text{-Cl}$, $\text{Ti}_3\text{C}_2\text{T}_x\text{-F}$ sensors. (d) Real-time response curves of the $\text{Ti}_3\text{C}_2\text{T}_x\text{-F}$ sensor toward 30 ppm of ethanol under different RH levels from 5 to 80%. (e) Sensing response of the $\text{Ti}_3\text{C}_2\text{T}_x\text{-F}$ sensor to 30 ppm of ethanol versus bending cycles. (f) Long-term stability over a month (bottom) and consecutive sensing cycles (top) of the $\text{Ti}_3\text{C}_2\text{T}_x\text{-F}$ sensor toward 30 ppm of ethanol.⁸¹

Fig. 7.14(d) shows the dynamic response of the $\text{Ti}_3\text{C}_2\text{T}_x\text{-F}$ sensor to 30 ppm of ethanol under various RH levels (5 to 80%). The response of the $\text{Ti}_3\text{C}_2\text{T}_x\text{-F}$ sensor decreased from 5.7% to 1.5% as the humidity increased from 5 to 80%, indicating that, although there is a humidity interference, the functionalized sensor still performs well in a high humidity environment up to 80%. The decrease of the sensor response is expected and is most likely due to partial occupancy of water molecules on active surface of sensing channel, which adversely affects sensing performance.¹⁴² As observed from **Fig. 7.14(e)**, the flexible $\text{Ti}_3\text{C}_2\text{T}_x\text{-F}$ sensor was subjected to cyclic bending tests with a bending radius of 5 mm, and their sensing performance toward 30 ppm of ethanol was evaluated. After 1,000 bending cycles, the sensor response was well maintained; this durability is

ascribed to the outstanding mechanical and flexibility properties of the 2D MXene, which result in reducing cracks and damage during the bending test.¹⁴³

The $\text{Ti}_3\text{C}_2\text{T}_x\text{-F}$ sensor was further tested under 30 ppm of ethanol over a period of 30 days, as shown in the bottom plot of **Fig. 7.14(f)**. The $\text{Ti}_3\text{C}_2\text{T}_x\text{-F}$ sensor revealed no significant response variations after 30 days of testing, suggesting its good long-term stability and durability for practical sensing application. The performance of the $\text{Ti}_3\text{C}_2\text{T}_x\text{-F}$ sensor under 30 ppm ethanol toward for six consecutive cycles was also tested and shown in the top plot of **Fig. 7.14(f)**, revealing the sensor's repeatable and stable sensing responses.

7.3.5 Sensing Mechanism for Silane-functionalized MXene

Density functional theory (DFT) simulations were performed to calculate the values of adsorption energy of ethanol and toluene molecules on $\text{Ti}_3\text{C}_2\text{T}_x$ and $\text{Ti}_3\text{C}_2\text{T}_x\text{-F}$. Error! Reference source not found.(a) displays the side and top views of the most stable molecular configuration for an ethanol molecule adsorbed on $\text{Ti}_3\text{C}_2\text{T}_x\text{-F}$ through DFT simulations. First, the ethanol adsorption induces a local structural deformation that causes the Ti–O bond length to increase from 2.26 to 2.57 Å, indicating a strong interaction of ethanol molecule with $\text{Ti}_3\text{C}_2\text{T}_x\text{-F}$. A similar structural deformation upon gas adsorption was also observed previously.¹⁴⁴ The oxygen atom adjacent to the adsorbed ethanol molecule is pulled outward from the layer owing to the attraction between the oxygen and the ethanol's hydrogen atom. **Fig. 7.15**Error! Reference source not found.(b) shows the minimum adsorption energies of the ethanol and toluene molecules for $\text{Ti}_3\text{C}_2\text{T}_x$ and $\text{Ti}_3\text{C}_2\text{T}_x\text{-F}$ calculated from DFT simulations, along with their corresponding sensor responses. The adsorption energies of ethanol are stronger than those of toluene for both $\text{Ti}_3\text{C}_2\text{T}_x$ and $\text{Ti}_3\text{C}_2\text{T}_x\text{-F}$, suggesting a strong interaction of ethanol with MXene-based sensors. Moreover, the adsorption energy of ethanol on $\text{Ti}_3\text{C}_2\text{T}_x\text{-F}$ (−0.745 eV) is higher than that on $\text{Ti}_3\text{C}_2\text{T}_x$ (−0.621 eV), implying that oxygen-containing VOCs would be preferentially adsorbed on $\text{Ti}_3\text{C}_2\text{T}_x\text{-F}$. The local structure deformation induced by ethanol adsorption, together with an enhanced interaction of ethanol and $\text{Ti}_3\text{C}_2\text{T}_x\text{-F}$, sheds light on why the $\text{Ti}_3\text{C}_2\text{T}_x\text{-F}$ sensor has a superior sensing performance toward ethanol.

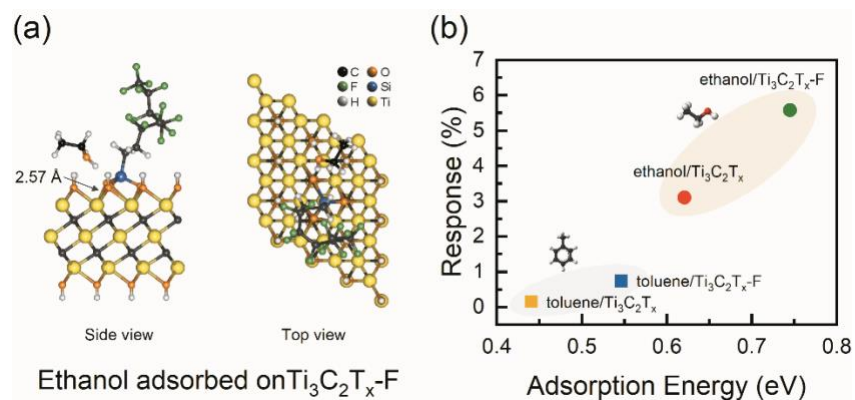


Fig. 7.15 (a) Side and top views of minimum energy configurations for an ethanol molecule (C₂H₅OH) adsorbed on Ti₃C₂T_x-F surface based on DFT simulations. (b) Calculated minimum adsorption energies of toluene and ethanol on Ti₃C₂T_x and Ti₃C₂T_x-F *versus* corresponding sensing responses.⁸¹

8. CONCLUSIONS AND FUTURE DIRECTIONS

8.1 Conclusions

We have reported Au-functionalized MoS₂ nanoflakes, fabricated through a facile solution mixing method, which have strong prospects for scalable production. Size distribution of Au nanoparticles is important for the achievement of high-performance gas sensors. With adequate decoration of 10-nm Au nanoparticles, MoS₂ sensor reveal highest selectivity and excellent response to oxygen-based VOCs owing to the electron-donating effect of Au nanoparticles and synergistic effects between Au-MoS₂, ambient oxygen species, and VOC analytes. Compared with the sensor made with pristine MoS₂, the Au-decorated MoS₂ sensors exhibit an enhancement of response by 131% towards detection of acetone. DFT simulations also support that the adsorption of VOC molecules on Au-decorated MoS₂ are stronger than on pristine MoS₂. The sensing mechanism of oxygen-based VOCs for Au-decorated MoS₂ is proposed as being dominated by the interaction between adsorbed oxygen species on MoS₂ and oxygen-containing VOCs.

We have successfully developed gas sensors based on Cu(I) pincer complex coated MoS₂-SCNT for selective detection of ethylene at room temperature. The sensors reveal a detection limit of 100 ppb. Incorporating 5×10^{-4} wt% SCNT into the MoS₂-SCNT composite supports conductivity on the order of 0.1 mS/cm, and further raised by functionalization of Cu(I) pincer complex. The air-stable Cu-Tm **2** acts as an n-type dopant of MoS₂ and a receptor of ethylene binding, which is transduced by modulations in conductance owing to the partial disruption of charge transfer between **2** and MoS₂. The thin-film sensor operates at low power and is compatible with battery-operated transceivers that can support applications in wireless ethylene monitoring, as demonstrated with authentic fruit samples. Thin-film sensors based on **2**-MoS₂-SCNT can be prepared with cost-effective and simple procedures, which have great potential for scalable production using continuous manufacturing processes.

We have demonstrated an inkjet-printing and wirelessly-operating sensor based on Ti₃C₂T_x/WSe₂ nanohybrids for the selective detection of oxygen-containing VOCs at room temperature. Inkjet printing allows repeatable fabrication of Ti₃C₂T_x/WSe₂ sensors, thus providing reproducible the sensing responses and low device-to-device variations. Compared with pristine Ti₃C₂T_x and pristine WSe₂ sensors, the Ti₃C₂T_x/WSe₂ hybrid sensor demonstrates a 12-fold

increase in ethanol sensitivity, good selectivity, low electrical noise, and ultrafast response/recovery properties. Furthermore, the $\text{Ti}_3\text{C}_2\text{T}_x/\text{WSe}_2$ displays hydration stability in humid environment, which overcomes the notorious instability and oxidization tendency of individual MXenes. The sensing enhancement for $\text{Ti}_3\text{C}_2\text{T}_x/\text{WSe}_2$ hybrid sensor is attributed to the numerous heterojunction interfaces for gas adsorption and its sensing mechanism is proposed. The hybridization strategy studied here can be an effective solution for preventing moisture degradation of MXenes and thus improves their promise for practical sensing applications.

We have reported a facile method functionalizing $\text{Ti}_3\text{C}_2\text{T}_x$ MXene with a superhydrophobic protection layer by employing FOTS-SAM. The contact angle, zeta potential, and XPS measurements confirms the formation of SAM layer on $\text{Ti}_3\text{C}_2\text{T}_x$. In particular, FOTS-functionalized $\text{Ti}_3\text{C}_2\text{T}_x$ not only provides hydration stability in humid environment, but also shows good tolerance in strong acidic and basic solutions. Moreover, using $\text{Ti}_3\text{C}_2\text{T}_x$ -F with larger interspacing as electrode material in a chemoresistive sensing configuration greatly improved the gas-sensing performance in terms of sensitivity, selectivity, and response/recovery times, especially in detecting of oxygen-based VOCs by offering a favorable structure with elevated adsorption sites and effective gas transport. DFT simulations indicate that the ethanol-induced structure deformation and the strong adsorption energy of ethanol on $\text{Ti}_3\text{C}_2\text{T}_x$ -F both likely contributed to gas-sensing enhancement. Thus, the functionalization strategy reported here have a great potential for developing highly reliable MXene-based sensors.

8.2 Future Perspectives

The significance of wearable and wireless technologies has been increasing rapidly with internet of things (IoTs), in which the integration of various functional devices into a multifunctional device deemed necessary for real-life applications, including power supply, sensing, communication, control, and response abilities. MXenes possess a unique combination of properties, including high (metal-based) electrical conductivity, large chemically active surface, adjustable hydrophilicity, and good colloidal dispersion in water, and thus have been explored recently in a variety of applications summarized in **Fig. 8.1**.

This study has used surface functionalization/hybridization of MXene to develop highly stable gas sensors, which can significantly improve the material stability and sensing performance that may be an effective way to protect oxidation of other MXene-based devices, such as

biomedical sensors, energy storage, electromagnetic interference shielding applications. The future directions are listed below based on the highly stable MXene-based materials through surface functionalization and hybridization.

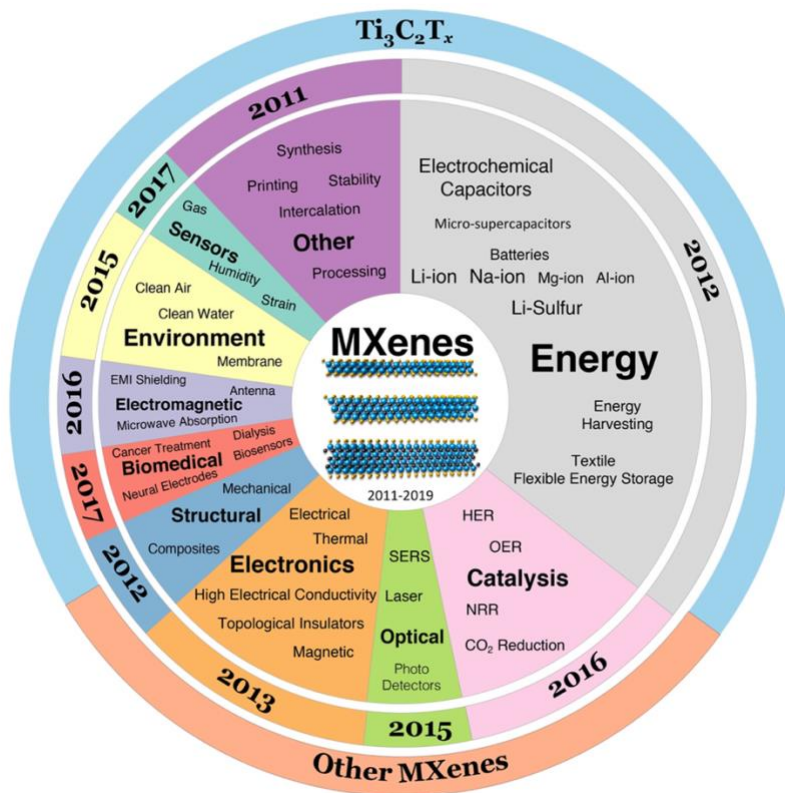


Fig. 8.1 The pie chart showing the potential applications of MXene materials for energy conversion/storage, catalysis, electromagnetic interference shielding, and biomedical sensors.

1. Increasing the number of gas sensors with different 2D materials for simultaneously identifying multiple VOCs based on electronic nose technology.
2. Fabricating gas sensors by cost- and time-effective roll-to-roll (R2R) production method. The solution processing of 2D materials proposed here is fully compatible with a R2R continuous production system.
3. Functionalizing highly stable MXene with ssDNA probes for selective detection of a diverse range of analytes including ions and biomolecules.
4. Optimizing the performance of biosensors based on ssDNA functionalized MXene.

REFERENCES

- 1 Geim, A. K.; Novoselov, K. S., The rise of graphene. *Nat. Mater.* **2007**, *6*, 183.
- 2 Deng, Y.; Luo, Z.; Conrad, N. J.; Liu, H.; Gong, Y.; Najmaei, S.; Ajayan, P. M.; Lou, J.; Xu, X.; Ye, P. D., Black phosphorus-monolayer MoS₂ van der Waals heterojunction p-n diode. *ACS Nano* **2014**, *8*, 8292.
- 3 Cho, B.; Yoon, J.; Lim, S. K.; Kim, A. R.; Kim, D. H.; Park, S. G.; Kwon, J. D.; Lee, Y. J.; Lee, K. H.; Lee, B. H.; Ko, H. C.; Hahm, M. G., Chemical sensing of 2D graphene/MoS₂ heterostructure device. *ACS Appl. Mater. Interfaces* **2015**, *7*, 16775.
- 4 Um, D. S.; Lee, Y.; Lim, S.; Park, S.; Lee, H.; Ko, H., High-performance MoS₂/CuO nanosheet-on-one-dimensional heterojunction photodetectors. *ACS Appl. Mater. Interfaces* **2016**, *8*, 33955.
- 5 Jariwala, D.; Sangwan, V. K.; Lauhon, L. J.; Marks, T. J.; Hersam, M. C., Emerging device applications for semiconducting two-dimensional transition metal dichalcogenides. *ACS Nano* **2014**, *8*, 1102.
- 6 Gogotsi, Y.; Anasori, B., The rise of MXenes. *ACS Nano* **2019**, *13*, 8491.
- 7 Kim, S. J.; Koh, H. J.; Ren, C. E.; Kwon, O.; Maleski, K.; Cho, S. Y.; Anasori, B.; Kim, C. K.; Choi, Y. K.; Kim, J.; Gogotsi, Y.; Jung, H. T., Metallic Ti₃C₂T_x MXene gas sensors with ultrahigh signal-to-noise ratio. *ACS Nano* **2018**, *12*, 986.
- 8 Meng, Z.; Stolz, R. M.; Mendecki, L.; Mirica, K. A., Electrically-transduced chemical sensors based on two-dimensional nanomaterials. *Chem. Rev.* **2019**, *119*, 478.
- 9 Bernal, M. M.; Álvarez, L.; Giovanelli, E.; Arnáiz, A.; Ruiz-González, L.; Casado, S.; Granados, D.; Pizarro, A. M.; Castellanos-Gomez, A.; Pérez, E. M., Luminescent transition metal dichalcogenide nanosheets through one-step liquid phase exfoliation. *2D Mater.* **2016**, *3*, 035014.
- 10 Zhang, J.; Liu, X.; Neri, G.; Pinna, N., Nanostructured materials for room-temperature gas sensors. *Adv. Mater.* **2016**, *28*, 795.
- 11 Liu, X.; Ma, T.; Pinna, N.; Zhang, J., Two-dimensional nanostructured materials for gas sensing. *Adv. Funct. Mater.* **2017**, *27*, 1702168.
- 12 Joshi, N.; Hayasaka, T.; Liu, Y.; Liu, H.; Oliveira, O. N.; Lin, L., A review on chemiresistive room temperature gas sensors based on metal oxide nanostructures, graphene and 2D transition metal dichalcogenides. *Microchim. Acta* **2018**, *185*, 213.
- 13 Radisavljevic, B.; Radenovic, A.; Brivio, J.; Giacometti, V.; Kis, A., Single-layer MoS₂ transistors. *Nat. Nanotechnol.* **2011**, *6*, 147.
- 14 Chhowalla, M.; Shin, H. S.; Eda, G.; Li, L. J.; Loh, K. P.; Zhang, H., The chemistry of two-dimensional layered transition metal dichalcogenide nanosheets. *Nat. Chem.* **2013**, *5*, 263.
- 15 Wang, Q. H.; Kalantar-Zadeh, K.; Kis, A.; Coleman, J. N.; Strano, M. S., Electronics and optoelectronics of two-dimensional transition metal dichalcogenides. *Nat. Nanotechnol.* **2012**, *7*, 699–712.
- 16 Wilson, J. A.; Yoffe, A. D., The transition metal dichalcogenides discussion and interpretation of the observed optical, electrical and structural properties. *Adv. Phys.* **1969**, *18*, 193.
- 17 Li, H.; Zhang, Q.; Yap, C. C. R.; Tay, B. K.; Edwin, T. H. T.; Olivier, A.; Baillargeat, D., From bulk to monolayer MoS₂: evolution of Raman scattering. *Adv. Funct. Mater.* **2012**, *22*, 1385.

- 18 Lee, C.; Yan, H.; Brus, L. E.; Heinz, T. F.; Hone, J.; Ryu, S., Anomalous lattice vibrations of single- and few-layer MoS₂. *ACS Nano* **2010**, 4, 2695.
- 19 Nguyen, E. P.; Carey, B. J.; Daeneke, T.; Ou, J. Z.; Latham, K.; Zhuiykov, S.; Kalantar-zadeh, K., Investigation of two-solvent grinding-assisted liquid phase exfoliation of layered MoS₂. *Chem. Mat.* **2014**, 27, 53.
- 20 Eda, G.; Yamaguchi, H.; Voiry, D.; Fujita, T.; Chen, M.; Chhowalla, M., Photoluminescence from chemically exfoliated MoS₂. *Nano Lett.* **2011**, 11, 5111.
- 21 Long, H.; Harley-Trochimczyk, A.; Pham, T.; Tang, Z.; Shi, T.; Zettl, A.; Carraro, C.; Worsley, M. A.; Maboudian, R., High surface area MoS₂/graphene hybrid aerogel for ultrasensitive NO₂ detection. *Adv. Funct. Mater.* **2016**, 26, 5158.
- 22 Li, P.; Zhang, D. Z.; Sun, Y. E.; Chang, H. Y.; Liu, J. J.; Yin, N. L., Towards intrinsic MoS₂ devices for high performance arsenite sensing. *Appl. Phys. Lett.* **2016**, 109, 063110.
- 23 Samnakay, R.; Jiang, C.; Rumyantsev, S. L.; Shur, M. S.; Balandin, A. A., Selective chemical vapor sensing with few-layer MoS₂ thin-film transistors: comparison with graphene devices. *Appl. Phys. Lett.* **2015**, 106, 023115.
- 24 Backes, C.; Szydłowska, B. M.; Harvey, A.; Yuan, S.; Vega-Mayoral, V.; Davies, B. R.; Zhao, P. L.; Hanlon, D.; Santos, E. J.; Katsnelson, M. I.; Blau, W. J.; Gadermaier, C.; Coleman, J. N., Production of highly monolayer enriched dispersions of liquid-exfoliated nanosheets by liquid cascade centrifugation. *ACS Nano* **2016**, 10, 1589.
- 25 Cho, B.; Kim, A. R.; Park, Y.; Yoon, J.; Lee, Y. J.; Lee, S.; Yoo, T. J.; Kang, C. G.; Lee, B. H.; Ko, H. C.; Kim, D. H.; Hahm, M. G., Bifunctional sensing characteristics of chemical vapor deposition synthesized atomic-layered MoS₂. *ACS Appl. Mater. Interfaces* **2015**, 7, 2952.
- 26 Donarelli, M.; Prezioso, S.; Perrozzi, F.; Bisti, F.; Nardone, M.; Giancaterini, L.; Cantalini, C.; Ottaviano, L., Response to NO₂ and other gases of resistive chemically exfoliated MoS₂-based gas sensors. *Sens. Actuator B-Chem.* **2015**, 207, 602.
- 27 Li, H.; Yin, Z.; He, Q.; Li, H.; Huang, X.; Lu, G.; Fam, D. W.; Tok, A. I.; Zhang, Q.; Zhang, H., Fabrication of single- and multilayer MoS₂ film-based field-effect transistors for sensing NO at room temperature. *Small* **2012**, 8, 63–67.
- 28 Cho, B.; Hahm, M. G.; Choi, M.; Yoon, J.; Kim, A. R.; Lee, Y. J.; Park, S. G.; Kwon, J. D.; Kim, C. S.; Song, M.; Jeong, Y.; Nam, K. S.; Lee, S.; Yoo, T. J.; Kang, C. G.; Lee, B. H.; Ko, H. C.; Ajayan, P. M.; Kim, D. H., Charge-transfer-based gas sensing using atomic-layer MoS₂. *Sci. Rep.* **2015**, 5, 8052.
- 29 Perkins, F. K.; Friedman, A. L.; Cobas, E.; Campbell, P. M.; Jernigan, G. G.; Jonker, B. T., Chemical vapor sensing with monolayer MoS₂. *Nano Lett.* **2013**, 13, 668.
- 30 Kim, J. S.; Yoo, H. W.; Choi, H. O.; Jung, H. T., Tunable volatile organic compounds sensor by using thiolated ligand conjugation on MoS₂. *Nano Lett.* **2014**, 14, 5941.
- 31 Cho, S. Y.; Koh, H. J.; Yoo, H. W.; Kim, J. S.; Jung, H. T., Tunable volatile-organic-compound sensor by using Au nanoparticle incorporation on MoS₂. *ACS Sens.* **2017**, 2, 183.
- 32 Cho, S. Y.; Yoo, H. W.; Kim, J. Y.; Jung, W. B.; Jin, M. L.; Kim, J. S.; Jeon, H. J.; Jung, H. T., High-resolution p type metal oxide semiconductor nanowire array as an ultrasensitive sensor for volatile organic compounds. *Nano Lett.* **2016**, 16, 4508.
- 33 Ma, H.; Xu, Y.; Rong, Z.; Cheng, X.; Gao, S.; Zhang, X.; Zhao, H.; Huo, L., Highly toluene sensing performance based on monodispersed Cr₂O₃ porous microspheres. *Sens. Actuator B-Chem.* **2012**, 174, 325.

- 34 Yang, W.; Gan, L.; Li, H.; Zhai, T., Two-dimensional layered nanomaterials for gas-sensing applications. *Inorg. Chem. Front.* **2016**, 3, 433.
- 35 Yue, Q.; Shao, Z.; Chang, S.; Li, J., Adsorption of gas molecules on monolayer MoS₂ and effect of applied electric field. *Nanoscale Res. Lett.* **2013**, 8, 425.
- 36 Ou, J. Z.; Ge, W.; Carey, B.; Daeneke, T.; Rotbart, A.; Shan, W.; Wang, Y.; Fu, Z.; Chrimes, A. F.; Wlodarski, W.; Russo, S. P.; Li, Y. X.; Kalantar-Zadeh, K., Physisorption-based charge transfer in two-dimensional SnS₂ for selective and reversible NO₂ gas sensing. *ACS Nano* **2015**, 9, 10313.
- 37 Kajiyama, S.; Szabova, L.; Iinuma, H.; Sugahara, A.; Gotoh, K.; Sodeyama, K.; Tateyama, Y.; Okubo, M.; Yamada, A., Enhanced Li-ion accessibility in MXene titanium carbide by steric chloride termination. *Adv Energy Mater* **2017**, 7, 1601873.
- 38 Dong, Y.; Chertopalov, S.; Maleski, K.; Anasori, B.; Hu, L.; Bhattacharya, S.; Rao, A. M.; Gogotsi, Y.; Mochalin, V. N.; Podila, R., Saturable absorption in 2D Ti₃C₂ MXene thin films for passive photonic diodes. *Adv. Mater.* **2018**, 30, 1705714.
- 39 Hantanasirisakul, K.; Zhao, M.-Q.; Urbankowski, P.; Halim, J.; Anasori, B.; Kota, S.; Ren, C. E.; Barsoum, M. W.; Gogotsi, Y., Fabrication of Ti₃C₂T_x MXene transparent thin films with tunable optoelectronic properties. *Adv. Electron. Mater.* **2016**, 2.
- 40 Hantanasirisakul, K.; Gogotsi, Y., Electronic and optical properties of 2D transition metal carbides and nitrides (MXenes). *Adv. Mater.* **2018**, 30, 1804779.
- 41 Zhang, C. J.; Anasori, B.; Seral-Ascaso, A.; Park, S.-H.; McEvoy, N.; Shmeliov, A.; Duesberg, G. S.; Coleman, J. N.; Gogotsi, Y.; Nicolosi, V., Transparent, flexible, and conductive 2D titanium carbide (MXene) films with high volumetric capacitance. *Adv. Mater.* **2017**, 29, 1702678.
- 42 Naguib, M.; Kurtoglu, M.; Presser, V.; Lu, J.; Niu, J.; Heon, M.; Hultman, L.; Gogotsi, Y.; Barsoum, M. W., Two-dimensional nanocrystals produced by exfoliation of Ti₃AlC₂. *Adv. Mater.* **2011**, 23, 4248.
- 43 Anasori, B.; Lukatskaya, M. R.; Gogotsi, Y., 2D metal carbides and nitrides (MXenes) for energy storage. *Nat. Rev. Mater.* **2017**, 2, 16098.
- 44 Lee, E.; VahidMohammadi, A.; Yoon, Y. S.; Beidaghi, M.; Kim, D. J., Two-dimensional vanadium carbide MXene for gas sensors with ultrahigh sensitivity toward nonpolar gases. *ACS Sens.* **2019**, 4, 1603.
- 45 Wang, Y.-T.; Whang, W.-T.; Chen, C.-H., Hollow V₂O₅ nanoassemblies for high-performance room-temperature hydrogen sensors. *ACS Appl. Mater. Interfaces* **2015**, 7, 8480.
- 46 Korotcenkov, G., Metal oxides for solid-state gas sensors: what determines our choice? *Mater. Sci. Eng. B* **2007**, 139, 1.
- 47 Janata, J., Conductometric sensors. *Principles of Chemical Sensors* **2009**, 241.
- 48 Chen, G.; Paronyan, T. M.; Pigos, E. M.; Harutyunyan, A. R., Enhanced gas sensing in pristine carbon nanotubes under continuous ultraviolet light illumination. *Sci. Rep.* **2012**, 2, 343.
- 49 Zhao, P. X.; Tang, Y.; Mao, J.; Chen, Y. X.; Song, H.; Wang, J. W.; Song, Y.; Liang, Y. Q.; Zhang, X. M., One-dimensional MoS₂-decorated TiO₂ nanotube gas sensors for efficient alcohol sensing. *J Alloy Compd* **2016**, 674, 252.
- 50 Ji, F.; Ren, X.; Zheng, X.; Liu, Y.; Pang, L.; Jiang, J.; Liu, S. F., 2D-MoO₃ nanosheets for superior gas sensors. *Nanoscale* **2016**, 8, 8696–8703.

- 51 Yan, H. H.; Song, P.; Zhang, S.; Yang, Z. X.; Wang, Q., Dispersed SnO₂ nanoparticles on MoS₂ nanosheets for superior gas-sensing performances to ethanol. *RSC Adv.* **2015**, *5*, 79593.
- 52 Yan, H.; Song, P.; Zhang, S.; Yang, Z.; Wang, Q., Facile synthesis, characterization and gas sensing performance of ZnO nanoparticles-coated MoS₂ nanosheets. *J Alloy Compd* **2016**, *662*, 118.
- 53 Yavari, F.; Chen, Z.; Thomas, A. V.; Ren, W.; Cheng, H. M.; Koratkar, N., High sensitivity gas detection using a macroscopic three-dimensional graphene foam network. *Sci. Rep.* **2011**, *1*, 166.
- 54 Zhou, Y.; Jiang, Y.; Xie, T.; Tai, H.; Xie, G., A novel sensing mechanism for resistive gas sensors based on layered reduced graphene oxide thin films at room temperature. *Sens. Actuator B-Chem.* **2014**, *203*, 135.
- 55 Lee, E.; VahidMohammadi, A.; Prorok, B. C.; Yoon, Y. S.; Beidaghi, M.; Kim, D. J., Room temperature gas sensing of two-dimensional titanium carbide (MXene). *ACS Appl. Mater. Interfaces* **2017**, *9*, 37184.
- 56 Yuan, W.; Yang, K.; Peng, H.; Li, F.; Yin, F., A flexible VOCs sensor based on a 3D MXene framework with a high sensing performance. *J Mater. Chem. A* **2018**, *6*, 18116.
- 57 Koh, H. J.; Kim, S. J.; Maleski, K.; Cho, S. Y.; Kim, Y. J.; Ahn, C. W.; Gogotsi, Y.; Jung, H. T., Enhanced selectivity of MXene gas sensors through metal ion intercalation: in situ X-ray diffraction study. *ACS Sens.* **2019**, *4*, 1365.
- 58 Ko, K. Y.; Park, K.; Lee, S.; Kim, Y.; Woo, W. J.; Kim, D.; Song, J. G.; Park, J.; Kim, H., Recovery improvement for large-area tungsten diselenide gas sensors. *ACS Appl. Mater. Interfaces* **2018**, *10*, 23910.
- 59 Kim, Y. H.; Kim, K. Y.; Choi, Y. R.; Shim, Y.-S.; Jeon, J.-M.; Lee, J.-H.; Kim, S. Y.; Han, S.; Jang, H. W., Ultrasensitive reversible oxygen sensing by using liquid-exfoliated MoS₂ nanoparticles. *J. Mater. Chem. A* **2016**, *4*, 6070.
- 60 Ikram, M.; Liu, L.; Liu, Y.; Ma, L.; Lv, H.; Ullah, M.; He, L.; Wu, H.; Wang, R.; Shi, K., Fabrication and characterization of a high-surface area MoS₂@WS₂ heterojunction for the ultra-sensitive NO₂ detection at room temperature. *J. Mater. Chem. A* **2019**, *7*, 14602.
- 61 Yang, K.; Wang, X.; Li, H.; Chen, B.; Zhang, X.; Li, S.; Wang, N.; Zhang, H.; Huang, X.; Huang, W., Composition- and phase-controlled synthesis and applications of alloyed phase heterostructures of transition metal disulphides. *Nanoscale* **2017**, *9*, 5102.
- 62 Ko, K. Y.; Song, J. G.; Kim, Y.; Choi, T.; Shin, S.; Lee, C. W.; Lee, K.; Koo, J.; Lee, H.; Kim, J.; Lee, T.; Park, J.; Kim, H., Improvement of gas-sensing performance of large-area tungsten disulfide nanosheets by surface functionalization. *ACS Nano* **2016**, *10*, 9287.
- 63 Chen, W. Y.; Yen, C. C.; Xue, S.; Wang, H.; Stanciu, L. A., Surface functionalization of layered molybdenum disulfide for the selective detection of volatile organic compounds at room temperature. *ACS Appl. Mater. Interfaces* **2019**, *11*, 34135–34143.
- 64 Ouyang, C.; Chen, Y.; Qin, Z.; Zeng, D.; Zhang, J.; Wang, H.; Xie, C., Two-dimensional WS₂-based nanosheets modified by Pt quantum dots for enhanced room-temperature NH₃ sensing properties. *Appl. Surf. Sci.* **2018**, *455*, 45.
- 65 Wang, X.; Gu, D.; Li, X.; Lin, S.; Zhao, S.; Rumyantseva, M. N.; Gaskov, A. M., Reduced graphene oxide hybridized with WS₂ nanoflakes based heterojunctions for selective ammonia sensors at room temperature. *Sens. Actuator B-Chem.* **2019**, *282*, 290.

- 66 Zhang, D. Z.; Liu, A. M.; Chang, H. Y.; Xia, B. K., Room-temperature high-performance acetone gas sensor based on hydrothermal synthesized SnO₂-reduced graphene oxide hybrid composite. *RSC Adv.* **2015**, 5, 3016.
- 67 Liu, L.; Zhang, D.; Zhang, Q.; Chen, X.; Xu, G.; Lu, Y.; Liu, Q., Smartphone-based sensing system using ZnO and graphene modified electrodes for VOCs detection. *Biosens. Bioelectron.* **2017**, 93, 94.
- 68 Zhang, S.-L.; Yue, H.; Liang, X.; Yang, W.-C., Liquid-phase co-exfoliated graphene/MoS₂ nanocomposite for methanol gas sensing. *J. Nanosci. Nanotechnol.* **2015**, 15, 8004.
- 69 Ganatra, R.; Zhang, Q., Few-layer MoS₂: a promising layered semiconductor. *ACS Nano* **2014**, 8, 4074.
- 70 Liu, K. K.; Zhang, W.; Lee, Y. H.; Lin, Y. C.; Chang, M. T.; Su, C. Y.; Chang, C. S.; Li, H.; Shi, Y.; Zhang, H.; Lai, C. S.; Li, L. J., Growth of large-area and highly crystalline MoS₂ thin layers on insulating substrates. *Nano Lett.* **2012**, 12, 1538.
- 71 Zhan, Y.; Liu, Z.; Najmaei, S.; Ajayan, P. M.; Lou, J., Large-area vapor-phase growth and characterization of MoS₂ atomic layers on a SiO₂ substrate. *Small* **2012**, 8, 966.
- 72 Lee, Y. H.; Zhang, X. Q.; Zhang, W.; Chang, M. T.; Lin, C. T.; Chang, K. D.; Yu, Y. C.; Wang, J. T.; Chang, C. S.; Li, L. J.; Lin, T. W., Synthesis of large-area MoS₂ atomic layers with chemical vapor deposition. *Adv. Mater.* **2012**, 24, 2320.
- 73 Lv, R. T.; Terrones, H.; Elias, A. L.; Perea-Lopez, N.; Gutierrez, H. R.; Cruz-Silva, E.; Rajukumar, L. P.; Dresselhaus, M. S.; Terrones, M., Two-dimensional transition metal dichalcogenides: clusters, ribbons, sheets and more. *Nano Today* **2015**, 10, 559.
- 74 Zhou, K. G.; Mao, N. N.; Wang, H. X.; Peng, Y.; Zhang, H. L., A mixed-solvent strategy for efficient exfoliation of inorganic graphene analogues. *Angew. Chem.-Int. Edit.* **2011**, 50, 10839.
- 75 Bissett, M. A.; Kinloch, I. A.; Dryfe, R. A., Characterization of MoS₂-graphene composites for high-performance coin cell supercapacitors. *ACS Appl. Mater. Interfaces* **2015**, 7, 17388.
- 76 Alhabeab, M.; Maleski, K.; Anasori, B.; Lelyukh, P.; Clark, L.; Sin, S.; Gogotsi, Y., Guidelines for synthesis and processing of two-dimensional titanium carbide (Ti₃C₂T_x MXene). *Chem. Mater.* **2017**, 29, 7633.
- 77 Naguib, M.; Mashtalir, O.; Carle, J.; Presser, V.; Lu, J.; Hultman, L.; Gogotsi, Y.; Barsoum, M. W., Two-dimensional transition metal carbides. *ACS Nano* **2012**, 6, 1322–1331.
- 78 Callister, W. D.; Rethwisch, D. G., 2020.
- 79 Ying, Y.; Liu, Y.; Wang, X.; Mao, Y.; Cao, W.; Hu, P.; Peng, X., Two-dimensional titanium carbide for efficiently reductive removal of highly toxic chromium(VI) from water. *ACS Appl. Mater. Interfaces* **2015**, 7, 1795.
- 80 Chen, W. Y.; Jiang, X.; Lai, S. N.; Peroulis, D.; Stanciu, L., Nanohybrids of a MXene and transition metal dichalcogenide for selective detection of volatile organic compounds. *Nat. Commun.* **2020**, 11, 1302.
- 81 Chen, W. Y.; Lai, S. N.; Yen, C. C.; Jiang, X.; Peroulis, D.; Stanciu, L. A., Surface functionalization of Ti₃C₂T_x mxene with highly reliable superhydrophobic protection for volatile organic compounds sensing. *ACS Nano* **2020**, 14, 11490.
- 82 **!!! INVALID CITATION !!! 81.**
- 83 Behera, B.; Chandra, S., A MEMS based acetone sensor incorporating ZnO nanowires synthesized by wet oxidation of Zn film. *J. Micromech. Microeng.* **2015**, 25, 015007.

- 84 Yaws, C. L.; Satyro, M. A., in *The Yaws Handbook of Vapor Pressure (Second Edition)*, (Ed: C. L. Yaws), Gulf Professional Publishing, 2015, 1.
- 85 Kannan, P. K.; Late, D. J.; Morgan, H.; Rout, C. S., Recent developments in 2D layered inorganic nanomaterials for sensing. *Nanoscale* **2015**, 7, 13293.
- 86 Sinha, M.; Mahapatra, R.; Mondal, B.; Maruyama, T.; Ghosh, R., Ultrafast and reversible gas-sensing properties of ZnO nanowire arrays grown by hydrothermal technique. *J Phys Chem C* **2016**, 120, 3019.
- 87 Kim, J.; Byun, S.; Smith, A. J.; Yu, J.; Huang, J., Enhanced electrocatalytic properties of transition-metal dichalcogenides sheets by spontaneous gold nanoparticle decoration. *J. Phys. Chem. Lett.* **2013**, 4, 1227–1232.
- 88 Sreepasad, T. S.; Nguyen, P.; Kim, N.; Berry, V., Controlled, defect-guided, metal-nanoparticle incorporation onto MoS₂ via chemical and microwave routes: electrical, thermal, and structural properties. *Nano Lett.* **2013**, 13, 4434–4441.
- 89 Han, T.-L.; Wan, Y.-T.; Li, J.-J.; Zhang, H.-G.; Liu, J.-H.; Huang, X.-J.; Liu, J.-Y., In situ gold nanoparticle-decorated three-dimensional tin dioxide nanostructures for sensitive and selective gas-sensing detection of volatile organic compounds. *J. Mater. Chem. C* **2017**, 5, 6193–6201.
- 90 Bandgar, D. K.; Navale, S. T.; Khuspe, G. D.; Pawar, S. A.; Mulik, R. N.; Patil, V. B., Novel route for fabrication of nanostructured α -Fe₂O₃ gas sensor. *Mater. Sci. Semicond. Process* **2014**, 17, 67.
- 91 Yan, W.; Harley-Trochimczyk, A.; Long, H.; Chan, L.; Pham, T.; Hu, M.; Qin, Y.; Zettl, A.; Carraro, C.; Worsley, M. A.; Maboudian, R., Conductometric gas sensing behavior of WS₂ aerogel. *FlatChem* **2017**, 5, 1.
- 92 Li, X.; Li, X.; Li, Z.; Wang, J.; Zhang, J., WS₂ nanoflakes based selective ammonia sensors at room temperature. *Sens. Actuator B-Chem.* **2017**, 240, 273.
- 93 Chen, W. Y.; Yermembetova, A.; Washer, B. M.; Jiang, X.; Shuvo, S. N.; Peroulis, D.; Wei, A.; Stanciu, L. A., Selective detection of ethylene by MoS₂-carbon nanotube networks coated with Cu(I)-pincer complexes. *ACS Sens.* **2020**, 5, 1699.
- 94 Ryu, M. Y.; Jang, H. K.; Lee, K. J.; Piao, M.; Ko, S. P.; Shin, M.; Huh, J.; Kim, G. T., Triethanolamine doped multilayer MoS₂ field effect transistors. *Phys. Chem. Chem. Phys.* **2017**, 19, 13133.
- 95 Sim, D. M.; Kim, M.; Yim, S.; Choi, M. J.; Choi, J.; Yoo, S.; Jung, Y. S., Controlled doping of vacancy-containing few-layer MoS₂ via highly stable thiol-based molecular chemisorption. *ACS Nano* **2015**, 9, 12115.
- 96 Fang, H.; Tosun, M.; Seol, G.; Chang, T. C.; Takei, K.; Guo, J.; Javey, A., Degenerate n-doping of few-layer transition metal dichalcogenides by potassium. *Nano Lett.* **2013**, 13, 1991.
- 97 Yang, L.; Majumdar, K.; Liu, H.; Du, Y.; Wu, H.; Hatzistergos, M.; Hung, P. Y.; Tieckelmann, R.; Tsai, W.; Hobbs, C.; Ye, P. D., Chloride molecular doping technique on 2D materials: WS₂ and MoS₂. *Nano Lett.* **2014**, 14, 6275.
- 98 Qu, D.; Liu, X.; Huang, M.; Lee, C.; Ahmed, F.; Kim, H.; Ruoff, R. S.; Hone, J.; Yoo, W. J., Carrier-type modulation and mobility improvement of thin MoTe₂. *Adv. Mater.* **2017**, 29, 1606433.
- 99 Koroteev, V. O.; Bulusheva, L. G.; Asanov, I. P.; Shlyakhova, E. V.; Vyalikh, D. V.; Okotrub, A. V., Charge transfer in the MoS₂/carbon nanotube composite. *J Phys Chem C* **2011**, 115, 21199.

- 100 Fukumaru, T.; Fujigaya, T.; Nakashima, N., Development of n-type cobaltocene-encapsulated carbon nanotubes with remarkable thermoelectric property. *Sci. Rep.* **2015**, *5*, 7951.
- 101 Pham, V. P.; Yeom, G. Y., Recent advances in doping of molybdenum disulfide: industrial applications and future prospects. *Adv. Mater.* **2016**, *28*, 9024.
- 102 Dodds, C. A.; Garner, M.; Reglinski, J.; Spicer, M. D., Coinage metal complexes of a boron-substituted soft scorpionate ligand. *Inorg. Chem.* **2006**, *45*, 2733.
- 103 Smith, J. M., Strongly donating scorpionate ligands. *Comments Inorganic Chem.* **2008**, *29*, 189.
- 104 Fu, W.; van Dijkman, T. F.; Lima, L. M. C.; Jiang, F.; Schneider, G. F.; Bouwman, E., Ultrasensitive ethene detector based on a graphene-copper(I) hybrid material. *Nano Lett.* **2017**, *17*, 7980.
- 105 Esser, B.; Schnorr, J. M.; Swager, T. M., Selective detection of ethylene gas using carbon nanotube-based devices: utility in determination of fruit ripeness. *Angew. Chem.-Int. Edit.* **2012**, *51*, 5752.
- 106 Pesis, E., The role of the anaerobic metabolites, acetaldehyde and ethanol, in fruit ripening, enhancement of fruit quality and fruit deterioration. *Postharvest Biol. Technol.* **2005**, *37*, 1.
- 107 Barry, C. S.; Giovannoni, J. J., Ethylene and fruit ripening. *J. Plant Growth Regul.* **2007**, *26*, 143.
- 108 Janssen, S.; Schmitt, K.; Blanke, M.; Bauersfeld, M. L.; Wollenstein, J.; Lang, W., Ethylene detection in fruit supply chains. *Phil. Trans. R. Soc. A* **2014**, *372*, 20130311.
- 109 Cherian, S.; Figueroa, C. R.; Nair, H., 'Movers and shakers' in the regulation of fruit ripening: a cross-dissection of climacteric versus non-climacteric fruit. *J. Exp. Bot.* **2014**, *65*, 4705.
- 110 Liu, M.; Pirrello, J.; Chervin, C.; Roustan, J. P.; Bouzayen, M., Ethylene control of fruit ripening: revisiting the complex network of transcriptional regulation. *Plant Physiol.* **2015**, *169*, 2380.
- 111 Ko, K. Y.; Lee, S.; Park, K.; Kim, Y.; Woo, W. J.; Kim, D.; Song, J. G.; Park, J.; Kim, J. H.; Lee, Z.; Kim, H., High-performance gas sensor using a large-area $WS_{2x}Se_{2-2x}$ alloy for low-power operation wearable applications. *ACS Appl. Mater. Interfaces* **2018**, *10*, 34163.
- 112 Rakhi, R. B.; Ahmed, B.; Hedhili, M. N.; Anjum, D. H.; Alshareef, H. N., Effect of postetch annealing gas composition on the structural and electrochemical properties of Ti_2CT_x MXene electrodes for supercapacitor applications. *Chem. Mater.* **2015**, *27*, 5314.
- 113 Shah, S. A.; Habib, T.; Gao, H.; Gao, P.; Sun, W.; Green, M. J.; Radovic, M., Template-free 3D titanium carbide ($Ti_3C_2T_x$) MXene particles crumpled by capillary forces. *Chem. Commun.* **2016**, *53*, 400.
- 114 Liu, Y. T.; Zhang, P.; Sun, N.; Anasori, B.; Zhu, Q. Z.; Liu, H.; Gogotsi, Y.; Xu, B., Self-assembly of transition metal oxide nanostructures on MXene nanosheets for fast and stable lithium storage. *Adv. Mater.* **2018**, *30*, 1707334.
- 115 Du, C. F.; Dinh, K. N.; Liang, Q.; Zheng, Y.; Luo, Y.; Zhang, J.; Yan, Q., Self-assemble and in situ formation of $Ni_{1-x}Fe_xPS_3$ nanomosaic-decorated MXene hybrids for overall water splitting. *Adv Energy Mater* **2018**, *8*, 1801127.
- 116 Ran, J.; Gao, G.; Li, F. T.; Ma, T. Y.; Du, A.; Qiao, S. Z., Ti_3C_2 MXene co-catalyst on metal sulfide photo-absorbers for enhanced visible-light photocatalytic hydrogen production. *Nat. Commun.* **2017**, *8*, 13907.

- 117 Lipatov, A.; Alhabeab, M.; Lukatskaya, M. R.; Boson, A.; Gogotsi, Y.; Sinitskii, A., Effect of synthesis on quality, electronic properties and environmental stability of individual monolayer Ti_3C_2 MXene flakes. *Adv. Electron. Mater.* **2016**, *2*, 1600255.
- 118 Zhang, C. J.; Pinilla, S.; McEvoy, N.; Cullen, C. P.; Anasori, B.; Long, E.; Park, S.-H.; Seral-Ascaso, A.; Shmeliov, A.; Krishnan, D.; Morant, C.; Liu, X.; Duesberg, G. S.; Gogotsi, Y.; Nicolosi, V., Oxidation stability of colloidal two-dimensional titanium carbides (MXenes). *Chem. Mater.* **2017**, *29*, 4848.
- 119 Habib, T.; Zhao, X.; Shah, S. A.; Chen, Y.; Sun, W.; An, H.; Lutkenhaus, J. L.; Radovic, M.; Green, M. J., Oxidation stability of $Ti_3C_2T_x$ MXene nanosheets in solvents and composite films. *NPJ 2D Mater. Appl.* **2019**, *3*, 8.
- 120 Hoppe, M.; Ababii, N.; Postica, V.; Lupan, O.; Polonskyi, O.; Schütt, F.; Kaps, S.; Sukhodub, L. F.; Sontea, V.; Strunskus, T.; Faupel, F.; Adelung, R., (CuO-Cu₂O)/ZnO:Al heterojunctions for volatile organic compound detection. *Sens. Actuator B-Chem.* **2018**, *255*, 1362.
- 121 Dillon, A. D.; Ghidui, M. J.; Krick, A. L.; Griggs, J.; May, S. J.; Gogotsi, Y.; Barsoum, M. W.; Fafarman, A. T., Highly conductive optical quality solution-processed films of 2D titanium carbide. *Adv. Funct. Mater.* **2016**, *26*, 4162.
- 122 Li, B.; Guo, H.; Wang, Y.; Zhang, W.; Zhang, Q.; Chen, L.; Fan, X.; Zhang, W.; Li, Y.; Lau, W.-M., Asymmetric MXene/monolayer transition metal dichalcogenide heterostructures for functional applications. *Npj Comput. Mater.* **2019**, *5*, 1–8.
- 123 Zhao, X.; Vashisth, A.; Prehn, E.; Sun, W.; Shah, S. A.; Habib, T.; Chen, Y.; Tan, Z.; Lutkenhaus, J. L.; Radovic, M.; Green, M. J., Antioxidants unlock shelf-stable $Ti_3C_2T_x$ (MXene) nanosheet dispersions. *Matter* **2019**, *1*, 513.
- 124 Cui, S.; Wen, Z.; Huang, X.; Chang, J.; Chen, J., Stabilizing MoS₂ nanosheets through SnO₂ nanocrystal decoration for high-performance gas sensing in air. *Small* **2015**, *11*, 2305–2313.
- 125 Kumar, S.; Lei, Y.; Alshareef, N. H.; Quevedo-Lopez, M. A.; Salama, K. N., Biofunctionalized two-dimensional Ti_3C_2 MXenes for ultrasensitive detection of cancer biomarker. *Biosens. Bioelectron.* **2018**, *121*, 243.
- 126 Zhao, J.; Yang, Y.; Yang, C.; Tian, Y.; Han, Y.; Liu, J.; Yin, X.; Que, W., A hydrophobic surface enabled salt-blocking 2D Ti_3C_2 MXene membrane for efficient and stable solar desalination. *J. Mater. Chem. A* **2018**, *6*, 16196.
- 127 Riazi, H.; Anayee, M.; Hantanasirisakul, K.; Shamsabadi, A. A.; Anasori, B.; Gogotsi, Y.; Soroush, M., Surface modification of a MXene by an aminosilane coupling agent. *Adv. Mater. Interfaces* **2020**, *7*, 1902008.
- 128 Ahangaran, F.; Hassanzadeh, A.; Nouri, S., Surface modification of Fe₃O₄@SiO₂ microsphere by silane coupling agent. *Int. Nano Lett.* **2013**, *3*, 23.
- 129 Worsley, M. A.; Shin, S. J.; Merrill, M. D.; Lenhardt, J.; Nelson, A. J.; Woo, L. Y.; Gash, A. E.; Baumann, T. F.; Orme, C. A., Ultralow density, monolithic WS₂, MoS₂, and MoS₂/graphene aerogels. *ACS Nano* **2015**, *9*, 4698.
- 130 Liu, J.; Zhang, H. B.; Sun, R.; Liu, Y.; Liu, Z.; Zhou, A.; Yu, Z. Z., Hydrophobic, Flexible, and Lightweight MXene Foams for High-Performance Electromagnetic-Interference Shielding. *Adv Mater* **2017**, *29*.
- 131 Zhao, D.; Clites, M.; Ying, G.; Kota, S.; Wang, J.; Natu, V.; Wang, X.; Pomerantseva, E.; Cao, M.; Barsoum, M. W., Alkali-induced crumpling of $Ti_3C_2T_x$ (MXene) to form 3D porous networks for sodium ion storage. *Chem. Commun.* **2018**, *54*, 4533.

- 132 Song, G.; Kim, Y.; Yu, S.; Kim, M.-O.; Park, S.-H.; Cho, S. M.; Velusamy, D. B.; Cho, S. H.; Kim, K. L.; Kim, J.; Kim, E.; Park, C., Molecularly engineered surface triboelectric nanogenerator by self-assembled monolayers (METS). *Chem. Mater.* **2015**, *27*, 4749.
- 133 Zhang, F.; Chen, S.; Dong, L.; Lei, Y.; Liu, T.; Yin, Y., Preparation of superhydrophobic films on titanium as effective corrosion barriers. *Appl. Surf. Sci.* **2011**, *257*, 2587.
- 134 Peng, C.; Yang, X.; Li, Y.; Yu, H.; Wang, H.; Peng, F., Hybrids of two-dimensional Ti₃C₂ and TiO₂ exposing {001} facets toward enhanced photocatalytic activity. *ACS Appl. Mater. Interfaces* **2016**, *8*, 6051.
- 135 Ren, C. E.; Zhao, M.-Q.; Makaryan, T.; Halim, J.; Boota, M.; Kota, S.; Anasori, B.; Barsoum, M. W.; Gogotsi, Y., Porous two-dimensional transition metal carbide (MXene) flakes for high-performance li-ion storage. *ChemElectroChem* **2016**, *3*, 689.
- 136 Cai, Y.; Li, J.; Yi, L.; Yan, X.; Li, J., Fabricating superhydrophobic and oleophobic surface with silica nanoparticles modified by silanes and environment-friendly fluorinated chemicals. *Appl. Surf. Sci.* **2018**, *450*, 102.
- 137 Li, Y.; Xu, C. Y.; Hu, P.; Zhen, L., Carrier control of MoS₂ nanoflakes by functional self-assembled monolayers. *ACS Nano* **2013**, *7*, 7795.
- 138 Shin, S. H.; Kwon, Y. H.; Kim, Y. H.; Jung, J. Y.; Lee, M. H.; Nah, J., Triboelectric charging sequence induced by surface functionalization as a method to fabricate high performance triboelectric generators. *ACS Nano* **2015**, *9*, 4621.
- 139 Yoo, D.; Kim, Y.; Min, M.; Ahn, G. H.; Lien, D. H.; Jang, J.; Jeong, H.; Song, Y.; Chung, S.; Javey, A.; Lee, T., Highly reliable superhydrophobic protection for organic field-effect transistors by fluoroalkylsilane-coated TiO₂ nanoparticles. *ACS Nano* **2018**, *12*, 11062.
- 140 Jiang, Y.; Tang, N.; Zhou, C.; Han, Z.; Qu, H.; Duan, X., A chemiresistive sensor array from conductive polymer nanowires fabricated by nanoscale soft lithography. *Nanoscale* **2018**, *10*, 20578.
- 141 Cho, S.-Y.; Lee, Y.; Koh, H.-J.; Jung, H.; Kim, J.-S.; Yoo, H.-W.; Kim, J.; Jung, H.-T., Superior chemical sensing performance of black phosphorus: comparison with MoS₂ and graphene. *Adv. Mater.* **2016**, *28*, 7020–7028.
- 142 Raghu, A. V.; Karuppanan, K. K.; Nampoothiri, J.; Pullithadathil, B., Wearable, flexible ethanol gas sensor based on TiO₂ nanoparticles-grafted 2D-titanium carbide nanosheets. *ACS Appl. Nano Mater.* **2019**, *2*, 1152–1163.
- 143 Naguib, M.; Mochalin, V. N.; Barsoum, M. W.; Gogotsi, Y., 25th anniversary article: MXenes: a new family of two-dimensional materials. *Adv. Mater.* **2014**, *26*, 992–1005.
- 144 Yu, X. F.; Li, Y. C.; Cheng, J. B.; Liu, Z. B.; Li, Q. Z.; Li, W. Z.; Yang, X.; Xiao, B., Monolayer Ti₂CO₂: a promising candidate for NH₃ sensor or capturer with high sensitivity and selectivity. *ACS Appl. Mater. Interfaces* **2015**, *7*, 13707.

PUBLICATIONS

- 1 **Chen, W. Y.**; Yen, C. C.; Xue, S.; Wang, H.; Stanciu, L. A., Surface functionalization of layered molybdenum disulfide for the selective detection of volatile organic compounds at room temperature. *ACS Appl. Mater. Interfaces* **2019**, 11, 34135–34143
- 2 **Chen, W. Y.**; Yermembetova, A.; Washer, B. M.; Jiang, X.; Shuvo, S. N.; Peroulis, D.; Wei, A.; Stanciu, L. A., Selective detection of ethylene by MoS₂-carbon nanotube networks coated with Cu(I)-pincer complexes. *ACS Sens.* **2020**, 5, 1699.
- 3 **Chen, W. Y.**; Jiang, X.; Lai, S. N.; Peroulis, D.; Stanciu, L. A., Nanohybrids of a MXene and transition metal dichalcogenide for selective detection of volatile organic compounds. *Nat. Commun.* **2020**, 11, 1302
- 4 **Chen, W. Y.**; Lai, S. N.; Yen, C. C.; Jiang, X.; Peroulis, D.; Stanciu, L. A., Surface functionalization of Ti₃C₂T_x mxene with highly reliable superhydrophobic protection for volatile organic compounds sensing. *ACS Nano* **2020**, 14, 11490
- 5 **Chen, W. Y.**; Yermembetova, A.; Washer, B. M.; Jiang, X.; Shuvo, S. N.; Peroulis, D.; Wei, A.; Stanciu, L. A., Selective detection of ethylene by MoS₂-carbon nanotube networks coated with Cu(I)-pincer complexes. *ACS Sens.* **2020**, 5, 1699.
- 6 Shuvo, S. N.; Ulloa Gomez, A. M.; Mishra, A.; **Chen, W. Y.**; Dongare, A. M.; Stanciu, L. A., Sulfur-doped titanium carbide MXenes for room-temperature gas sensing. *ACS Sens.* **2020**, 5, 2915.
- 7 **Chen, W. Y.**; Lin, H.; Barui, A.; Ulloa, A.; Wendt, M.; Stanciu, L. A., Single-strained DNA functionalized Ti₃C₂T_x MXenes for selective and rapid detection of SARS-CoV-2 nucleocapsid gene, submitted
- 8 **Chen, W. Y.**; Zhang, H. T.; Park, J. T.; Lin, H.; Chan, H.; Sankaranarayanan, S.; Wendt, M.; Stanciu, L. A.; Ramanathan, S., Low concentration detection of COVID-19 virus using correlated perovskite nickelates, in preparation